Department of Precision and Microsystems Engineering

The Moving Node Approach in Topology Optimization

An Exploration to a Flow-inspired Meshless Method-based Topology Optimization Method

Johannes. T. B. Overvelde

Report no	:	EM 12.006
Coach	:	Dr. ir. Matthijs Langelaar
Professor	:	Prof. dr. ir. Fred van Keulen
Specialization	:	Solid and Fluid Mechanics Structural Optimization and Computational Mechanics
Type of report	:	Master thesis
Date	:	18 April 2012

Delft University of Technology

Faculty of Mechanical, Maritime and Materials Engineering

The Moving Node Approach in Topology Optimization

An Exploration to a Flow-inspired Meshless Method-based Topology Optimization Method

A Master's Thesis in
Mechanical Engineering
by

Johannes T.B. Overvelde

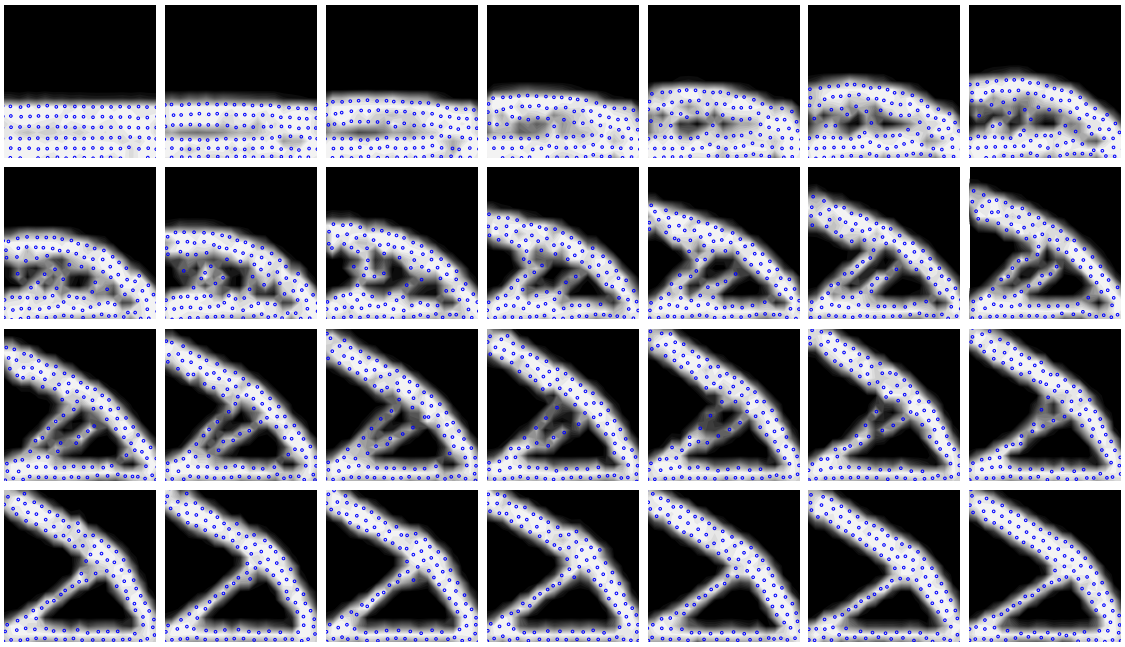

April 18, 2012

Faculty of Mechanical, Maritime and Materials Engineering

The Moving Node Approach in Topology Optimization

An Exploration to a Flow-inspired Meshless Method-based Topology Optimization Method

A Master's Thesis in
Mechanical Engineering
Track: Solid and Fluid Mechanics (SFM)
Specialization: Structural Optimization and Computational Mechanics

Author
Johannes T.B. Overvelde
Student no. 1228145
www.overvelde.com

Exam Committee
Prof.dr.ir. Fred van Keulen
Dr.ir. Matthijs Langelaar
Prof.dr.ir. Miguel A. Gutiérrez De La Merced
Sergio R. Turteltaub Ph.D.

April 18, 2012

Preface

This Master's thesis is submitted in fulfillment of the requirements for the Degree of Master of Science in the subject of mechanical engineering at the Faculty of Mechanical, Maritime and Materials Engineering at Delft University of Technology.

The subject of the thesis flows naturally from the composition of my Master's track Solid and Fluid Mechanics, with a specialization in Optimization and Computational Engineering. The problem definition and proposed ideas arise from a combination of practices and methods employed in solid mechanics, optimization and fluid mechanics.

The field of solid mechanics and optimization are often associated with each other and the combination of the two proves to be very fruitful, i.e. topology optimization. In this thesis, fluid dynamics is thrown into the mix and together the fields create a trinity that shows great potential. I am excited to present the results.

Haarlem April 18, 2012

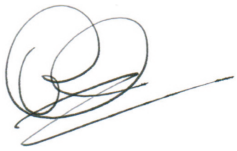

Johannes T.B. Overvelde

Acknowledgments

This Master's thesis is submitted in fulfillment of the requirements for the Degree of Master of Science in the subject of mechanical engineering at the Faculty of Mechanical, Maritime and Materials Engineering at Delft University of Technology. I wish here to express my sincere appreciation to Prof. dr. ir. Fred van Keulen, professor and chair of the research group Structural Optimization and Computational Mechanics - Applied Mechanics at the Department of Precision and Microsystems Engineering (PME) at the Faculty of Mechanical, Maritime and Materials Engineering at Delft University of Technology, for his constructive criticism and for allowing and supporting me to pursue my own research ideas.

I am grateful to Dr. ir. Matthijs Langelaar, assistant professor at the research group Structural Optimization and Computational Mechanics - Applied Mechanics at the Department of Precision and Microsystems Engineering (PME) at the Faculty of Mechanical, Maritime and Materials Engineering of Delft University of Technology for the numerous fruitful and candid discussions. I highly appreciate his enthusiasm and input. My colleagues Nico van Dijk, Hans Goosen, Miquel Gutiérrez De La Merced, Evert Hooijkamp, Kelvin Ng Wei Siang, Hugo Peters, Samee-ur Rehman, Mohammad Samimi, Saputra, Kostiantyn Vandyshev, Alexander Verbart, Tim van Wageningen, Jeroen Wolfs, Stanley Wong and Marco Zocca at the research group Structural Optimization and Computational Mechanics - Applied Mechanics at the Department of Precision and Microsystems Engineering (PME) at the Faculty of Mechanical, Maritime and Materials Engineering of Delft University of Technology, all of whom I gratefully acknowledge here with my sincere thanks for their critical contributions during the weekly CHARLES meetings.

I would also like to seize this opportunity to thank Katia Bertoldi, Ph.D., assistant professor in Applied Mechanics at the School of Engineering and Applied Sciences at Harvard University, for her kind encouragements, trust and interest. Katia has been an incredible source of inspiration during my research internship at Harvard University in 2010, and remained so unremittingly in the succeeding

years. I am glad we continued working together and maintain in touch through boundless email and Skype communication.

I wish to thank my employers Ir. Tom Santegoeds and Dr. ir. Ronald van Dijk, proprietors of Femto Engineering for their kind-heartedness and flexibility.

Of course I thank all family and friends for their love and support. Finally, I am most grateful to my fiancée Sanne Slagman, for all her support throughout my studies. She has encouraged and taught me to reach for the sky. Without her, I would not have been able to finish my studies so excellently. Above all, I thank her for her infinite trust and love.

Contents

Chapter 1

Introduction

1.1 FEM-based topology optimization

This Master's thesis is situated in the field of topology optimization. Topology optimization is concerned with finding the optimal material layout, in which the optimal layout is determined according to specific performance targets. The material layout in various fields, such as solid mechanics, fluid dynamics and thermodynamics can be optimized using topology optimization. Applications of topology optimization are for example: satellite support structure designs that weigh less than a specified mass, yet are strong enough to carry the instruments during launch [1]; optimization of the mixing performance of laminar static mixers [2]; two-phase composites design having maximum thermal expansion, zero thermal expansion, or negative thermal expansion [3]; optimization of the crashworthiness of cars, where during impact the front of the car keeps a certain acceleration and only a certain intrusion is reached [4].

The difference between the various topology optimization problems is the physical problem, i.e. the governing differential equations and boundary conditions. The mathematical algorithms underlying the optimization of the layout are universal. Thus, two main components of topology optimization can be distinguished: the physical problem and the optimization problem. The interaction between both problems is illustrated in Fig. 1.1.

Although the mathematical optimization algorithms are universal and can be applied to various physical fields, a variety of optimization methods has been proposed in literature. At least three main methods can be identified: the density-based homogenization method, the Evolutionary Structural Optimization (ESO) method and the level-set method. These three methods are discussed next.

In 1988 Bendsøe and Kikuchi [5] introduced one of the first topology opti-

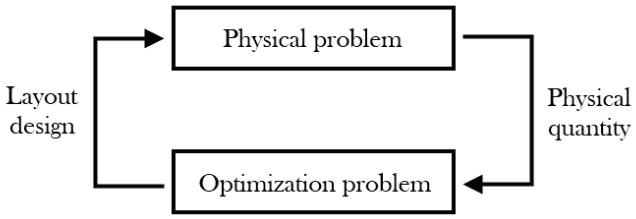

Figure 1.1: The two components of topology optimization. The physical problem is solved and forms the input for the optimization problem. In the optimization problem the shape is adapted to better meet the performance targets. This cycle is repeated until the optimal design is reached.

mization methods: the homogenization method. In the homogenization method the design space[1] is covered with cells that contain a microstructure. The shape of this microstructure is parameterized such that the cell can represent various compositions, from completely filled with material to completely empty. With these cells the rather difficult topology optimization problem is simplified to a sizing problem of the microstructural parameters, in which the parameters can vary from cell to cell. However, for some objectives the homogenization method may not result in plausible designs. The homogenization method often produces layouts with infinitesimal holes, which make the design difficult to fabricate.

Some variations on the homogenization method have been proposed. Especially the Solid Isotropic Material with Penalization (SIMP) method has gained wide-spread attention [6], [7]. The power of the SIMP method lies in its conceptual and computational simplicity. In this method the presence of material is given by the density of the cells, instead of the shape of the microstructure. By varying the normalized cell density between zero and one, material can locally be added or removed. Penalization of intermediate density is introduced in this formulation in order to obtain manufacturable designs. However, numerical instabilities, such as checkerboard patterns, mesh-dependencies and local minima can occur in this method [8]. In order to prevent these problems, additional measures should be incorporated in the method. For instance, checkerboard patterns can be prevented by minimum length scale filters.

Another topology optimization method, called the ESO method, has been proposed in 1993 by Xie and Steven [9]. This method is based on the gradual removal of material to achieve an optimal design. In contrast to the SIMP method, the design space contains only material with a normalized cell density of either

[1]The domain in which material can be present. Note that the final layout will always be contained inside the design space.

zero or one, and therefore intermediate density does not exist. However, the final design is highly sensitive to the initial design space and the size of the underlying cell structure [10].

The level-set method, proposed in 2000 by Sethian and Weigmann [11], tries to overcome some of the aforementioned problems such as numerical instability and intermediate density. This method describes the varying layout of the structure with a level-set function. Material can therefore also be gradually added in the level-set method. The removal or addition of the material occurs near the boundaries of the design, in which the tracking of boundaries is done by a level-set algorithm. The addition of material makes the final design less sensitive to the initial design and the underlying cell structure. However, intermediate density may still exist near the boundary, depending on the numerical implementation.

The physical problem can be described in terms of a partial differential equation, or a set of partial differential equations. The solution to such equations is often found by a numerical method, when the problem is too complex to solve analytically. All aforementioned topology optimization methods have in common that the governing equations of the physical problem are typically solved by the same numerical technique, called the Finite Element Method (FEM). By use of this method the complex partial differential equations are reduced to a set of simple linear algebraic equations.

FEM is based on the discretization of the domain Ω and its boundary Γ by a mesh. To create the mesh, nodes are distributed in the domain Ω and on its boundary Γ. These nodes are connected with each other through elements. Thus, the domain is discretized with a fixed interconnection between the nodes. As an example, a triangular mesh of a two-dimensional domain is shown in Fig. 1.2a.

However, some difficulties arise when using a mesh. It is for instance difficult to determine a good robust mesh, especially in three-dimensional domains [12]. Also, in large deformation and displacement problems, the mesh will deform and become less reliable. Remeshing is used to solve this problem, although it is computationally time consuming [13], [14]. Another problem for which standard FEM is not well suited, is the propagation of cracks in solids [15].

1.2 Meshless method-based topology optimization

To overcome some difficulties that arise when using FEM, meshless discretization techniques have been applied. These techniques are also called meshless methods.

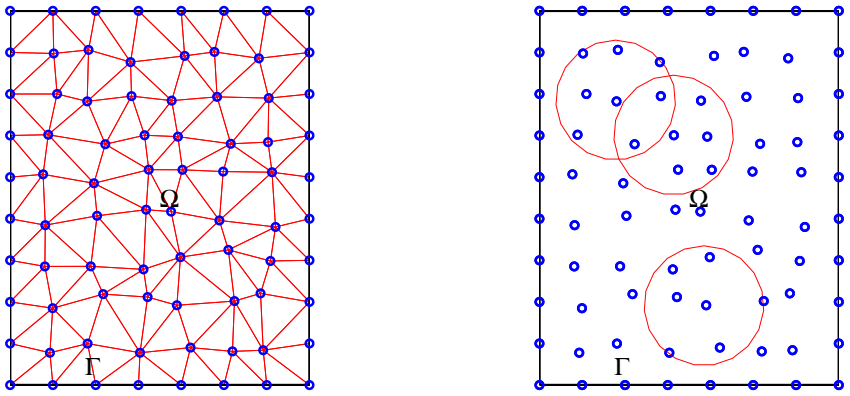

(a) Typical FEM discretization (b) Typical meshless method discretization

Figure 1.2: Typical FEM and meshless method discretization of a rectangular domain Ω and its boundary Γ (black line). The domain is discretized using nodes (blue circles). For the FEM discretization the element boundaries are in red. For the meshless method discretization the boundary of the influence or local domain is given in red.

In these methods the simple linear algebraic equations are constructed entirely in terms of nodes.[2] These nodes have no fixed elements connecting each other, in contrast the connections are simply formed between neighboring nodes. In Fig. 1.2b a discretized rectangular domain Ω and its boundary Γ are shown. The influence domain of nodes, which determines the connections between neighboring nodes, is also shown.

One of the first meshless methods, called the Smoothed Particle Hydrodynamics (SPH) method, was constructed in 1977 by Gingold and Monaghan [17] and independently by Lucy [18]. This method was first created for modeling astrophysical phenomena, and later to model fluid dynamic problems. The first attempt to model solid mechanics (impact) problems was by Libersky [19] in 1993. The SPH method is based on the strong form notation of partial differential equations (hereafter: strong form) [20], [21]. The strong form in solid mechanics contains second order derivatives, and therefore the discretization becomes troublesome.

Other methods were developed in the early 1990's. These methods are based on the weak form notation of partial differential equations (hereafter: weak form) [20], [21]. For the weak form there is no necessity to discretize second order derivatives. The first developed method based on the weak form, and mainly applied to solid mechanics, is the Element-free Galerkin (EFG) method [12]. Although the EFG method does not require a mesh to give relations between nodes, a background mesh is necessary for the evaluation of the integrals present in the weak form.

[2]The term 'node' will be used throughout this thesis, although in some literature the terminology 'particle' is used instead [16], [17].

More recently, in 1998, Atluri and Zhu proposed a different method called the Meshless Local Petrov-Galerkin (MLPG) method, which is based on the local weak form [22]. In this method, the integrals present in the local weak form are evaluated on sub-domains, therefore no background mesh is needed.

The EFG and MLPG methods are some of the most common methods. Obviously, these are not the only available meshless methods. A more complete overview of meshless methods is provided in the work of Nguyen et al [14]. However, to limit the scope, this thesis focusses on the EFG and MLPG mixed collocation method.

During the last decade, meshless methods have also been applied to discretize and solve the physical problem in topology optimization. As a proof of concept, various meshless methods have been applied to discretize the governing equations of linear physical problems with the use of the SIMP method [23], [24], [25], [26], ESO method [13] and the level-set method [27], [28], [29], [30], [31], [32]. The meshless SIMP method has also been applied to intricate non-linear problems [33], [34], [35], [36], elucidating the capabilities of meshless methods in topology optimization. In principle, these meshless method-based topology optimization methods have been introduced to increase the capabilities of topology optimization for use in non-linear physical problems. In these topology optimization applications, the meshless methods have been used as a direct replacement of FEM, in which the nodal distribution remained unchanged during the optimization process.

1.3 Flow-inspired meshless method-based topology optimization

A possible alternative to topology optimization methods based on regular nodal distributions, might be generated from the field of fluid dynamics. In fluid dynamics, the governing partial differential equations are usually expressed in the Eulerian form, i.e. at each coordinate in the problem domain Ω the fluid velocity and density are tracked [37]. This approach works well for problems in which the complete problem domain Ω consists of one type of fluid. However, for free surface, multi-phase and mixing flows the Eulerian description of the fluid is unsuitable. A Lagrangian form of the governing partial differential equations is more compatible with these types of boundary flows [16].

New developments in discretization techniques depart from a Lagrangian formulation of the governing equations. In the Lagrangian form, the fluid is modeled

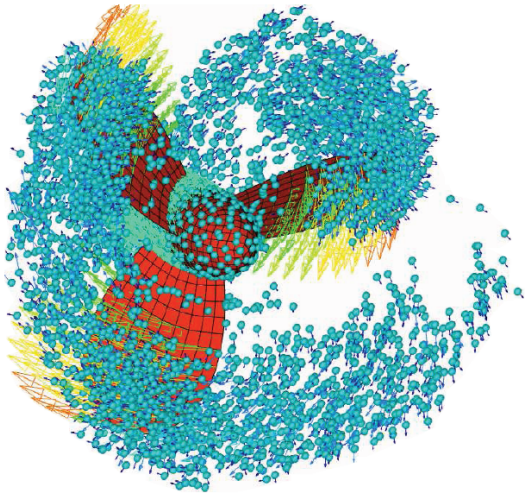

Figure 1.3: Fluid flow around a moving propeller, found with the SPH method. The results have been obtained by Femto Engineering [38].

as mass-containing nodes, which can move through the problem domain Ω. Since the mass is fixed to these nodes, it is much simpler to combine fluids and multiple phases. The meshless SPH method is often used, in order to solve the governing partial differential equations in the Lagrangian form. Fig. 1.3 shows an instantaneous SPH image of a fluid flow.

Comparable to the Eulerian form in fluid dynamics, are the topology optimization methods based on fixed and regular discretizations of the problem domain. In these approaches, the presence of material is determined at every coordinate in the design space. For the SIMP, ESO and level-set methods the amount of material at every coordinate depends on the coordinate density, which can either take on continuous or discrete values. In the Eulerian approach, this coordinate density is mostly used as the design variable in the topology optimization problem.

This leaves open the possibility to investigate the opportunities of a flow-inspired Lagrangian approach in topology optimization. Such a flow-inspired approach could result in a topology optimization method in which the density is determined from the position of the mass-containing nodes. The design variable for the Lagrangian approach is then not the density, but the nodal position. The layout of the problem domain Ω could possibly be transformed by moving the nodes through the design space. Although this approach has not been the subject of discussion in literature, it could possibly provide in exciting new openings in topology optimization.

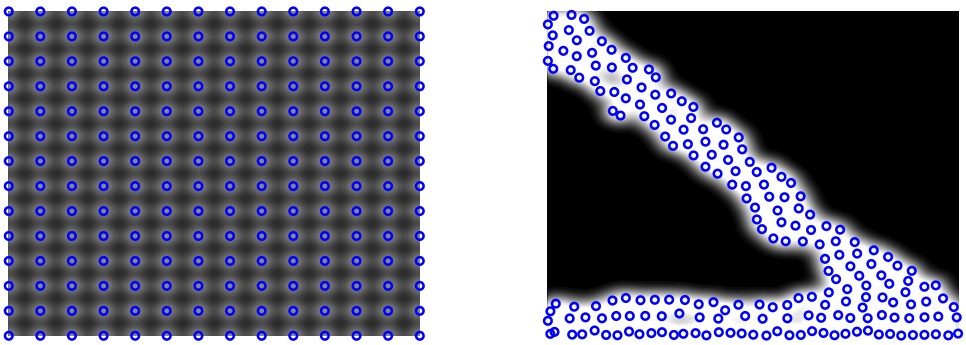

Figure 1.4: Normalized density of two constructed nodal distributions illustrating the MNA concept, where the nodes are depicted as the blue circles. Material (white area) exist around the nodes, and no material is present at the black areas. Grey areas contain intermediate density.

The question is then:

What are the opportunities for a flow-inspired moving node approach in topology optimization?

This thesis explores the possibility of a flow-inspired meshless method-based approach in topology optimization. By employing the position of the nodes as design variables in the topology optimization method, this approach could possibly provide for exciting new opportunities in topology optimization. The topology optimization problem then transforms into a flow-like problem, in which the material moves to a more optimal distribution. An example of a change in layout by the redistribution of nodes is shown in Fig. 1.4. This concept is comparable to replacing the mesh in CFD by mass-containing nodes in an SPH setting. The featuring characteristic of this newly proposed meshless method-based topology optimization method is its moving node approach. Therefore, in this thesis this newly proposed topology optimization method will be referred to as the Moving Node Approach (hereafter: MNA).

1.4 Thesis structure

The focus of this thesis is the exploration of a flow-inspired topology optimization method and the assessment of its potential. To highlight this newly proposed method, only the optimization of the layout of well established and relatively simple physical problems is considered in this thesis. More specifically, the employed physical problem is the two-dimensional linear elastic solid under force loading

(hereafter: linear elasticity problem).

Since the MNA method will be based on meshless methods, it is of key importance to dissect relevant characteristics of widely used meshless methods. To gain better insight in meshless methods, two different meshless methods, respectively the EFG and MLPG mixed collocation method, are investigated. Therefore, in Chap. 2 the linear elasticity problem is discretized and an exemplary problem is solved using these two meshless methods. Furthermore, a convergence study on the accuracy of both meshless methods is performed.

In Chap. 3 the meshless method with the highest potential is tested further in order to explore the effect of the nodal distribution on the accuracy of the solution and on the material distribution. The favorable properties of the meshless method that can be utilized in the formulation of the MNA in topology optimization are determined from exemplary problems. Moreover, additional conditions on the nodal distribution are determined.

Chap. 4 will choose and adapt an existing meshless method in order to solve the physical problem and effectively be able to move the material layout in MNA. The material distribution in the meshless method is altered by introducing a material density defined by the nodal compaction. Moreover, in this chapter the favorable characteristics of this material distribution are determined.

Finally, in Chap. 5 the observations and alterations from previous chapters are applied to propose an MNA topology optimization algorithm. This algorithm is then used to determine the optimal shape of some exemplary problems. Based on these findings favorable characteristics of the MNA are derived.

Chapter 2

Meshless Methods

In this chapter meshless method-based discretization techniques are discussed. To gain better insight in meshless methods, the workings of two distinct meshless methods, respectively the EFG and MLPG mixed collocation method, are investigated. Sec. 2.1 discusses the approximations methods used in meshless methods. In Sec. 2.2 the linear elasticity problem is discretized using both the EFG and MLPG mixed collocation method. Next, in Sec. 2.3 the aforementioned meshless methods are applied to the exemplary problem of a two-dimensional cantilever beam and the specific characteristics of both methods are discussed. Finally, in Sec. 2.4 the favorable characteristics of meshless methods for the MNA in topology optimization are discussed.

2.1 Approximation methods

Sec. 2.1 introduces approximation methods, which are at the base of most discretization techniques. It is essential to have a clear understanding of approximation methods, in order to be able to use meshless methods. Here, three different approximation methods are discussed: FEM approximations (Sec. 2.1.1), kernel approximations (Sec. 2.1.2) and Moving Least Squares (MLS) approximations (Sec. 2.1.3). In order to provide insight in their workings, a general notation is introduced as well as an exemplary problem in order to demonstrate how the approximation methods function.

General notation

The three aforementioned approximation methods share a general notation which is also used in FEM. A continuous scalar function $u(\boldsymbol{x})$ and its derivative $u_{,j}(\boldsymbol{x})$ can

be approximated with a finite number of known scalar function values $u(\boldsymbol{x}^I) = u^I$, where $I = 1...n$ and n is the number of coordinates $\boldsymbol{x}^I$. These coordinates $\boldsymbol{x}^I$ for which the scalar function is known are called the nodes. Here, $\boldsymbol{x}$ is the vector containing the coordinates x_i for $i = 1...l$ for a l-dimensional domain, and the subscript $,j$ is the notation for the derivative with respect to coordinate x_j. At each node I a shape function $\phi^I(\boldsymbol{x})$ is defined, in order to interpolate between the known scalar values at each node u^I and to find the approximated scalar value and its derivative for all $\boldsymbol{x}$. The weight of each shape function is given by $u^I = u(\boldsymbol{x}^I)$, where the weight determines the contribution of each shape function to the total approximation. The approximation of the continuous scalar function $u(\boldsymbol{x})$ is written as

$$u(\boldsymbol{x}) \approx u^h(\boldsymbol{x}) = \sum_{I=1}^{n} \phi^I(\boldsymbol{x}) u^I \tag{2.1}$$

and the approximation of the derivative $u_{,j}(\boldsymbol{x})$ equals

$$u_{,j}(\boldsymbol{x}) \approx u^h_{,j}(\boldsymbol{x}) = \sum_{I=1}^{n} \phi^I_{,j}(\boldsymbol{x}) u^I, \tag{2.2}$$

where $\phi^I(\boldsymbol{x})$ is the value of the shape function belonging to node I at coordinate $\boldsymbol{x}$, and $\phi^I_{,j}(\boldsymbol{x})$ is the value of the derivative in direction x_j of the shape function from node I at coordinate $\boldsymbol{x}$.

One-dimensional exemplary problem

Although the three approximation methods share a general notation, they differ in their shape functions. Sec. 2.1.1, Sec. 2.1.2 and Sec. 2.1.3 elaborate on these distinctions. To exemplify these dissimilarities in the shape functions of the approximations, the following one-dimensional problem is used.

The problem domain Ω is given by a line of length $L = 10$. The coordinates of the domain are given by x. The boundary Γ is given by the outer left coordinate $x = 0$ and the outer right coordinate $x = L$. At each coordinate a scalar function $u(x)$ and its derivative $u_{,x}(x)$ are respectively defined by

$$u(x) = -\left[L - x\right]^2 + L^2 + \frac{L^2}{4}\cos\left[\frac{6\pi x}{L}\right] \tag{2.3}$$

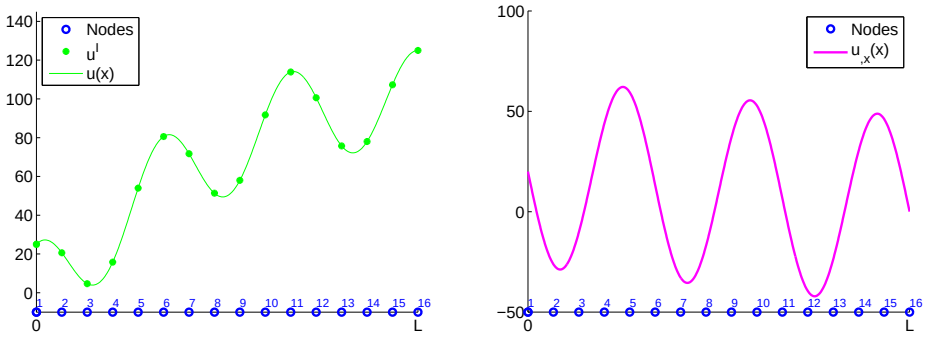

(a) Scalar function $u(x)$ and scalar nodal values u^I

(b) Derivative of the scalar function $u(x)_{,x}$

Figure 2.1: Scalar function $u(x)$ and derivative of scalar function $u_{,x}(x)$ from Eq. 2.3 and Eq. 2.4. The nodal values u^I are also shown. The blue integers indicate the node numbers.

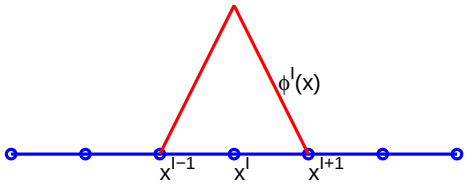

Figure 2.2: Shape function ϕ^I (red line) for node I. Node I and its neighboring nodes are depicted as blue circles.

and

$$u_{,x}(x) = 2\left[L - x\right] - \frac{6\pi L}{4}\sin\left[\frac{6\pi x}{L}\right]. \tag{2.4}$$

The scalar function $u(x)$ and its derivative $u_{,x}(x)$, can be approximated using the values at a finite number of nodes. In the introduced one-dimensional problem, the domain Ω is discretized by sixteen nodes, which are equally spaced. The scalar function at each node is known, and is given by $u(\boldsymbol{x}^I) = u^I$ for $I = 1...16$. The nodes, $u(x)$ and $u_{,x}(x)$ are shown in Fig. 2.1.

2.1.1 FEM approximation

In order to create the shape function in FEM, connections between nodes need to be assigned. The total collection of connections is also called the mesh. To mesh the domain in the one-dimensional problem (shown in Fig. 2.1), neighboring nodes need to be connected. This results in fifteen elements, where a single element is a connection between two nodes.

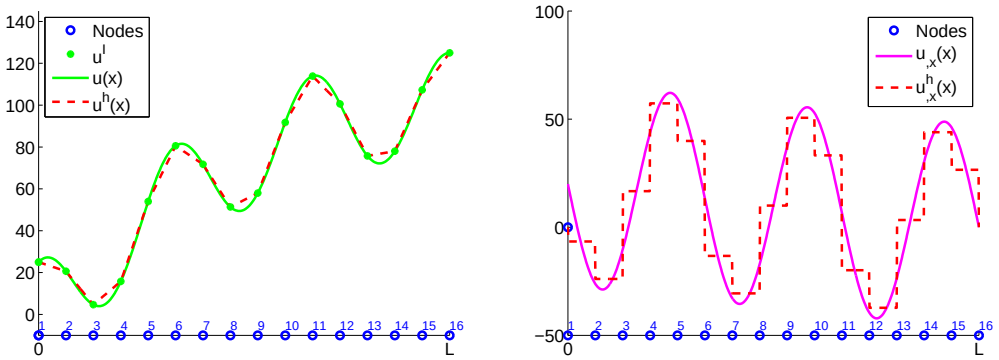

(a) $u^h(x)$ (b) $u^h_{,x}(x)$

Figure 2.3: Approximation of the scalar function $u^h(x)$ and the derivative of the scalar function $u^h_{,x}(x)$ from (2.3) and (2.4) with FEM.

Now that the mesh is assigned, the shape function of each node can be constituted. The simplest shape function in FEM is the linear shape function. The value of this shape function equals one at the corresponding node and zero at other nodes. Linear interpolation is applied between the corresponding node and the nodes that are connected through elements [21], [20]. Fig. 2.2 shows the linear shape function used in FEM. Once the shape function for each node is known, the derivative of each shape function can be determined by simple taking the derivatives of the linear interpolation functions.

At this point, the scalar values u^I, the shape functions $\phi^I(\boldsymbol{x})$ and the derivative of the shape functions $\phi^I_{,x}(\boldsymbol{x})$ are known for all nodes ($I = 1...n$). From Eq. 2.1 and Eq. 2.2 the approximation of $u^h(x)$ and $u^h_{,x}(x)$ can be determined and are shown in Fig. 2.4. The figure displays $u^h(\boldsymbol{x}^I) = u^I$, which is called the Kronecker Delta property [39], [40], [41].[1] The approximation of the scalar function $u^h(x)$ closely follows the scalar function $u(x)$. However, because the derivative of the shape function is discontinuous, the approximation of the derivative of the scalar function $u^h_{,x}(x)$ is not very accurate. By increasing the number of nodes in the mesh, the approximation of both $u^h(x)$ and $u^h_{,x}(x)$ will become more accurate, although discontinuities in the derivative will always exist. A solution to these discontinuities is the use of higher order shape functions.

[1] Although this property applies to FEM, meshless methods do in general not share this characteristic. This will be further discussed in Sec. 2.1.2 and Sec. 2.1.3.

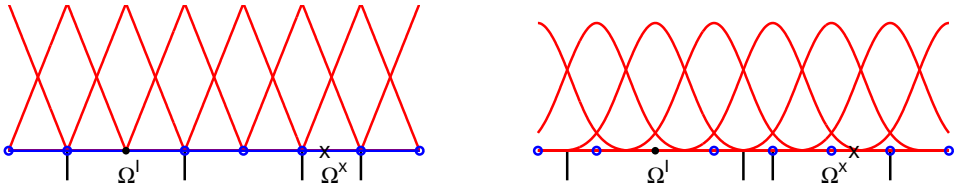

(a) Influence and support domain in FEM

(b) Influence and support domain in meshless methods

Figure 2.4: One-dimensional nodal distribution (circles) and their typical FEM and meshless method shape functions. For the node indicated by the black dot, the influence domain Ω^I is shown. The support domain Ω^x of coordinate x is also shown.

Local characteristic of FEM

A characteristic of the shape functions in FEM is their local influence. The shape function $\phi^I(x)$ is only unequal to zero if $\boldsymbol{x}$ lies on an element connected to node I. Fig. 2.2 shows this local influence for a one-dimensional case. For each node I the influence domain Ω^I is a sub-domain of the total domain Ω, where the shape function $\phi^I(\boldsymbol{x})$ is unequal to zero. For FEM this domain Ω^I is the area covered by the elements connected to node I. Thus, there are n defined influence domains Ω^I in the total domain Ω. For each coordinate $\boldsymbol{x}$, a support (or support domain) is given by Ω^x. The support Ω^x of coordinate $\boldsymbol{x}$ consists of all nodes for which the shape function is unequal to zero. Fig.2.4a shows the influence domain and support domain for a one-dimensional FEM approximation.

Although the definition of these domains seems rather thorough for FEM, meshless methods require a proper understanding of the influence domain Ω^I of node I and support domain Ω^x of coordinate $\boldsymbol{x}$. With this characteristic concerning locality, the summation in Eq. 2.1 and Eq. 2.2 can in FEM be reduced to

$$u(\boldsymbol{x}) \approx u^h(\boldsymbol{x}) = \sum_{J=1}^{k} \phi^J(\boldsymbol{x}) u^J \tag{2.5}$$

and

$$u_{,j}(\boldsymbol{x}) \approx u^h_{,j}(\boldsymbol{x}) = \sum_{J=1}^{k} \phi^J_{,j}(\boldsymbol{x}) u^J, \tag{2.6}$$

where $J = 1...k$ are the nodes in the support Ω^x of coordinate $\boldsymbol{x}$.

2.1.2 Kernel approximation

In the previous discussed FEM approximation (Sec. 2.1.1) a mesh needs to be assigned in order to be able to calculate the shape functions for each node. The kernel approximation is an approximation method in which there is no mesh required. The kernel approximation is used in the meshless method called the SPH method, which was the first existing meshless method [17], [18]. A clear description of the kernel approximation is given in the work of Liu and Liu [16]. Their work gives a thorough and clear description of the SPH method. Therefore it is used as a guideline to explain the kernel approximation.

Basic approximation

A scalar function $u(\boldsymbol{x})$ can be represented by the following integral notation:

$$u(\boldsymbol{x}) = \int_{\Omega} u(\boldsymbol{x}')\delta(\boldsymbol{x}-\boldsymbol{x}')d\boldsymbol{x}' \quad \text{with} \quad \delta(\boldsymbol{x}-\boldsymbol{x}') = \begin{cases} 1 & \boldsymbol{x}=\boldsymbol{x}' \\ 0 & \boldsymbol{x}\neq\boldsymbol{x}' \end{cases}. \tag{2.7}$$

Here $\delta(\boldsymbol{x}-\boldsymbol{x}')$ is called the Dirac delta function. Eq. 2.7 is an exact representation of $u(\boldsymbol{x})$. An approximation of the scalar function $u^h(\boldsymbol{x})$ can be found by smoothing a finite number of known values $u(\boldsymbol{x}^I) = u^I$, where $I = 1...n$. To be able to smooth the known values in Eq. 2.7, the Dirac delta function is replaced by a kernel function $W(\boldsymbol{x}-\boldsymbol{x}', d)$, and the integral is replaced by a summation of the known scalar values u^I. The approximation of $u(\boldsymbol{x})$ is then

$$u(\boldsymbol{x}) \approx u^h(\boldsymbol{x}) = \sum_{I=1}^{n} W(\boldsymbol{x}-\boldsymbol{x}^I, d)\frac{m^I}{\rho(\boldsymbol{x})}u^I, \tag{2.8}$$

where m^I is the a specified weight of each node, $\rho(\boldsymbol{x})$ is the density at coordinate $\boldsymbol{x}$ and d is a parameter specifying the size of the influence domain Ω^I of the kernel function. The properties of the kernel function will be discussed below. The density $\rho(\boldsymbol{x})$ is determined using the summation density approach, which equals

$$\rho(\boldsymbol{x}) = \sum_{J=1}^{n} m^J W(\boldsymbol{x}-\boldsymbol{x}^J, d). \tag{2.9}$$

This approach specifies that the density at each coordinate is the weighted average of m^I. Eq. 2.8 can be rewritten in the general form (Eq. 2.1) that is used in

approximation methods:

$$u^h(\boldsymbol{x}) = \sum_{I=1}^{n} \phi^I(\boldsymbol{x}) u^I \quad \text{with} \quad \phi^I(\boldsymbol{x}) = \frac{m^I W(\boldsymbol{x} - \boldsymbol{x}^I, d)}{\sum_{J=1}^{n} m^J W(\boldsymbol{x} - \boldsymbol{x}^J, d)}. \tag{2.10}$$

The derivative of the approximation then becomes

$$u^h_{,j}(\boldsymbol{x}) = \sum_{I=1}^{n} \phi^I_{,j}(\boldsymbol{x}) u^I \tag{2.11}$$

with

$$\phi^I_{,j}(\boldsymbol{x}) = \frac{m^I W_{,j}(\boldsymbol{x} - \boldsymbol{x}^I, d)}{\sum_{J=1}^{n} m^J W(\boldsymbol{x} - \boldsymbol{x}^J, d)} - \phi^I(\boldsymbol{x}) \frac{\sum_{K=1}^{n} m^K W_{,j}(\boldsymbol{x} - \boldsymbol{x}^K, d)}{\sum_{J=1}^{n} m^J W(\boldsymbol{x} - \boldsymbol{x}^J, d)}. \tag{2.12}$$

Properties of the kernel function

For a accurate approximation $u^h(\boldsymbol{x})$ of the scalar function $u(\boldsymbol{x})$, the kernel function $W(\boldsymbol{x} - \boldsymbol{x}', d)$ should have three properties. The first property is defined by

$$\int_{\Omega} W(\boldsymbol{x} - \boldsymbol{x}', d) d\boldsymbol{x}' = 1, \tag{2.13}$$

which is called the unity condition. It implies that integration of the kernel function should produce unity. The second property is called the compact condition. For each node I an influence domain Ω_I is defined. The weight function of node I is zero outside this domain. This condition can be written as

$$W(\boldsymbol{x} - \boldsymbol{x}^I, d) = 0 \quad \text{outside} \quad \Omega^I. \tag{2.14}$$

Only for coordinates $\boldsymbol{x}$ that lie within the influence domain of node I, the scalar value u^I has an influence on the approximation. In accordance with this condition, the summation in Eq. 2.11 is reduced to a summation over the nodes in the support Ω^x of coordinate $\boldsymbol{x}$. The third and final property is the delta function condition:

$$\lim_{d \to 0} W(\boldsymbol{x} - \boldsymbol{x}^I, d) = \delta(\boldsymbol{x} - \boldsymbol{x}'). \tag{2.15}$$

This condition ensures that for coordinates $\boldsymbol{x}$ closer to a node, the value of the kernel function is higher. Moreover, for smaller influence domains Ω^I, the kernel function resembles the Dirac delta function more closely. According to Eq. 2.7 this results in a better approximation. However, reducing the influence domain size d is only possible if there are enough nodes in the support domain Ω^x of coordinate

$\boldsymbol{x}$.

A normalized kernel function, that satisfies these aforementioned three conditions, is the cubic spline weight function [14], [42], [43]:

$$W(\boldsymbol{x}-\boldsymbol{x}^I,d)=W(r)=\alpha\begin{cases}\frac{2}{3}-4r^2+4r^3 & \text{if} \quad 0\leq r\leq\frac{1}{2}\\ \frac{4}{3}-4r+4r^2-\frac{4}{3}r^3 & \text{if} \quad \frac{1}{2}\leq r\leq 1\\ 0 & \text{otherwise}\end{cases}. \tag{2.16}$$

The derivative of the cubic spline weight function equals

$$W_{,r}(r)=\alpha\begin{cases}-8r+12r^2 & \text{if} \quad 0\leq r\leq\frac{1}{2}\\ -4+8r-4r^2 & \text{if} \quad \frac{1}{2}\leq r\leq 1\\ 0 & \text{otherwise}\end{cases}, \tag{2.17}$$

where r is the normalized distance and α is a constant depending on the dimension and shape of the kernel function. In general, α is chosen in such a way that the unity condition from Eq. 2.13 is satisfied. However, because the summation density approach from Eq. 2.9 is used, the final approximation becomes independent of α.

In a one-dimensional domain, the normalized distance r is chosen such that

$$r=\frac{|x-x_i|}{d}. \tag{2.18}$$

In accordance with this equation, the influence domain Ω^I of node I is given by $-d\leq x^I\leq d$. A one-dimensional example of the cubic spline weight function and its derivative, is shown in Fig. 2.5. Moreover, Fig. 2.4b shows the influence domain and support domain for a one-dimensional Kernel approximation.

In a two-dimensional domain, the influence domain of a node can adopt any shape. However, commonly used influence domains are circular or rectangular. The kernel function for a circular influence domain Ω^I is

$$W(\boldsymbol{x}-\boldsymbol{x}^I,d)=W(r) \tag{2.19}$$

and the derivative is

$$W_{,j}(\boldsymbol{x}-\boldsymbol{x}^I,d)=W_{,j}(r)=w_{,r}(r)r_{,j}, \tag{2.20}$$

where $,j$ is the derivative with respect to the x_j direction and $r=\frac{||\boldsymbol{x}-\boldsymbol{x}^I||}{d}$. For a

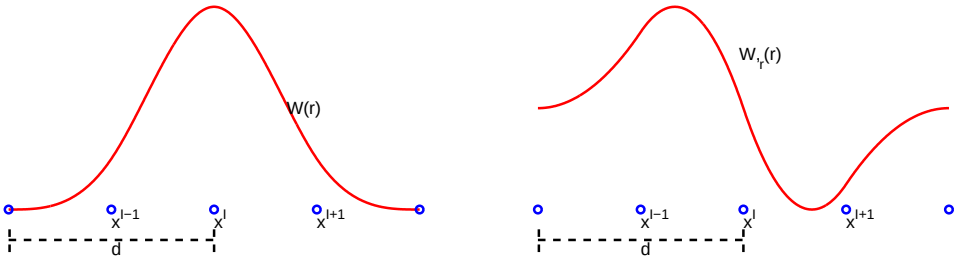

(a) $W(r)$ (b) $W_{,r}(r)$

Figure 2.5: A one-dimensional example of the spline kernel function and its derivative. The size of the support domain is equals $2d$.

rectangular influence domain Ω^I the kernel function equals

$$W(\boldsymbol{x} - \boldsymbol{x}^I, d) = W(r_1, d_1 d)W(r_2, d_2 d) \tag{2.21}$$

and the derivatives equal

$$\begin{aligned} W_{,1}(\boldsymbol{x} - \boldsymbol{x}^I, d) &= W_{,1}(r_1)W(r_2) = W_{,r_1}(r_1)r_{1,1}W(r_2) \quad \text{and} \\ W_{,2}(\boldsymbol{x} - \boldsymbol{x}^I, d) &= W(r_1)W_{,2}(r_2) = W(r_1)W_{,r_2}(r_2)r_{2,2}, \end{aligned} \tag{2.22}$$

where $r_j = \frac{|x_j - x_j^I|}{d_j d}$ for $j = 1, 2$ and $d_1 d$ and $d_2 d$ are respectively the sizes of the domain in the x_1 and x_2 direction. d_1 and d_2 are values determined from the average node distance in de x_1 and x_2 direction. The size of the influence domain Ω^I alters when varying the parameter d.

An example of a problem domain Ω is shown in Fig. 2.6. In this figure both circular and rectangular influence domains are shown. The size d of the rectangular domain should be chosen such that the total domain Ω is completely covered by the sum of the local influence domains.

Solution to the one-dimensional exemplary problem

The kernel approximation is applied to the one-dimensional problem as shown in Fig. 2.1. Because the kernel approximation is a meshless method, there is no need for a mesh. Instead, the size d of the influence domain is provided for each node. For simplicity, the influence domain is chosen to be similar for each node, where $d = 2$. According to the approximation in Eq. 2.10, a weight m needs to be

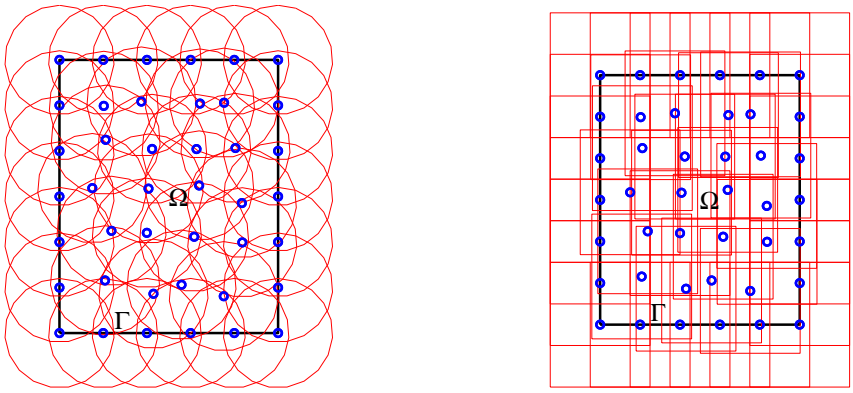

(a) Circular influence domains (b) Rectangular influence domains

Figure 2.6: Example of a rectangular problem domain Ω and boundary Γ. The domain is discretized with nodes (blue circles), each having an influence domain depicted in red.

assigned to each node. This weight is chosen to be the same for each node. The cubic spline function from Eq. 2.16 is used as the weight function.

Next, the scalar function $u(x)$ from Eq. 2.10 and its derivative $u_{,x}(x)$ from Eq. 2.11 are approximated and shown in Fig. 2.7. This figure clearly shows that the approximation of the scalar function $u(x)$ is continuous, but does not satisfy the Kronecker delta criterion i.e., $u^h(\boldsymbol{x}^I) \neq u^I$. Although the approximation does not satisfy this criterion, the approximation is still reasonably good. However, near the boundaries of the domain Ω, the derivative of the approximation $u_{,x}(x)$ is inaccurate. Since the derivative is often used in meshless methods, the accuracy of the approximation needs to be improved. In order to do so, an other approximation method that reduces these inconsistencies near the boundaries is explained in Sec. 2.1.3.

2.1.3 MLS approximation

The previously explained kernel approximation (Sec. 2.1.2) does not require a mesh, however the derivative of the approximation shows inconsistencies near the boundaries of the domain Ω. The MLS approximation is in fact, a more general formulation of the kernel approximation, in which these inconsistencies are reduced. Originally, the MLS approximation was created for fitting a smooth curve through a set of points, but nowadays the most common application is probably the meshless EFG method [14], [15], [12].

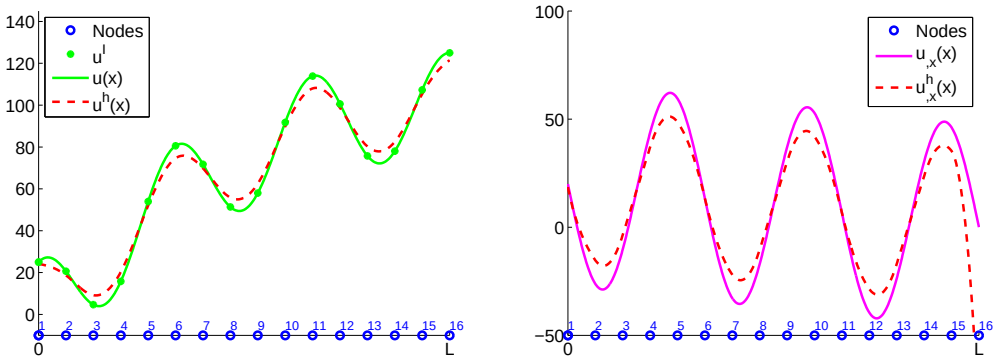

(a) $u^h(x)$ (b) $u^h_{,x}(x)$

Figure 2.7: Approximation of a scalar function $u(x)$ and the derivative of the scalar function $u_{,x}(x)$ with the kernel approximation. The size of the influence domain Ω^I around each node is specified by $d = 2$.

Basic approximation

A scalar function $u(\boldsymbol{x})$ can be approximated with a finite number of n nodes, for which the scalar value $u(\boldsymbol{x}^I) = u^I$ is known (in which $I = 1...n$). The approximation is defined by

$$u(\boldsymbol{x}) \approx u^h(\boldsymbol{x}) = \sum_{l=1}^{m} p_l(\boldsymbol{x}) a_l(\boldsymbol{x}) = \boldsymbol{p}^{\mathrm{T}}(\boldsymbol{x})\boldsymbol{a}(\boldsymbol{x}), \tag{2.23}$$

where $\boldsymbol{p}(\boldsymbol{x})$ is a vector containing monomials, m is the number of monomials in $\boldsymbol{p}(\boldsymbol{x})$ and $\boldsymbol{a}(\boldsymbol{x})$ is a vector containing m coefficients. Two examples of a monomial basis $\boldsymbol{p}(\boldsymbol{x})$ are the linear basis

$$\begin{aligned} \boldsymbol{p}(\boldsymbol{x}) &= \begin{bmatrix} 1 & x \end{bmatrix}^{\mathrm{T}} \quad 1D \quad m = 2 \\ \boldsymbol{p}(\boldsymbol{x}) &= \begin{bmatrix} 1 & x & y \end{bmatrix}^{\mathrm{T}} \quad 2D \quad m = 3 \end{aligned} \tag{2.24}$$

and the quadratic basis

$$\begin{aligned} \boldsymbol{p}(\boldsymbol{x}) &= \begin{bmatrix} 1 & x & x^2 \end{bmatrix}^{\mathrm{T}} \quad 1D \quad m = 3 \\ \boldsymbol{p}(\boldsymbol{x}) &= \begin{bmatrix} 1 & x & y & x^2 & y^2 & xy \end{bmatrix}^{\mathrm{T}} \quad 2D \quad m = 6. \end{aligned} \tag{2.25}$$

To determine the coefficients in $\boldsymbol{a}(\boldsymbol{x})$, a weighted least square fit is performed around coordinate $\boldsymbol{x}$. The weighted least square fit is found by minimizing a

weighted discrete L_2 norm, in which the norm equals

$$J(\boldsymbol{x}) = \sum_{I=1}^{k} W(\boldsymbol{x} - \boldsymbol{x}^I, d) \left[\boldsymbol{p}^{\mathrm{T}}(\boldsymbol{x}^I)\boldsymbol{a}(\boldsymbol{x}) - u^I\right]^2. \tag{2.26}$$

Here, $\boldsymbol{x}^I$ are the coordinates of the nodes and $W(\boldsymbol{x} - \boldsymbol{x}^I, d)$ is a kernel function. The properties of the kernel function are discussed in detail in Sec. 2.1.2. Note that the summation over all n nodes in domain Ω, can be reduced to a summation over the k nodes in the support Ω^x of coordinate $\boldsymbol{x}$. This can be assumed since the kernel function $W(\boldsymbol{x} - \boldsymbol{x}^I, d)$ has compact support. Eq. 2.26 is rewritten as follows:

$$J(\boldsymbol{x}) = \left[\boldsymbol{P}\boldsymbol{a}(\boldsymbol{x}) - \boldsymbol{u}\right]^{\mathrm{T}} \boldsymbol{W}(\boldsymbol{x}) \left[\boldsymbol{P}\boldsymbol{a}(\boldsymbol{x}) - \boldsymbol{u}\right], \tag{2.27}$$

with

$$\boldsymbol{u} = \begin{bmatrix} u_1 \\ \vdots \\ u_n \end{bmatrix}, \quad \boldsymbol{P} = \begin{bmatrix} p_1(\boldsymbol{x}_1) & \cdots & p_m(\boldsymbol{x}_1) \\ \vdots & \ddots & \vdots \\ p_1(\boldsymbol{x}_n) & \cdots & p_m(\boldsymbol{x}_n) \end{bmatrix} \quad \text{and}$$

$$\boldsymbol{W}(\boldsymbol{x}) = \begin{bmatrix} W(\boldsymbol{x} - \boldsymbol{x}_1, d) & 0 & \cdots & 0 \\ 0 & W(\boldsymbol{x} - \boldsymbol{x}_2, d) & \cdots & 0 \\ \vdots & \vdots & \ddots & \vdots \\ 0 & 0 & \cdots & W(\boldsymbol{x} - \boldsymbol{x}_n, d) \end{bmatrix}. \tag{2.28}$$

The values of the coefficients $\boldsymbol{a}(\boldsymbol{x})$ are found by minimizing the discrete L_2 norm. The minimum is determined by taking the derivative of the functional $J(\boldsymbol{x})$ with respect to each term in $\boldsymbol{a}(\boldsymbol{x})$ and equal to zero i.e., $\frac{\partial J(\boldsymbol{x})}{\partial a_l(\boldsymbol{x})} = 0$ for $l = 1...m$:

$$\sum_{I=1}^{k} W(\boldsymbol{x} - \boldsymbol{x}^I, d) 2\boldsymbol{p}(\boldsymbol{x}^I) \left[\boldsymbol{p}^{\mathrm{T}}(\boldsymbol{x}^I)\boldsymbol{a}(\boldsymbol{x}) - u^I\right] = 0 \tag{2.29}$$

or

$$\sum_{I=1}^{k} W(\boldsymbol{x} - \boldsymbol{x}^I, d)\boldsymbol{p}(\boldsymbol{x}^I)\boldsymbol{p}^{\mathrm{T}}(\boldsymbol{x}^I)\boldsymbol{a}(\boldsymbol{x}) = \sum_{I=1}^{k} W(\boldsymbol{x} - \boldsymbol{x}^I, d)\boldsymbol{p}(\boldsymbol{x}^I)u^I. \tag{2.30}$$

Eq. 2.30 can be rewritten in matrix notation as

$$\boldsymbol{A}(\boldsymbol{x})\boldsymbol{a}(\boldsymbol{x}) = \boldsymbol{B}(\boldsymbol{x})\boldsymbol{u}, \tag{2.31}$$

with

$$\boldsymbol{A}(\boldsymbol{x}) = \boldsymbol{P}^{\mathrm{T}}\boldsymbol{W}(\boldsymbol{x})\boldsymbol{P} = \sum_{I=1}^{k} W(\boldsymbol{x} - \boldsymbol{x}^I, d)\boldsymbol{p}(\boldsymbol{x}^I)\boldsymbol{p}^{\mathrm{T}}(\boldsymbol{x}^I) \tag{2.32}$$

and

$$\boldsymbol{B}(\boldsymbol{x}) = \boldsymbol{P}^{\mathrm{T}}\boldsymbol{W}(\boldsymbol{x}) = \sum_{I=1}^{k} W(\boldsymbol{x} - \boldsymbol{x}^I, d)\boldsymbol{p}(\boldsymbol{x}^I). \tag{2.33}$$

The coefficients $\boldsymbol{a}(\boldsymbol{x})$ are found by solving Eq. 2.31 according to

$$\boldsymbol{a}(\boldsymbol{x}) = \boldsymbol{A}^{-1}(\boldsymbol{x})\boldsymbol{B}(\boldsymbol{x})\boldsymbol{u}. \tag{2.34}$$

The approximation from Eq. 2.23 can be rewritten by substituting the vector $\boldsymbol{a}(\boldsymbol{x})$ with Eq. 2.34. With the use of the general formulation for the approximation (Eq. 2.1), Eq. 2.23 becomes

$$u^h(\boldsymbol{x}) = \boldsymbol{p}^{\mathrm{T}}(\boldsymbol{x})\boldsymbol{A}^{-1}(\boldsymbol{x})\boldsymbol{B}(\boldsymbol{x})\boldsymbol{u} = \sum_{I=1}^{k} \phi^I(\boldsymbol{x})u^I, \tag{2.35}$$

where the shape function $\phi^I(\boldsymbol{x})$ equals

$$\begin{aligned} \phi^I(\boldsymbol{x}) &= \boldsymbol{p}^{\mathrm{T}}(\boldsymbol{x})\boldsymbol{A}^{-1}(\boldsymbol{x})W(\boldsymbol{x} - \boldsymbol{x}^I, d)\boldsymbol{p}(\boldsymbol{x}^I) \\ &= \boldsymbol{c}^{\mathrm{T}}(\boldsymbol{x})W(\boldsymbol{x} - \boldsymbol{x}^I, d)\boldsymbol{p}(\boldsymbol{x}^I) \end{aligned} \tag{2.36}$$

with

$$\boldsymbol{c}(\boldsymbol{x}) = \boldsymbol{A}^{-1}(\boldsymbol{x})\boldsymbol{p}(\boldsymbol{x}). \tag{2.37}$$

The derivative $u_{,j}(x)$ of a scalar function $u(\boldsymbol{x})$ is found according to Eq. 2.2. Thus, in the MLS approximation it is only necessary to take the derivative of the shape function from Eq. 2.36, which equals

$$\phi^I_{,j}(\boldsymbol{x}) = \boldsymbol{c}^{\mathrm{T}}_{,j}(\boldsymbol{x})W(\boldsymbol{x} - \boldsymbol{x}^I, d)\boldsymbol{p}(\boldsymbol{x}^I) + \boldsymbol{c}^{\mathrm{T}}(\boldsymbol{x})W_{,j}(\boldsymbol{x} - \boldsymbol{x}^I, d)\boldsymbol{p}(\boldsymbol{x}^I) \tag{2.38}$$

with

$$\begin{aligned} \boldsymbol{c}_{,j}(\boldsymbol{x}) &= \left[\boldsymbol{A}^{-1}\right]_{,j}(\boldsymbol{x})\boldsymbol{p}(\boldsymbol{x}) + \boldsymbol{A}^{-1}(\boldsymbol{x})\boldsymbol{p}_{,j}(\boldsymbol{x}) \\ &= -\boldsymbol{A}^{-1}(\boldsymbol{x})\boldsymbol{A}_{,j}(\boldsymbol{x})\boldsymbol{A}^{-1}(\boldsymbol{x})\boldsymbol{p}(\boldsymbol{x}) + \boldsymbol{A}^{-1}(\boldsymbol{x})\boldsymbol{p}_{,j}(\boldsymbol{x}) \\ &= -\boldsymbol{A}^{-1}(\boldsymbol{x})\left[\boldsymbol{A}_{,j}(\boldsymbol{x})\boldsymbol{c}(\boldsymbol{x}) + \boldsymbol{p}_{,j}(\boldsymbol{x})\right], \end{aligned} \tag{2.39}$$

in which the derivative of the kernel function can be calculated analytically (see Sec. 2.1.2) and the derivative of $\boldsymbol{p}(\boldsymbol{x})$ is simply a vector containing the derivative of each individual term.

Similarity between MLS and kernel approximation

As mentioned before, the MLS approximation is a more general formulation of the kernel approximation. However, the formulations of the shape functions given in Eq. 2.10 and Eq. 2.36 apparently do not match. In one particular case, the formulation of the shape function in the MLS and kernel approximation coincide. This is explained below, starting from the MLS shape function.

Consider the monomial vector $\boldsymbol{p}(\boldsymbol{x})$ to contain a constant i.e., $\boldsymbol{p}(\boldsymbol{x}) = 1$. Eq. 2.36 is then written as

$$\phi^I(\boldsymbol{x}) = \boldsymbol{p}^{\mathrm{T}}(\boldsymbol{x})\boldsymbol{A}^{-1}(\boldsymbol{x})W(\boldsymbol{x}-\boldsymbol{x}^I,d)\boldsymbol{p}(\boldsymbol{x}^I) = \boldsymbol{A}^{-1}(\boldsymbol{x})W(\boldsymbol{x}-\boldsymbol{x}^I,d). \tag{2.40}$$

Next, Eq. 2.32 can be written as

$$\boldsymbol{A}(\boldsymbol{x}) = \sum_{J=1}^{k} W(\boldsymbol{x}-\boldsymbol{x}^J,d)\boldsymbol{p}(\boldsymbol{x}^J)\boldsymbol{p}^{\mathrm{T}}(\boldsymbol{x}^J) = \sum_{J=1}^{k} W(\boldsymbol{x}-\boldsymbol{x}^J,d). \tag{2.41}$$

When combining these two equations, this results in

$$\phi^I(\boldsymbol{x}) = \frac{W(\boldsymbol{x}-\boldsymbol{x}^I,d)}{\sum_{J=1}^{k} W(\boldsymbol{x}-\boldsymbol{x}^J,d)}. \tag{2.42}$$

The shape function in the kernel approximation (Eq. 2.10) has previously been defined as

$$\phi^I(\boldsymbol{x}) = \frac{m^I W(\boldsymbol{x}-\boldsymbol{x}^I,d)}{\sum_{J=1}^{k} m^J W(\boldsymbol{x}-\boldsymbol{x}^J,d)}. \tag{2.43}$$

The formulation of the MLS shape function and kernel shape function in Eq. 2.42 and Eq. 2.43 coincide when the weight m for each node equals one. In conclusion, the simplest form of the MLS approximation is the kernel approximation. The MLS approximation provides more consistent results when increasing the number of terms in the monomial vector $\boldsymbol{p}(\boldsymbol{x})$.

Solution to the one-dimensional exemplary problem

The MLS approximation is used to approximate the scalar function $u(x)$ and its derivative $u_{,x}(x)$ from Fig. 2.1. Although no mesh is required, the size d of the

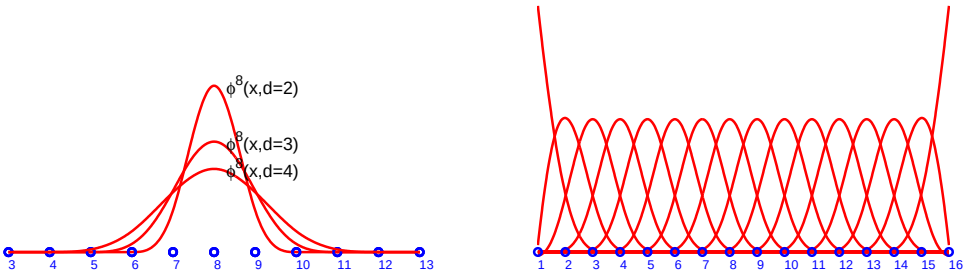

(a) ϕ^8 (b) All shape functions ϕ^I for $I = 1...16$

Figure 2.8: MLS shape function ϕ^I for the center node $I = 8$ for $d = 2, 3, 4$ and shape functions ϕ^I for all nodes, i.e. $I = 1...16$, and $d = 2$.

influence domain of the kernel function has to be given. This size will affect the accuracy of the approximation. Therefore, the approximation from Eq. 2.3 is compared for different sizes $d = 2, 3, 4$. The choice of monomials in $\boldsymbol{p}(\boldsymbol{x})$ also affects the approximation, therefore a linear and quadratic basis are compared as well. The cubic spline weight function is chosen as the kernel function (see Sec. 2.1.2).

First, the shape function corresponding to the center node $I = 8$ is shown in Fig. 2.8 for $d = 2, 3, 4$ and a linear monomial basis. The shape function for each node is also given, with $d = 2$. Since the number of nodes decreases near the boundary, the values of the shape function increase near the boundary.

By the use of the shape functions and their derivatives, the scalar function Eq. 2.3 and its derivative Eq. 2.4 are approximated with a discrete number of nodes according to Eq. 2.35. The approximations of the scalar function and its derivative are shown in Fig. 2.9a and Fig. 2.9b, with $d = 2, 3, 4$ and a linear basis. In Fig. 2.9c and Fig. 2.9d the approximations of the scalar function and its derivative are shown, with $d = 3$ and a linear or quadratic basis. Note that for the MLS approximation, the Kronecker delta criterion $u^h(\boldsymbol{x}_i) = u_i$ does not hold. This can be seen in Fig. 2.9a and Fig. 2.9c, where the approximation does not intersect the scalar values at the nodes.

2.2 Discretization of the linear elasticity problem

This section introduces two meshless methods, which are based on the MLS approximation (Sec. 2.1.3). The MLS approximation is utilized to discretize the governing equations for a linear elastic two-dimensional solid. However, there are

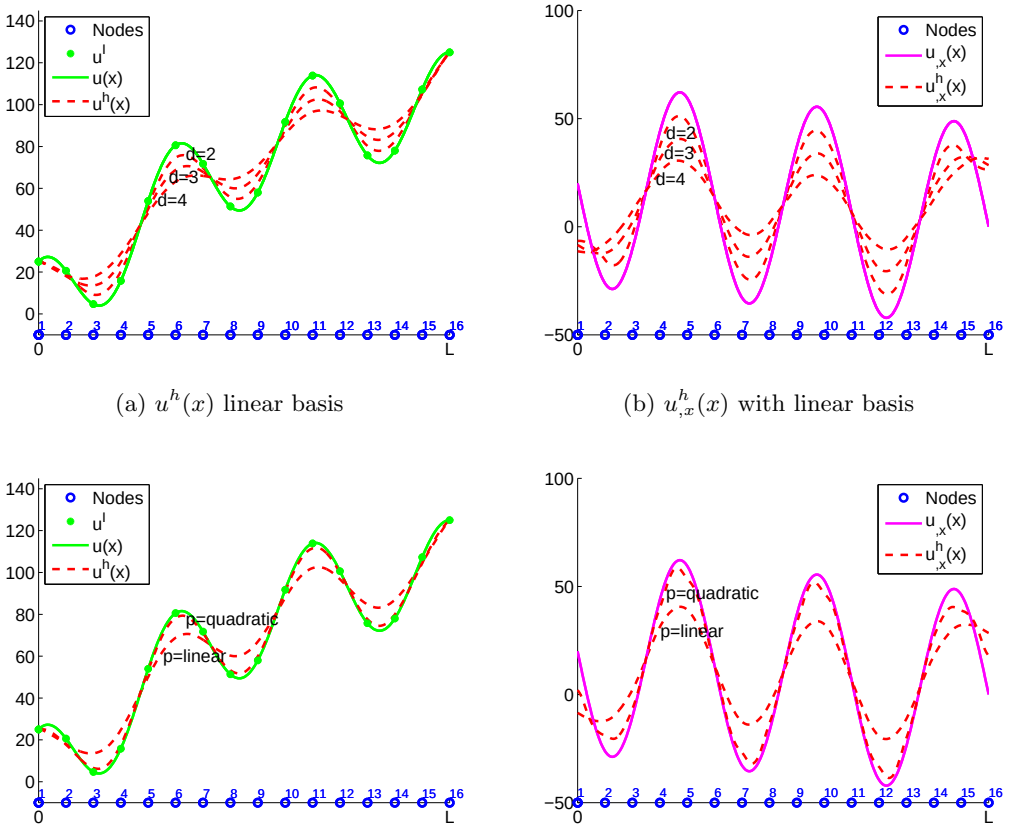

(a) $u^h(x)$ linear basis

(b) $u^h_{,x}(x)$ with linear basis

(c) $u^h(x)$ with $d = 3$

(d) $u^h_{,x}(x)$ with $d = 3$

Figure 2.9: The approximation of the scalar function $u(x)$ and its derivative $u^h_{,x}(x)$ with the MLS approximation. Both functions are given in Eq. 2.3 and Eq. 2.4. The domain is discretized with sixteen equally spaced nodes, and the approximation is calculated for different meshless parameters d and monomial basis $\boldsymbol{p}$.

several forms of these linear elastic equations, and this is exactly where the two meshless methods differ from each other. Sec. 2.2.1 discusses the EFG method, developed by Belytschko et al. [12]. This method is based on the weak form of the linear elastic equations and requires a background mesh for the integration. Sec. 2.2.2 discusses the more recent MLPG method, developed by Atluri and Zhu [40], [22]. The MLPG framework is based on a local weak form of the linear elastic equations. To avoid integration, the mixed collocation form is adopted [41], [39].

2.2.1 EFG method

The EFG method was proposed in 1994 by Belytschko et al. [12]. The formulation of the EFG method has undergone some slight changes in order to be suitable for multiple applications [14], [15], [13], [44]. In the EFG method, the linear elastic equations are discretized by utilizing the MLS approximation. In this section, first the linear elastic equations and the weak form on which the EFG method will be applied are recalled. Second, the linear elastic equations are discretized using the EFG method. The enforcement of essential boundary conditions is discussed next. Finally, the evaluation of the integrals present in the discretized equations is discussed.

Linear elastic equations

The governing equations for a linear elastic solid, which occupies a domain Ω bounded by Γ, are given by

$$\begin{cases} \boldsymbol{L}^{\mathrm{T}}\boldsymbol{\sigma} + \boldsymbol{b} = 0 & \text{in} \quad \Omega \\ \boldsymbol{\sigma}\boldsymbol{n} = \bar{\boldsymbol{t}} & \text{on} \quad \Gamma_t \\ \boldsymbol{u} = \bar{\boldsymbol{u}} & \text{on} \quad \Gamma_u \end{cases}, \tag{2.44}$$

where $\boldsymbol{L}$ is the differential operator, $\boldsymbol{\sigma}$ is the stress vector, $\boldsymbol{b}$ is the body force vector, $\boldsymbol{n}$ is the normal vector on boundary Γ_t, $\bar{\boldsymbol{t}}$ is the prescribed traction on boundary Γ_t, $\boldsymbol{u}$ is the displacement vector and $\bar{\boldsymbol{u}}$ is the prescribed displacement on boundary Γ_u. In two dimensions the vectors and matrices are

$$\boldsymbol{u} = \begin{bmatrix} u_1(\boldsymbol{x}) \\ u_2(\boldsymbol{x}) \end{bmatrix}, \quad \boldsymbol{\sigma} = \begin{bmatrix} \sigma_{11}(\boldsymbol{x}) \\ \sigma_{22}(\boldsymbol{x}) \\ \sigma_{12}(\boldsymbol{x}) \end{bmatrix}, \quad \boldsymbol{b} = \begin{bmatrix} b_1(\boldsymbol{x}) \\ b_2(\boldsymbol{x}) \end{bmatrix}, \quad \bar{\boldsymbol{u}} = \begin{bmatrix} \bar{u}_1(\boldsymbol{x}) \\ \bar{u}_2(\boldsymbol{x}) \end{bmatrix}, \quad \bar{\boldsymbol{t}} = \begin{bmatrix} \bar{t}_1(\boldsymbol{x}) \\ \bar{t}_2(\boldsymbol{x}) \end{bmatrix},$$

$$\boldsymbol{n} = \begin{bmatrix} \bar{n}_1(\boldsymbol{x}) \\ \bar{n}_2(\boldsymbol{x}) \end{bmatrix} \quad \text{and} \quad \boldsymbol{L} = \begin{bmatrix} \partial/\partial x_1 & 0 \\ 0 & \partial/\partial x_2 \\ \partial/\partial x_2 & \partial/\partial x_1, \end{bmatrix} \tag{2.45}$$

where $\boldsymbol{x} = \begin{bmatrix} x_1 & x_2 \end{bmatrix}^{\mathrm{T}}$. For a two-dimensional linear isotropic plain stress material, the constitutive equations are

$$\boldsymbol{\sigma} = \boldsymbol{D}\boldsymbol{\epsilon} \quad \text{with} \quad \boldsymbol{D} = \frac{E}{1-\nu^2} \begin{bmatrix} 1 & \nu & 0 \\ \nu & 1 & 0 \\ 0 & 0 & 1 \end{bmatrix} \quad \text{and} \quad \boldsymbol{\epsilon} = \boldsymbol{L}\boldsymbol{u}, \tag{2.46}$$

where $\boldsymbol{\epsilon}$ is the strain in the material, $\boldsymbol{D}$ is a matrix containing the material properties, E is the Young's modulus and ν is the Poisson's ratio.[2]

The EFG method is based on the weak form of Eq. 2.44, which can be found by applying the principle of minimal potential energy [20]. The weak form is determined by multiplying the linear elasticity equations with a test function $\boldsymbol{v}$ and integrating this multiplication over the problem domain Ω:

$$\int_\Omega \{\boldsymbol{v}^{\mathrm{T}}\boldsymbol{L}^{\mathrm{T}}\boldsymbol{\sigma} + \boldsymbol{v}^{\mathrm{T}}\boldsymbol{b}\} d\Omega = 0 \tag{2.47}$$

or

$$\int_\Omega \left[\boldsymbol{L}\delta\boldsymbol{u}\right]^{\mathrm{T}} \boldsymbol{D} \left[\boldsymbol{L}\boldsymbol{u}\right] d\Omega - \int_\Omega \delta\boldsymbol{u}^{\mathrm{T}}\boldsymbol{b} d\Omega - \int_{\Gamma_t} \delta\boldsymbol{u}^{\mathrm{T}}\bar{\boldsymbol{t}} d\Gamma = 0, \tag{2.48}$$

where in the EFG method the test function $\boldsymbol{v}$ is chosen to be similar to the displacement $\boldsymbol{u}$ and $\delta\boldsymbol{u}$ corresponds to infinitesimal variations of the displacement.

Discretization of the weak form

An approximation of the displacement $\boldsymbol{u}$ is found by discretizing Eq. 2.47 with the MLS approximation (Sec. 2.1.3). With the use of the general formulation for the shape functions (Eq. 2.1), the approximation of the displacement is written as

$$\boldsymbol{u} = \begin{bmatrix} u_1(\boldsymbol{x}) \\ u_2(\boldsymbol{x}) \end{bmatrix} \approx \begin{bmatrix} u_1^h(\boldsymbol{x}) \\ u_2^h(\boldsymbol{x}) \end{bmatrix} = \begin{bmatrix} \sum_{I=1}^k \phi^I(\boldsymbol{x})\hat{u}_1^{hI} \\ \sum_{I=1}^k \phi^I(\boldsymbol{x})\hat{u}_2^{hI} \end{bmatrix} = \sum_{I=1}^k \boldsymbol{\Phi}^I \hat{\boldsymbol{u}}^{hI}$$

[2]Further in the text the two-dimensional linear isotropic plain stress linear elasticity equations will be referred to as the linear elasticity equations.

$$= \begin{bmatrix} \phi^1(\boldsymbol{x}) & 0 & \dots & \phi^k(\boldsymbol{x}) & 0 \\ 0 & \phi^1(\boldsymbol{x}) & \dots & 0 & \phi^k(\boldsymbol{x}) \end{bmatrix} \begin{bmatrix} \hat{u}_1^{h1} \\ \hat{u}_2^{h1} \\ \vdots \\ \hat{u}_1^{hk} \\ \hat{u}_2^{hk} \end{bmatrix} = \boldsymbol{\Phi}\hat{\boldsymbol{u}}^h, \qquad (2.49)$$

with

$$\boldsymbol{\Phi}^I = \begin{bmatrix} \phi^I(\boldsymbol{x}) & 0 \\ 0 & \phi^I(\boldsymbol{x}) \end{bmatrix} \quad \text{and} \quad \hat{\boldsymbol{u}}^{hI} = \begin{bmatrix} \hat{u}_1^{hI} \\ \hat{u}_2^{hI} \end{bmatrix}. \qquad (2.50)$$

Here, $\hat{\boldsymbol{u}}^h$ is the vector containing the approximated nodal displacement $\hat{u}_i^{hI}$ (for $i = 1, 2$ and $I = 1...k$) and $\boldsymbol{\Phi}$ is the matrix containing all shape functions at $\boldsymbol{x}$ of the nodes within the support domain Ω^x. In the MLS approximation the shape functions are given by Eq. 2.36.[3] Similarly, the infinitesimal displacement $\delta\boldsymbol{u}$ is approximated according to

$$\delta\boldsymbol{u} \approx \sum_{I=1}^{k} \boldsymbol{\Phi}^I \delta\hat{\boldsymbol{u}}^{hI} \quad \text{with} \quad \delta\hat{\boldsymbol{u}}^{hI} = \begin{bmatrix} \delta\hat{u}_1^{h1} \\ \delta\hat{u}_2^{h1} \\ \vdots \\ \delta\hat{u}_1^{hk} \\ \delta\hat{u}_2^{hk} \end{bmatrix}. \qquad (2.51)$$

The derivative of the displacement $\boldsymbol{L}\boldsymbol{u}$ is approximated as

$$\boldsymbol{L}\boldsymbol{u} \approx \boldsymbol{L}\boldsymbol{\Phi}\hat{\boldsymbol{u}}^h = \begin{bmatrix} \partial/\partial x_1 & 0 \\ 0 & \partial/\partial x_2 \\ \partial/\partial x_2 & \partial/\partial x_1 \end{bmatrix} \begin{bmatrix} \phi^1(\boldsymbol{x}) & 0 & \dots & \phi^k(\boldsymbol{x}) & 0 \\ 0 & \phi^1(\boldsymbol{x}) & \dots & 0 & \phi^k(\boldsymbol{x}) \end{bmatrix} \begin{bmatrix} \hat{u}_1^{h1} \\ \hat{u}_2^{h1} \\ \vdots \\ \hat{u}_1^{hk} \\ \hat{u}_2^{hk} \end{bmatrix}$$

$$= \begin{bmatrix} \phi^1_{,1}(\boldsymbol{x}) & 0 & \dots & \phi^k_{,1}(\boldsymbol{x}) & 0 \\ 0 & \phi^1_{,2}(\boldsymbol{x}) & \dots & 0 & \phi^k_{,2}(\boldsymbol{x}) \\ \phi^1_{,2}(\boldsymbol{x}) & \phi^1_{,1}(\boldsymbol{x}) & \dots & \phi^k_{,2}(\boldsymbol{x}) & \phi^k_{,1}(\boldsymbol{x}) \end{bmatrix} \begin{bmatrix} \hat{u}_1^{h1} \\ \hat{u}_2^{h1} \\ \vdots \\ \hat{u}_1^{hk} \\ \hat{u}_2^{hk} \end{bmatrix}$$

[3] The formulation of the MLS approximation from Eq. 2.36 is slightly altered, i.e. u_i^I is replaced with $\hat{u}_i^{hI}$. The approximation in the EFG method is not based on smoothing the exact nodal displacement, but it smoothes an approximated nodal displacement, which is found by solving a set of equations. Since the Kronecker delta criterion $u_i^I = u_i^{hI}$ does not hold, the approximated displacement values u_i^{hI} are replaced with approximated virtual nodal values $\hat{u}_i^{hI}$.

$$= \boldsymbol{B}\hat{\boldsymbol{u}}^h = \sum_{I=1}^{k} \boldsymbol{B}^I \hat{\boldsymbol{u}}^{hI}, \tag{2.52}$$

with

$$\boldsymbol{B}^I = \begin{bmatrix} \phi^I_{,1}(\boldsymbol{x}) & 0 \\ 0 & \phi^I_{,2}(\boldsymbol{x}) \\ \phi^I_{,2}(\boldsymbol{x}) & \phi^I_{,1}(\boldsymbol{x}) \end{bmatrix}, \tag{2.53}$$

where $\boldsymbol{B}^I$ is the strain-displacement matrix of node I at coordinate $\boldsymbol{x}$.

The approximation of the individual elements from Eq. 2.47 is now known, and the next step is to combine these elements. Using Eq. 2.52 and Eq. 2.54 the first term in Eq. 2.48 becomes

$$\begin{aligned} \int_\Omega \delta \left[\boldsymbol{L}\boldsymbol{u}\right]^{\mathrm{T}} \boldsymbol{D} \left[\boldsymbol{L}\boldsymbol{u}\right] d\Omega &= \int_\Omega \left[\sum_{I=1}^{k} \boldsymbol{B}^I \delta\hat{\boldsymbol{u}}^{hI}\right]^{\mathrm{T}} \boldsymbol{D} \left[\sum_{J=1}^{k} \boldsymbol{B}^J \hat{\boldsymbol{u}}^{hJ}\right] d\Omega \\ &= \int_\Omega \sum_{I=1}^{k}\sum_{J=1}^{k} \left[\delta\hat{\boldsymbol{u}}^{hI}\right]^{\mathrm{T}} \left[\left\{\boldsymbol{B}^I\right\}^{\mathrm{T}} \boldsymbol{D}\boldsymbol{B}^J\right] \hat{\boldsymbol{u}}^{hJ} d\Omega \\ &= \sum_{I=1}^{k}\sum_{J=1}^{k} \left[\delta\hat{\boldsymbol{u}}^{hI}\right]^{\mathrm{T}} \left[\int_\Omega \left\{\boldsymbol{B}^I\right\}^{\mathrm{T}} \boldsymbol{D}\boldsymbol{B}^J d\Omega\right] \hat{\boldsymbol{u}}^{hJ}. \end{aligned} \tag{2.54}$$

Until this point, the summation is according to a local numbering within the support domain of each coordinate. From this stage, a global numbering system is adopted, in which the nodes in the global domain Ω are denoted by the numbers $I = 1...n$. With the global numbering, Eq. 2.54 can be rewritten as

$$\begin{aligned} \int_\Omega \delta \left[\boldsymbol{L}\boldsymbol{u}\right]^{\mathrm{T}} \boldsymbol{D} \left[\boldsymbol{L}\boldsymbol{u}\right] d\Omega &= \sum_{I=1}^{n}\sum_{J=1}^{n} \left[\delta\hat{\boldsymbol{u}}^{hI}\right]^{\mathrm{T}} \boldsymbol{K}^{IJ} \hat{\boldsymbol{u}}^{hJ} \\ &= \left\{\delta\hat{\boldsymbol{U}}^h\right\}^{\mathrm{T}} \boldsymbol{K}\hat{\boldsymbol{U}}^h, \end{aligned} \tag{2.55}$$

where

$$\boldsymbol{K}^{IJ} = \int_\Omega \left[\boldsymbol{B}^I\right]^{\mathrm{T}} \boldsymbol{D}\boldsymbol{B}^J d\Omega, \quad \boldsymbol{K} = \begin{bmatrix} \boldsymbol{K}_{11} & \dots & \boldsymbol{K}_{1n} \\ \vdots & \ddots & \vdots \\ \boldsymbol{K}_{n1} & \dots & \boldsymbol{K}_{nn} \end{bmatrix} \quad \text{and}$$

$$\hat{\boldsymbol{U}}^h = \begin{bmatrix} \hat{u}_1^{1h} \\ \hat{u}_2^{1h} \\ \vdots \\ \hat{u}_1^{nh} \\ \hat{u}_2^{nh} \end{bmatrix}. \tag{2.56}$$

$\boldsymbol{K}^{IJ}$ and $\boldsymbol{K}$ are often called respectively the nodal and global stiffness matrix. The second term in Eq. 2.48 can be rewritten as

$$\begin{aligned} \int_\Omega \delta \boldsymbol{u}^{\mathrm{T}} \boldsymbol{b} d\Omega &= \int_\Omega \left[\sum_{I=1}^{k} \boldsymbol{\Phi}^I \delta \hat{\boldsymbol{u}}^{hI} \right]^{\mathrm{T}} \boldsymbol{b} d\Omega = \sum_{I=1}^{k} \left[\delta \hat{\boldsymbol{u}}^{hI} \right]^{\mathrm{T}} \int_\Omega \left[\boldsymbol{\Phi}^I \right]^{\mathrm{T}} \boldsymbol{b} d\Omega \\ &= \sum_{I=1}^{k} \left[\delta \hat{\boldsymbol{u}}^{hI} \right]^{\mathrm{T}} \boldsymbol{F}_b^I = \left[\delta \hat{\boldsymbol{U}}^h \right]^{\mathrm{T}} \boldsymbol{F}_b, \end{aligned} \tag{2.57}$$

where

$$\boldsymbol{F}_b^I = \int_\Omega \left[\boldsymbol{\Phi}^I \right]^{\mathrm{T}} \boldsymbol{b} d\Omega \quad \text{and} \quad \boldsymbol{F}_b = \begin{bmatrix} \boldsymbol{F}_b^1 \\ \vdots \\ \boldsymbol{F}_b^n \end{bmatrix}. \tag{2.58}$$

The force vectors $\boldsymbol{F}_b^I$ and $\boldsymbol{F}_b$ are consecutively called the nodal body force vector and the body force vector. Similarly as in Eq. 2.57, the third term in Eq. 2.48 can be replaced by

$$\int_{\Gamma_t} \delta \boldsymbol{u}^{\mathrm{T}} \bar{\boldsymbol{t}} d\Omega = \sum_{I=1}^{n} \left[\delta \hat{\boldsymbol{u}}^{hI} \right]^{\mathrm{T}} \boldsymbol{F}_t^I = \left[\delta \hat{\boldsymbol{U}}^h \right]^{\mathrm{T}} \boldsymbol{F}_t, \tag{2.59}$$

where the force vector $\boldsymbol{F}_t^I$ is often called the nodal traction vector and $\boldsymbol{F}_t$ is often called the traction force vector, equal to

$$\boldsymbol{F}_t^I = \int_{\Gamma_t} \left[\boldsymbol{\Phi}^I \right]^{\mathrm{T}} \bar{\boldsymbol{t}} d\Omega \quad \text{and} \quad \boldsymbol{F}_t = \begin{bmatrix} \boldsymbol{F}_t^1 \\ \vdots \\ \boldsymbol{F}_t^n \end{bmatrix}. \tag{2.60}$$

The Galerkin weak form in Eq. 2.48 can be rewritten by substituting Eq. 2.54, Eq. 2.57 and 2.59. The discretized formulation of Eq. 2.48 is then given by

$$\left[\delta \hat{\boldsymbol{U}}^h \right]^{\mathrm{T}} \boldsymbol{K} \hat{\boldsymbol{U}}^h - \left[\delta \hat{\boldsymbol{U}}^h \right]^{\mathrm{T}} \boldsymbol{F}^b - \left[\delta \hat{\boldsymbol{U}}^h \right]^{\mathrm{T}} \boldsymbol{F}^t = 0$$

$$\left[\delta\hat{\boldsymbol{U}}^h\right]^{\mathrm{T}}\left[\boldsymbol{K}\hat{\boldsymbol{U}}^h-\boldsymbol{F}_b-\boldsymbol{F}_t\right]=0, \tag{2.61}$$

in which $\delta\boldsymbol{u}^{\mathrm{T}}$ can be chosen arbitrary. Then the following condition holds

$$\boldsymbol{K}\hat{\boldsymbol{U}}^h=\boldsymbol{F}, \tag{2.62}$$

where $\boldsymbol{F}=\boldsymbol{F}_b+\boldsymbol{F}_t$ is the global force vector. Eq. 2.62 is the well-known discretized form of the linear elasticity problem. The displacements $\hat{\boldsymbol{U}}^h$ can be obtained from this equation. Moreover, the approximated strain and stress can then be determined by

$$\boldsymbol{\epsilon}^h(\boldsymbol{x})=\sum_{J=1}^{k}\boldsymbol{B}^J\hat{\boldsymbol{u}}^{hJ} \tag{2.63}$$

and

$$\boldsymbol{\sigma}^h(\boldsymbol{x})=\sum_{J=1}^{k}\boldsymbol{D}\boldsymbol{B}^J\hat{\boldsymbol{u}}^{hJ}. \tag{2.64}$$

There are two large differences between FEM and the EFG method, namely the formulation of the shape functions, and the lack of the Kronecker delta criterion. Because the Kronecker delta criterion is not met, the displacement vector $\hat{\boldsymbol{U}}^h$ contains the approximated virtual nodal displacement. The actual nodal displacement can be found by substituting the virtual nodal displacement in Eq. 2.1 and Eq. 2.2. Moreover, the essential boundary conditions (displacement boundary conditions) cannot be applied directly to the global stiffness matrix K, because Eq. 2.62 is expressed in the virtual nodal displacement. A solution to this last problem is provided next.

Enforcement of essential boundary conditions

The enforcement of the essential boundary conditions in the EFG method is not as simple as in FEM. This is because the Kronecker delta criterion does not hold for the MLS shape functions used in the EFG method and because Eq. 2.62 is expressed in terms of the virtual nodal displacement. To overcome this problem, the essential boundary conditions are enforced using the Lagrange multipliers method [14], [12].

By adding two extra terms in the weak form (Eq. 2.48), the essential boundary conditions can be taken into account. The constrained weak form, which takes

into account these essential boundary conditions, equals

$$\int_{\Omega} [\boldsymbol{L}\boldsymbol{u}]^{\mathrm{T}} \boldsymbol{D} [\boldsymbol{L}\boldsymbol{u}] \, d\Omega - \int_{\Omega} \boldsymbol{u}^{\mathrm{T}} \boldsymbol{b} d\Omega - \int_{\Gamma_t} \boldsymbol{u}^{\mathrm{T}} \bar{\boldsymbol{t}} d\Gamma - \int_{\Gamma_u} \delta\boldsymbol{\lambda}^{\mathrm{T}} [\boldsymbol{u} - \bar{\boldsymbol{u}}] \, d\Gamma - \int_{\Gamma_u} \delta\boldsymbol{u}^{\mathrm{T}} \boldsymbol{\lambda} d\Gamma = 0. \tag{2.65}$$

Discretization of the constrained weak form is similar to discretization of the weak form (Eq. 2.48). However, the two extra terms corresponding to the Lagrange multipliers method also need to be approximated. First, the displacement $\boldsymbol{u}$ is approximated according to Eq. 2.49. Second, the Lagrange multipliers $\boldsymbol{\lambda}$ and $\delta\boldsymbol{\lambda}$ are approximated along the boundary Γ_u. The approximation of the Lagrange multipliers is given by

$$\boldsymbol{\lambda} \approx \begin{bmatrix} \lambda_1^h \\ \lambda_2^h \end{bmatrix} = \sum_{K=1}^{k_b} \boldsymbol{N}^K \hat{\boldsymbol{\lambda}}^{hK} \tag{2.66}$$

$$\delta\boldsymbol{\lambda} \approx \begin{bmatrix} \delta\lambda_1^h \\ \delta\lambda_2^h \end{bmatrix} = \sum_{K=1}^{k_b} \boldsymbol{N}^K \delta\hat{\boldsymbol{\lambda}}^{hK}, \tag{2.67}$$

in which

$$\boldsymbol{N}^K = \begin{bmatrix} N^K(\boldsymbol{x}) & 0 \\ 0 & N^K(\boldsymbol{x}) \end{bmatrix} \quad \text{and} \quad \hat{\boldsymbol{\lambda}}^{hK} = \begin{bmatrix} \hat{\lambda}_1^{hK} \\ \hat{\lambda}_2^{hK} \end{bmatrix}. \tag{2.68}$$

Here $\boldsymbol{x} \in \Gamma_u$, k_b is the number of nodes on the boundary in the support domain Ω^x of coordinate $\boldsymbol{x}$, $N^K(\boldsymbol{x})$ is the value of the shape function of boundary node K at $\boldsymbol{x}$, $\hat{\boldsymbol{\lambda}}^{hK} = \hat{\boldsymbol{\lambda}}(\boldsymbol{x}^K)$ and $\delta\hat{\boldsymbol{\lambda}}^{hK} = \delta\hat{\boldsymbol{\lambda}}(\boldsymbol{x}^K)$.[4] Third and last, the two extra terms in Eq. 2.65 are rewritten with the approximations for $\boldsymbol{u}$, $\delta\boldsymbol{u}$, $\boldsymbol{\lambda}$ and $\delta\boldsymbol{\lambda}$, resulting in

$$\begin{aligned} -\int_{\Gamma_u} \delta\boldsymbol{\lambda}^{\mathrm{T}} [\boldsymbol{u} - \bar{\boldsymbol{u}}] \, d\Gamma &= -\int_{\Gamma_u} \left[\sum_{K=1}^{k_b} \boldsymbol{N}^K \delta\hat{\boldsymbol{\lambda}}^{hK} \right]^{\mathrm{T}} \left[\sum_{I=1}^{k} \boldsymbol{\Phi}^I \hat{\boldsymbol{u}}^{hI} \right] d\Gamma \\ &\quad + \int_{\Gamma_u} \left[\sum_{K=1}^{k_b} \boldsymbol{N}^K \delta\hat{\boldsymbol{\lambda}}^{hK} \right]^{\mathrm{T}} \bar{\boldsymbol{u}} d\Gamma \\ &= -\sum_{K=1}^{k_b} \sum_{I=1}^{k} \left[\delta\hat{\boldsymbol{\lambda}}^{hK} \right]^{\mathrm{T}} \left[\int_{\Gamma_u} \left\{ \boldsymbol{N}^K \right\}^{\mathrm{T}} \boldsymbol{\Phi}^I d\Gamma \right] \hat{\boldsymbol{u}}^{hI} \end{aligned}$$

[4] The EFG shape functions can be used for $N^K(\boldsymbol{x})$, however in this thesis FEM is used for the boundary shape functions [12].

$$
\begin{aligned}
&+\sum_{K=1}^{k_b}\left[\delta\hat{\boldsymbol{\lambda}}^{hK}\right]^{\mathrm{T}}\left[\int_{\Gamma_u}\left\{\boldsymbol{N}^K\right\}^{\mathrm{T}}\bar{\boldsymbol{u}}d\Gamma\right]\\
&=\sum_{K=1}^{n_b}\sum_{I=1}^{n}\left[\delta\hat{\boldsymbol{\lambda}}^{hK}\right]^{\mathrm{T}}\boldsymbol{G}^{KI}\hat{\boldsymbol{u}}^{hI}-\sum_{K=1}^{k_b}\left[\delta\hat{\boldsymbol{\lambda}}^{hK}\right]^{\mathrm{T}}\boldsymbol{q}^K\\
&=\left[\delta\hat{\boldsymbol{\Lambda}}^{h}\right]^{\mathrm{T}}\boldsymbol{G}^{\mathrm{T}}\hat{\boldsymbol{U}}^{h}-\left[\delta\hat{\boldsymbol{\Lambda}}^{h}\right]^{\mathrm{T}}\boldsymbol{Q}
\end{aligned}
\tag{2.69}
$$

and

$$
\begin{aligned}
-\int_{\Gamma_u}\delta\boldsymbol{u}^{\mathrm{T}}\boldsymbol{\lambda}d\Gamma&=-\int_{\Gamma_u}\left[\sum_{I=1}^{k}\boldsymbol{\Phi}^I\delta\hat{\boldsymbol{u}}^{hI}\right]^{\mathrm{T}}\left[\sum_{K=1}^{k_b}\boldsymbol{N}^K\hat{\boldsymbol{\lambda}}^{hK}\right]d\Gamma\\
&=-\sum_{I=1}^{k}\sum_{K=1}^{k_b}\left[\delta\hat{\boldsymbol{u}}^{hI}\right]^{\mathrm{T}}\left[\int_{\Gamma_u}\left\{\boldsymbol{\Phi}^I\right\}^{\mathrm{T}}\boldsymbol{N}^K d\Gamma\right]\hat{\boldsymbol{\lambda}}^{hK}\\
&=\sum_{I=1}^{k}\sum_{K=1}^{k_b}\left[\delta\hat{\boldsymbol{u}}^{hI}\right]^{\mathrm{T}}\boldsymbol{G}^{IK}\hat{\boldsymbol{\lambda}}^{hK}=\left[\delta\hat{\boldsymbol{U}}^{h}\right]^{\mathrm{T}}\boldsymbol{G}\hat{\boldsymbol{\Lambda}}^{h},
\end{aligned}
\tag{2.70}
$$

in which

$$
\hat{\boldsymbol{\Lambda}}^{h}=\begin{bmatrix}\hat{\lambda}_1^{h1}\\ \hat{\lambda}_2^{h1}\\ \vdots\\ \hat{\lambda}_1^{hn_b}\\ \hat{\lambda}_2^{hn_b}\end{bmatrix},\quad \boldsymbol{G}^{IK}=-\int_{\Gamma_u}\left[\boldsymbol{\Phi}^I\right]^{\mathrm{T}}\boldsymbol{N}^K d\Gamma,\quad \boldsymbol{q}^K=-\int_{\Gamma_u}\left[\boldsymbol{N}^K\right]^{\mathrm{T}}\bar{\boldsymbol{u}}d\Gamma,
$$

$$
\boldsymbol{G}=\begin{bmatrix}\boldsymbol{G}_{11} & \dots & \boldsymbol{G}_{1n_b}\\ \vdots & \ddots & \vdots\\ \boldsymbol{G}_{n1} & \dots & \boldsymbol{G}_{nn_b}\end{bmatrix}\quad\text{and}\quad \boldsymbol{Q}=\begin{bmatrix}q_1^1\\ q_1^2\\ \vdots\\ q_1^{n_b}\\ q_2^{n_b}\end{bmatrix}.
\tag{2.71}
$$

Eq. 2.65 can be approximated by the use of Eq. 2.69 and Eq. 2.70 as

$$
\left[\delta\hat{\boldsymbol{U}}^{h}\right]^{\mathrm{T}}\left[\boldsymbol{K}\hat{\boldsymbol{U}}^{h}+\boldsymbol{G}\hat{\boldsymbol{\Lambda}}^{h}-\boldsymbol{F}_b-\boldsymbol{F}_t\right]+\left[\delta\hat{\boldsymbol{\Lambda}}^{h}\right]^{\mathrm{T}}\left[\boldsymbol{G}^{\mathrm{T}}\hat{\boldsymbol{U}}^{h}-\boldsymbol{Q}\right]=0.
\tag{2.72}
$$

$\delta\boldsymbol{U}^h$ and $\delta\hat{\boldsymbol{\lambda}}$ can be chosen arbitrary, resulting in the following set of equations

$$
\begin{bmatrix}\boldsymbol{K} & \boldsymbol{G}\\ \boldsymbol{G}^{\mathrm{T}} & \boldsymbol{0}\end{bmatrix}\begin{bmatrix}\hat{\boldsymbol{U}}^{h}\\ \hat{\boldsymbol{\Lambda}}^{h}\end{bmatrix}=\begin{bmatrix}\boldsymbol{F}\\ \boldsymbol{Q}\end{bmatrix}.
\tag{2.73}
$$

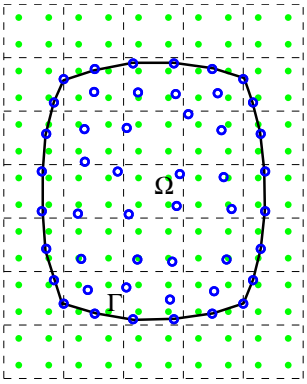

Figure 2.10: An example of a typical problem domain Ω, enclosed by its boundary Γ, the black line. The domain is discretized with nodes (blue circles). A background mesh is defined for integration of the governing equations. The background mesh is constructed of rectangular cells (dashed black lines), each having four integration points (green dots).

Integration

In the final constrained discretized weak form (Eq. 2.73), the integrals have to be evaluated. In order to calculate these integrals, a numerical integration scheme called Gauss quadrature is used [15], [20], [21]. Gauss quadrature can numerically find an approximation of the integral by accumulating the weighted value at integration points. The position of these integration points are placed by a background mesh. Although this background mesh is easier to construct than a typical FEM mesh, it still requires the formation of a cell structure. A detailed explanation of the weights and positions of the integration points within a rectangular cell is given in App. A. In Fig. 2.10 a typical background mesh is shown, with rectangular cells and four integration points in each cell. This figure demonstrates that the background mesh does not have to follow the boundary Ω of the domain.

2.2.2 MLPG mixed collocation method

In 1998, Atluri and Zhu proposed a different method called the Meshless Local Petrov-Galerkin (MLPG) method, which is based on the local weak form [40], [22]. Similar to the EFG method, the MLPG method is based on the MLS approximation. In MLPG, the integrals present in the local weak form are evaluated on sub-domains, therefore no background mesh is needed. Furthermore, the mixed collocation form was introduced [41], [39] to avoid integration. In this section, the MLPG mixed collocation form is explained. First, the local weak form is introduced. Second, the linear elasticity equations are discretized. Last, the ap-

plication of the traction and displacement boundary conditions are discussed.

Linear elasticity problem

The MLPG mixed collocation method is derived by using the weak formulation of the linear elasticity problem (Eq. 2.44) [39], [40], [41], [45]. Different from the EFG method, the test functions are chosen equal to the Dirac delta function, not the displacement:

$$\int_{\Omega} \{\boldsymbol{v}^{\mathrm{T}} \boldsymbol{L}^{\mathrm{T}} \boldsymbol{\sigma} + \boldsymbol{v}^{\mathrm{T}} \boldsymbol{b}\} d\Omega = \int_{\Omega} \{\boldsymbol{\delta}^{\mathrm{T}} \boldsymbol{L}^{\mathrm{T}} \boldsymbol{\sigma} + \boldsymbol{\delta}^{\mathrm{T}} \boldsymbol{b}\} d\Omega = 0. \tag{2.74}$$

The integral is evaluated over n non-overlapping sub-domains Ω_s, where these sub-domains cover the complete domain Ω, leading to

$$\boldsymbol{L}^{\mathrm{T}} \boldsymbol{\sigma}(\boldsymbol{x}^I) + \boldsymbol{b}(\boldsymbol{x}^I) = 0 \quad \text{for} \quad I = 1...n, \tag{2.75}$$

in which

$$\boldsymbol{\delta} = \begin{bmatrix} \delta(\boldsymbol{x} - \boldsymbol{x}^I) \\ \delta(\boldsymbol{x} - \boldsymbol{x}^I) \end{bmatrix}. \tag{2.76}$$

Discretization of the weak form

First, the virtual nodal values in the MLS approximation are expressed in the approximated nodal values. Consider a continuous scalar function $s(\boldsymbol{x})$. The approximation of the scalar function with the MLS approximation at the nodal coordinates is given by

$$s^h(\boldsymbol{x}^I) = s^{hI} = \sum_{J=1}^{n} \phi^J(\boldsymbol{x}^I) \hat{s}^{hJ} \quad \text{for} \quad I = 1...n. \tag{2.77}$$

The equation above can be reorganized in a matrix-vector multiplication:

$$\Phi \hat{\boldsymbol{s}}^h = \boldsymbol{s}^h, \tag{2.78}$$

where

$$\Phi = \begin{bmatrix} \phi^1(\boldsymbol{x^1}) & \dots & \phi^n(\boldsymbol{x^1}) \\ \vdots & \ddots & \vdots \\ \phi^1(\boldsymbol{x^n}) & \dots & \phi^n(\boldsymbol{x^n}) \end{bmatrix}, \quad \hat{\boldsymbol{s}}^h = \begin{bmatrix} \hat{s}^{h1} \\ \vdots \\ \hat{s}^{hn} \end{bmatrix}, \quad \text{and} \quad \boldsymbol{s}^h = \begin{bmatrix} s^{h1} \\ \vdots \\ s^{hn} \end{bmatrix}. \tag{2.79}$$

The virtual nodal values of the scalar function are then

$$\hat{\boldsymbol{s}}_{ij}^{h} = R\boldsymbol{s}_{ij}^{h}, \quad \text{with} \quad R = \Phi^{-1}. \tag{2.80}$$

The approximated scalar value at coordinate $\boldsymbol{x}$ then equals

$$s^{h}(\boldsymbol{x}) = \sum_{J=1}^{n}\sum_{K=1}^{n} \phi^{J}(\boldsymbol{x}) R^{JK} s_{ij}^{hK} = \sum_{K=1}^{n} \psi^{K}(\boldsymbol{x}) s_{ij}^{hK}, \tag{2.81}$$

in which

$$\psi^{K}(\boldsymbol{x}) = \sum_{J=1}^{n} \phi^{J}(\boldsymbol{x}) R^{JK}. \tag{2.82}$$

With the approximation expressed in the nodal values, the local weak form from Eq. 2.75 can be discretized as

$$\sum_{K=1}^{n} \{\boldsymbol{B}^{IK}\}^{\mathrm{T}} \boldsymbol{\sigma}^{hK} + \boldsymbol{b}(\boldsymbol{x}^{I}) = 0, \tag{2.83}$$

where

$$\boldsymbol{B}^{IK} = \begin{bmatrix} \psi_{,1}^{K}(\boldsymbol{x}^{I}) & 0 \\ 0 & \psi_{,2}^{K}(\boldsymbol{x}^{I}) \\ \psi_{,2}^{K}(\boldsymbol{x}^{I}) & \psi_{,1}^{K}(\boldsymbol{x}^{I}) \end{bmatrix} \quad \text{and} \quad \boldsymbol{\sigma}^{hK} = \begin{bmatrix} \sigma_{11}^{hK} \\ \sigma_{22}^{hK} \\ \sigma_{12}^{hK} \end{bmatrix} = \begin{bmatrix} \sigma_{11}^{h}(\boldsymbol{x}^{K}) \\ \sigma_{22}^{h}(\boldsymbol{x}^{K}) \\ \sigma_{12}^{h}(\boldsymbol{x}^{K}) \end{bmatrix}. \tag{2.84}$$

Because $I = 1...n$, Eq. 2.83 gives $2n$ independent equations with $3n$ unknowns. Since there are not enough equations to solve the problem, the stress is expressed in the displacement using the constitutive equations from Eq. 2.46. The stress vector at coordinate $\boldsymbol{x}^{K}$ can be written as

$$\boldsymbol{\sigma}^{hK} = \sum_{J=1}^{n} \boldsymbol{D}\boldsymbol{B}^{KJ}\boldsymbol{u}^{hJ}. \tag{2.85}$$

The displacement is approximated with the MLS approximation expressed in the actual nodal values (Eq. 2.81). Using this equation, the local discretized linear elasticity equations can be rewritten as

$$\sum_{J=1}^{n}\sum_{K=1}^{n} \{\boldsymbol{B}^{IK}\}^{\mathrm{T}} \boldsymbol{D}\boldsymbol{B}^{KJ}\boldsymbol{u}^{hJ} = \sum_{J=1}^{n} \boldsymbol{K}^{IJ}\boldsymbol{u}^{hJ} = -\boldsymbol{b}(\boldsymbol{x}^{I}), \tag{2.86}$$

with

$$\boldsymbol{K}^{IJ} = \sum_{K=1}^{n} \{\boldsymbol{B}^{IK}\}^{\mathrm{T}} \boldsymbol{D}\boldsymbol{B}^{KJ}. \tag{2.87}$$

All terms of the linear elasticity equations can be organized in the global stiffness matrix K. The final linear equations that have to be solved are

$$\boldsymbol{K}\boldsymbol{U}^h = \boldsymbol{F}, \tag{2.88}$$

in which

$$\boldsymbol{K} = \begin{bmatrix} \boldsymbol{K}^{11} & \dots & \boldsymbol{K}^{1n} \\ \vdots & \ddots & \vdots \\ \boldsymbol{K}^{n1} & \dots & \boldsymbol{K}^{nn} \end{bmatrix}, \quad \boldsymbol{U}^h = \begin{bmatrix} \boldsymbol{u}^{h1} \\ \vdots \\ \boldsymbol{u}^{hn} \end{bmatrix}, \quad \text{and} \quad \boldsymbol{F} = \begin{bmatrix} -\boldsymbol{b}(\boldsymbol{x}^1) \\ \vdots \\ -\boldsymbol{b}(\boldsymbol{x}^n) \end{bmatrix}. \tag{2.89}$$

The equations above can be simplified by separating the stiffness matrix in two parts:

$$\boldsymbol{K} = \boldsymbol{K}_{\boldsymbol{s}}\boldsymbol{T}. \tag{2.90}$$

This leads to the following two relations:

$$\boldsymbol{K}_s\boldsymbol{\sigma}^h = \boldsymbol{F} \tag{2.91}$$

and

$$\boldsymbol{\sigma}^h = \boldsymbol{T}\boldsymbol{U}^h, \tag{2.92}$$

with

$$\boldsymbol{\sigma}^h = \begin{bmatrix} \boldsymbol{\sigma}^{h1} \\ \vdots \\ \boldsymbol{\sigma}^{hn} \end{bmatrix}, \quad \boldsymbol{K}_s = \begin{bmatrix} \{\boldsymbol{B}^{11}\}^{\mathrm{T}} & \dots & \{\boldsymbol{B}^{1n}\}^{\mathrm{T}} \\ \vdots & \ddots & \vdots \\ \{\boldsymbol{B}^{n1}\}^{\mathrm{T}} & \dots & \{\boldsymbol{B}^{nn}\}^{\mathrm{T}} \end{bmatrix} \quad \text{and}$$

$$\boldsymbol{T} = \begin{bmatrix} \boldsymbol{D}\boldsymbol{B}^{11} & \dots & \boldsymbol{D}\boldsymbol{B}^{1n} \\ \vdots & \ddots & \vdots \\ \boldsymbol{D}\boldsymbol{B}^{n1} & \dots & \boldsymbol{D}\boldsymbol{B}^{nn} \end{bmatrix}. \tag{2.93}$$

Enforcement of traction boundary conditions

The traction boundary conditions are enforced at each node that lies on the traction boundary. At these nodes the following boundary conditions should hold:

$$\boldsymbol{n}^K \boldsymbol{\sigma}^{hK} = \bar{\boldsymbol{t}}^K \quad \text{for} \quad K = 1...k_t, \tag{2.94}$$

in which k_t are the number of nodes on the traction boundary and

$$\boldsymbol{\sigma}^{hK} = \begin{bmatrix} \sigma_{11}^{hK} \\ \sigma_{22}^{hK} \\ \sigma_{12}^{hK} \end{bmatrix}, \quad \boldsymbol{n}^K = \begin{bmatrix} n_1^K & 0 & n_2^K \\ 0 & n_2^K & n_1^K \end{bmatrix} \quad \text{and} \quad \bar{\boldsymbol{t}}^K = \begin{bmatrix} \bar{t}_1^K \\ \bar{t}_2^K \end{bmatrix}. \tag{2.95}$$

A penalty approach is used, such that Eq. 2.88 satisfies the traction boundary conditions [23], [39]. First, the stress vectors $\boldsymbol{\sigma}^{hK}$ for each node on the traction boundary are combined in one vector $\boldsymbol{\sigma}_1$:

$$\boldsymbol{\sigma}_1 = \begin{bmatrix} \sigma^{h1} \\ \vdots \\ \sigma^{hk_t} \end{bmatrix}. \tag{2.96}$$

The stress vectors for the other nodes, not lying on the traction boundary, are combined in a different vector $\boldsymbol{\sigma}_2$. With the combined stress vector $\boldsymbol{\sigma}_1$, the traction boundary conditions can be combined in a set of equations, according to

$$\boldsymbol{n}_t \boldsymbol{\sigma}_1 = \bar{\boldsymbol{t}}_t, \tag{2.97}$$

in which

$$\boldsymbol{n}_t = \begin{bmatrix} \boldsymbol{n}^1 & & 0 \\ & \ddots & \\ 0 & & \boldsymbol{n}^{k_t} \end{bmatrix} \quad \text{and} \quad \bar{\boldsymbol{t}}_t = \begin{bmatrix} \bar{\boldsymbol{t}}^1 \\ \vdots \\ \bar{\boldsymbol{t}}^{k_t} \end{bmatrix}. \tag{2.98}$$

Next, with the vectors $\boldsymbol{\sigma}_1$ and $\boldsymbol{\sigma}_2$, Eq. 2.91 can be separated according to

$$\boldsymbol{K}_s^1 \boldsymbol{\sigma}_1 + \boldsymbol{K}_s^2 \boldsymbol{\sigma}_2 = \boldsymbol{F}, \tag{2.99}$$

in which $\boldsymbol{K}_s^1$ and $\boldsymbol{K}_s^2$ are parts of $\boldsymbol{K}_s$ belonging to $\boldsymbol{\sigma}_1$ and $\boldsymbol{\sigma}_2$, respectively. Furthermore, Eq. 2.92 can be separated in a similar manner, resulting in

$$\boldsymbol{\sigma}_1 = \boldsymbol{T}_1 \boldsymbol{U}^h \tag{2.100}$$

and

$$\boldsymbol{\sigma}_2 = \boldsymbol{T}_2 \boldsymbol{U}^h, \tag{2.101}$$

in which $\boldsymbol{T}^1$ and $\boldsymbol{T}^2$ are parts of $\boldsymbol{T}$ belonging to $\boldsymbol{\sigma}_1$ and $\boldsymbol{\sigma}_2$, respectively. In order to enforce the traction boundary conditions, Eq. 2.97 is first multiplied with a penalty $\alpha \boldsymbol{n}_t^{\mathrm{T}}$, and then added to Eq. 2.100:

$$\boldsymbol{\sigma}_1 + \alpha \boldsymbol{n}_t^{\mathrm{T}} \boldsymbol{n}_t \boldsymbol{\sigma}_1 = \boldsymbol{T}_1 \boldsymbol{U}^h + \alpha \boldsymbol{n}_t^{\mathrm{T}} \bar{\boldsymbol{t}}_t. \tag{2.102}$$

This equation can be rewritten in

$$\begin{aligned} \boldsymbol{\sigma}_1 &= \{\boldsymbol{I} + \alpha \boldsymbol{n}_t^{\mathrm{T}} \boldsymbol{n}_t\}^{-1} \{\boldsymbol{T}_1 \boldsymbol{U}^h + \alpha \boldsymbol{n}_t^{\mathrm{T}} \bar{\boldsymbol{t}}_t\} \\ &= \boldsymbol{Q} \{\boldsymbol{T}_1 \boldsymbol{U}^h + \alpha \boldsymbol{n}_t^{\mathrm{T}} \bar{\boldsymbol{t}}_t\} \\ &= \boldsymbol{Q} \boldsymbol{T}_1 \boldsymbol{U}^h + \alpha \boldsymbol{Q} \boldsymbol{n}_t^{\mathrm{T}} \bar{\boldsymbol{t}}_t, \end{aligned} \tag{2.103}$$

with $\boldsymbol{I}$ a unit matrix and

$$\boldsymbol{Q} = \{\boldsymbol{I} + \alpha \boldsymbol{n}_t^{\mathrm{T}} \boldsymbol{n}_t\}^{-1}. \tag{2.104}$$

Finally, Eq. 2.101 and Eq. 2.103 are substituted in Eq. 2.99, resulting in

$$\{\boldsymbol{K}_s^1 \boldsymbol{Q} \boldsymbol{T}_1 + \boldsymbol{K}_s^2 \boldsymbol{T}_2\} \boldsymbol{U}^h = \boldsymbol{F} - \alpha \boldsymbol{Q} \boldsymbol{n}_t^{\mathrm{T}} \bar{\boldsymbol{t}}_t. \tag{2.105}$$

This equation can be rewritten in the well-known form

$$\boldsymbol{K}_t \boldsymbol{U}^h = \boldsymbol{F}_t, \tag{2.106}$$

with

$$\boldsymbol{K}_t = \boldsymbol{K}_s^1 \boldsymbol{Q} \boldsymbol{T}_1 + \boldsymbol{K}_s^2 \boldsymbol{T}_2 \quad \text{and} \quad \boldsymbol{F}_t = \boldsymbol{F} - \alpha \boldsymbol{Q} \boldsymbol{n}_t^{\mathrm{T}} \bar{\boldsymbol{t}}_t. \tag{2.107}$$

Enforcement of displacement boundary conditions

Since the discretized linear elasticity equations are expressed in the nodal displacement values, the essential boundary conditions can be applied similarly to FEM. Eq. 2.88 can be separated in two parts, a known part and an unknown part, according to

$$\begin{bmatrix} \boldsymbol{K_a} & \boldsymbol{K_b} \\ \boldsymbol{K_c} & \boldsymbol{K_d} \end{bmatrix} \begin{bmatrix} \boldsymbol{U}_a^h \\ \boldsymbol{U}_b \end{bmatrix} = \begin{bmatrix} \boldsymbol{F}_a \\ \boldsymbol{F}_b \end{bmatrix}, \tag{2.108}$$

where $\boldsymbol{U}_a^h$ is the unknown displacement and $\boldsymbol{U}_b^h$ is the known displacement at the displacement boundary. The displacements on the boundary can then be imposed

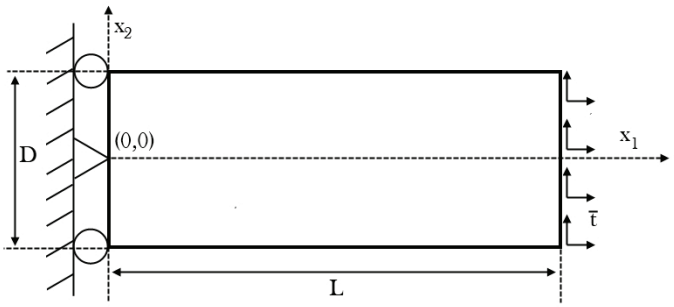

Figure 2.11: Two-dimensional cantilever beam problem with height D and length L. The beam is subjected to a displacement boundary condition on the left side and a traction boundary condition on the right side.

according to

$$\boldsymbol{K_a U}_a^h = \boldsymbol{F}_a - \boldsymbol{K_b U}_b^h. \tag{2.109}$$

When also dealing with traction boundary conditions, Eq. 2.88 should be replaced with Eq. 2.106. Then, $\boldsymbol{K}$ and $\boldsymbol{F}$ are replaced by $\boldsymbol{K}_t$ and $\boldsymbol{F}_t$, respectively.

2.3 Exemplary problem

In Sec. 2.2 two meshless methods have been discussed, namely the EFG method and the MLPG mixed collocation method. They were applied to discretize the linear elasticity problem. In this section the two meshless methods are compared by applying them to the relatively simple exemplary problem of a two-dimensional cantilever beam. Furthermore, a convergence study is performed on parameters that influence the accuracy.

2.3.1 Two-dimensional cantilever beam

The two-dimensional cantilever beam problem (hereafter: cantilever beam) is deployed to test the EFG and the MLPG mixed collocation method on the accuracy of their solutions. A cantilever beam is subjected to a transverse load at the right end, and fixed to the wall at the left end, as shown in Fig. 2.11. Here, D is the height and L is the length of the beam. The transverse load at the right end of the beam is a downward parabolic traction, defined by

$$\bar{t} = \begin{bmatrix} 0 \\ -\frac{P}{2I}\left[\frac{D^2}{4} - y^2\right] \end{bmatrix}, \quad \text{with} \quad I = \frac{D^3}{12}, \tag{2.110}$$

where P is the maximum value of the traction on the right end, and I is the moment of inertia of the beam. Assuming plane stress conditions, the exact solution for the displacement and stress in the beam can be determined analytically [39], [12]:

$$u_1^a(\boldsymbol{x}) = \frac{Px_2}{6EI}\left[\{6L - 3x_1\}x_1 + \{2+\nu\}\{x_2^2 - \frac{D^2}{4}\}\right] \tag{2.111}$$

$$u_2^a(\boldsymbol{x}) = -\frac{P}{6EI}\left[3\nu x_2^2\{L - x_1\} + \{4+5\nu\}\frac{D^2 x_1}{4} + \{3L - x_1\}x_1^2\right]. \tag{2.112}$$

Here, $u_1^a(\boldsymbol{x})$ and $u_2^a(\boldsymbol{x})$ respectively are the displacements in the x_1 and x_2 direction. The analytical solution for the stress in the beam equals

$$\sigma_{11}^a(\boldsymbol{x}) = \frac{P[L - x_1]x_2}{I} \tag{2.113}$$

$$\sigma_{21}^a(\boldsymbol{x}) = 0 \tag{2.114}$$

$$\sigma_{12}^a(\boldsymbol{x}) = -\frac{P}{2I}\left[\frac{D^2}{4} - x_2^2\right], \tag{2.115}$$

in which E is the Young's modulus, ν is the Poisson's ratio and the superscript a signifies an analytical value. Further investigation of this exemplary problem with meshless methods is done with the following model constants: $D = 12$, $L = 48$, $P = 0.1$, $E = 1$ and $\nu = 0.3$. The essential boundary conditions are prescribed according to the analytical solution at the left boundary of the cantilever beam $u_1(x_1 = 0, -1/2D \leq x_2 \leq 1/2D)$ and $u_2(x_1 = 0, -1/2D \leq x_2 \leq 1/2D)$.[5]

2.3.2 EFG and MLPG mixed collocation solutions

To solve the cantilever beam problem, the problem domain Ω is discretized using both the EFG and MLPG mixed collocation method. The stress and strain are obtained using a regular nodal distribution, as shown in Fig. 2.12. The integration cells and integration points are only used in the EFG method. Tab. 2.1 gives parameters, and their value, which are used in the EFG and MLPG mixed collocation method.

The displacement and stress are first obtained with the EFG method (Eq. 2.73). The solution for the displacement $u_1^h(\boldsymbol{x})$ and $u_2^h(\boldsymbol{x})$ is shown in Fig. 2.13a and Fig. 2.13b. The approximation of the stress can then be obtained from the approximated displacement according to Eq. 2.64, and is shown in Fig. 2.13c, Fig. 2.13d

[5] Since meshless methods cannot deal with point loads correctly, the essential boundary condition is prescribed on the left edge of the beam.

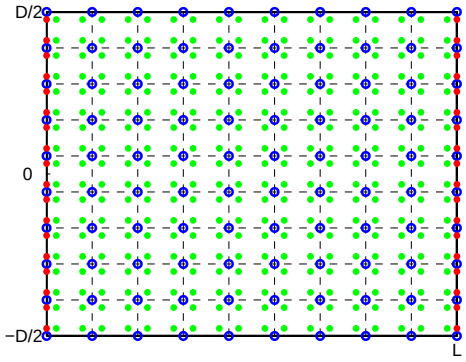

Figure 2.12: Discretization of the domain and boundary of the cantilever beam. The discretized domain consists of nodes (blue circles) and integration cells (black dashed lines). These integration cells contain integration points (green dots). Moreover, the red dots denote the boundary integration points.

Table 2.1: EFG and MLPG mixed collocation method parameters.

	EFG	MLPG
Nodes in x_1 direction	$n_1 = 10$	$n_1 = 10$
Nodes in x_2 direction	$n_2 = 10$	$n_2 = 10$
Influence domain shape	rectangular	rectangular
Average nodal distance in x_1 direction	$d_1 = L/[n_1 - 1]$	$d_1 = L/[n_1 - 1]$
Average nodal distance in x_2 direction	$d_2 = D/[n_2 - 1]$	$d_2 = D/[n_2 - 1]$
Local influence domain size	$d = 2.5$	$d = 1.15$
Size of monomial basis	2 (linear)	2 (linear)
Integration cells in x_1 direction	$m_1 = 9$	n/a
Integration cells in x_2 direction	$m_2 = 9$	n/a
Integration points per cell	$n_g = 4$	n/a

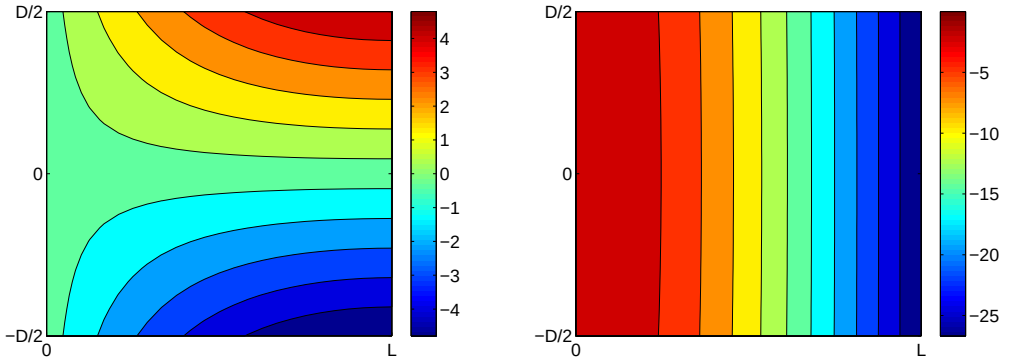

(a) $u_1^h(\boldsymbol{x})$

(b) $u_2^h(\boldsymbol{x})$

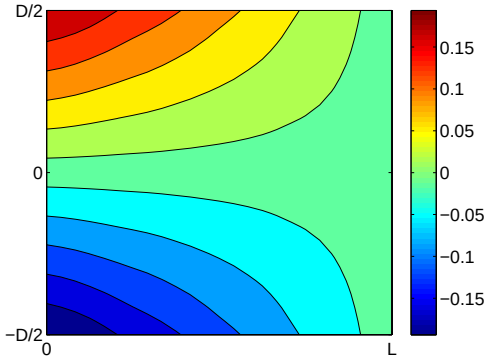

(c) $\sigma_{11}^h(\boldsymbol{x})$

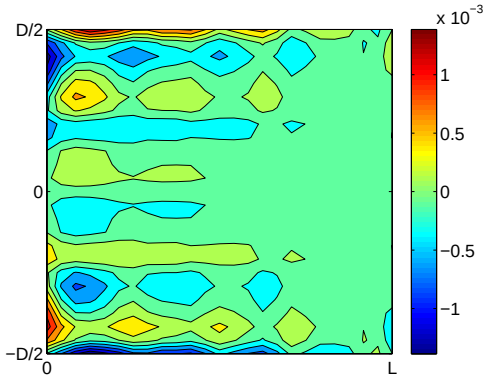

(d) $\sigma_{22}^h(\boldsymbol{x})$

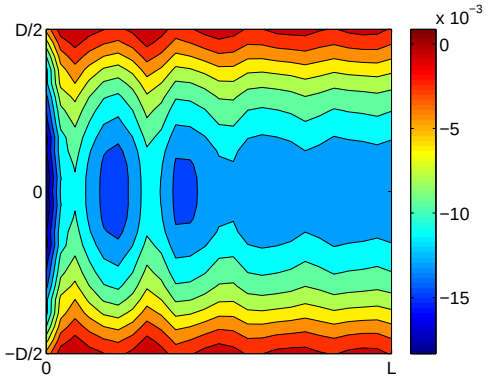

(e) $\sigma_{12}^h(\boldsymbol{x})$

Figure 2.13: Displacement and stress in the cantilever beam for a regular nodal distribution, found with the EFG method.

and Fig. 2.13e. The solution found with the EFG method corresponds well to the analytical solution, although some light numerical oscillations are present in the approximation of $\sigma_{22}^h(\boldsymbol{x})$ and $\sigma_{12}^h(\boldsymbol{x})$.

The displacement and stress are also approximated with the MLPG mixed collocation method (2.109). The displacements $u_1^h(\boldsymbol{x})$ and $u_2^h(\boldsymbol{x})$ are shown in Fig. 2.14a and Fig. 2.14b. The stress can be derived from the approximated displacement according to Eq. 2.92. $\sigma_{11}^h(\boldsymbol{x})$, $\sigma_{22}^h(\boldsymbol{x})$ and $\sigma_{12}^h(\boldsymbol{x})$ are shown respectively in Fig. 2.14c, Fig. 2.14d and Fig. 2.14e. Similar results as for the EFG method are obtained, although the oscillations in the stress are reduced.

The error norm can assist in a qualitative comparison between both meshless methods. The error norm is a scalar quantity and is determined by calculating the relative error between the elastic energy of the approximated solution and analytical solution. It is given by

$$||E|| = \frac{\left[\int_\Omega \frac{1}{2}\{\boldsymbol{\epsilon}^h(\boldsymbol{x}) - \boldsymbol{\epsilon}^a(\boldsymbol{x})\}^{\mathrm{T}}\{\boldsymbol{\sigma}^h(\boldsymbol{x}) - \boldsymbol{\sigma}^a(\boldsymbol{x})\}d\Omega\right]^{1/2}}{\left[\int_\Omega \frac{1}{2}\{\boldsymbol{\epsilon}^a(\boldsymbol{x})\}^{\mathrm{T}}\{\boldsymbol{\sigma}^a(\boldsymbol{x})\}d\Omega\right]^{1/2}}, \tag{2.116}$$

where a value of 0 corresponds to a perfect fit and a value of one corresponds to an error of 100 %.[6] For the EFG method, the error norm equals $||E|| = 0.0164$ or 1.64%. The error norm in the MLPG mixed collocation method is $||E|| = 0.0483$ or a 4.83% error in the energy. Thus, for the parameter values in Tab. 2.1, the error norm in the MLPG mixed collocation method is a factor three higher. However, a different choice in parameter values might influence the accuracy. This will be investigated next.

2.3.3 Influence of discretization parameters

In this section the convergence of the EFG and MLPG mixed collocation solution is investigated, by varying the values of the parameters used in the discretizations. In the EFG and MLPG mixed collocation method, the following parameters can be altered: the nodal position, the number of nodes, the nodal influence domain and the monomial basis. Furthermore, the precision of the numerical integration can be changed in the EFG method. The convergence of the accuracy of the approximated solution is defined by the error norm according to Eq. 2.116.

First, the influence of the number of nodes is considered. The number of nodes

[6] In the EFG method the integral in this equation is evaluated with the existing background mesh. Since no background mesh is present in the MLPG mixed collocation method, integration is done by nodal integration. In nodal integration, each node represents part of the volume and the integral can then be replaced by a summation $\int s(\boldsymbol{x})d\Omega = \sum_{I=1}^{n} s(\boldsymbol{x}^I)dV$.

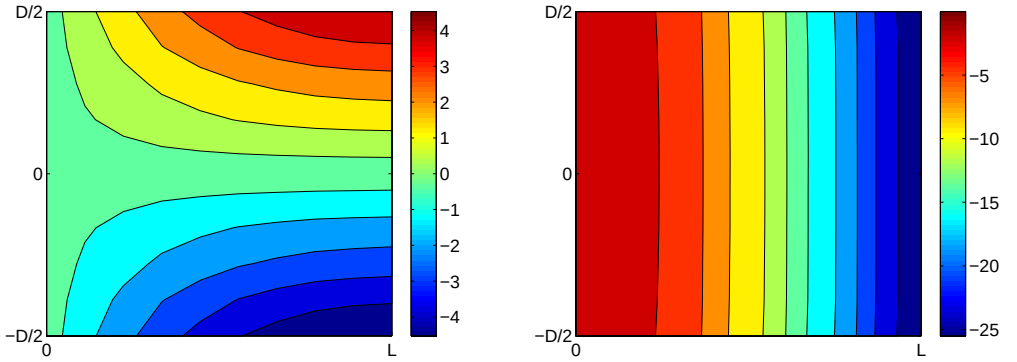

(a) $u_1^h(\boldsymbol{x})$

(b) $u_2^h(\boldsymbol{x})$

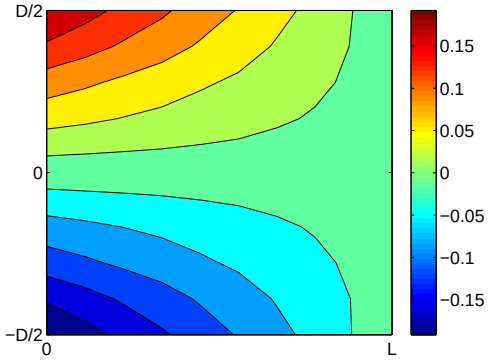

(c) $\sigma_{11}^h(\boldsymbol{x})$

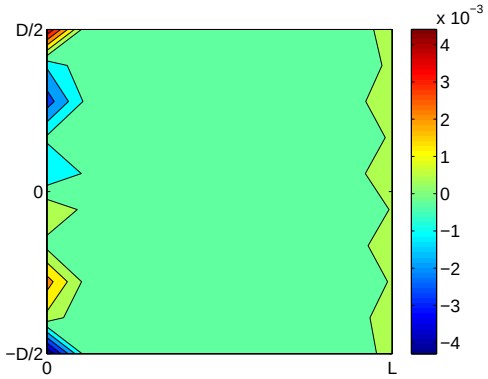

(d) $\sigma_{22}^h(\boldsymbol{x})$

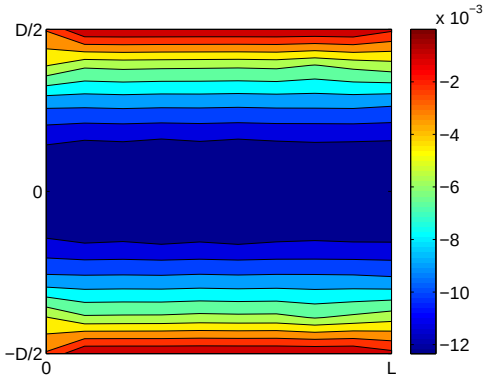

(e) $\sigma_{12}^h(\boldsymbol{x})$

Figure 2.14: Displacement and stress in the cantilever beam for a regular nodal distribution, found with the MLPG mixed collocation method.

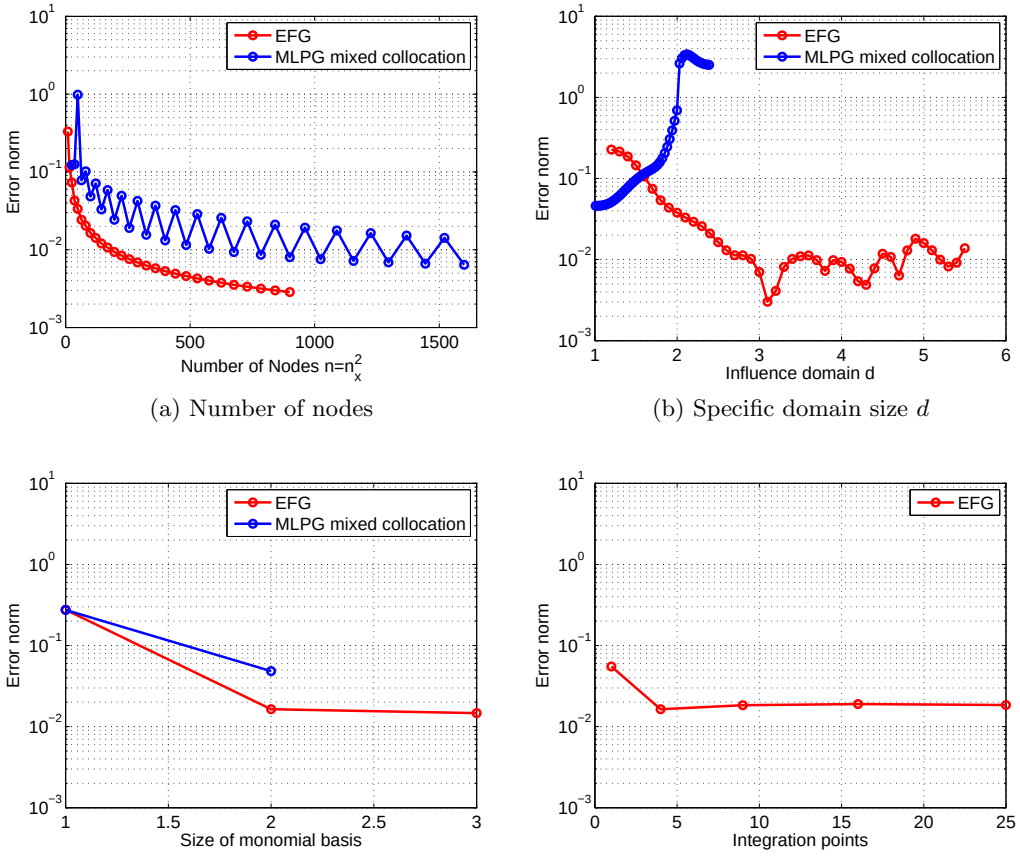

(a) Number of nodes

(b) Specific domain size d

(c) Order of monomial basis

(d) Integration points

Figure 2.15: Convergence study on the accuracy of the EFG and MLPG mixed collocation method. The error norm is calculated for a varying number of nodes, specific domain size d, order of the monomial basis and number of integration points.

n_1 in the x_1 direction is equal to the number of nodes n_2 in the x_2 direction. The convergence of the solution with respect to the number of nodes is shown in Fig. 2.15a. For an increasing number of nodes, the fault in the approximated solution decreases for both the EFG and the MLPG mixed collocation method. The EFG method shows the best convergence for all number of nodes. For instance, the error norm for a discretization with 250 nodes is 5 times lower for the EFG method. Even for a discretization with only a few nodes, the EFG method shows good results. Moreover, an even or uneven number of nodes has a large effect on the accuracy of the MLPG mixed collocation method.

Second, the convergence study with respect on the nodal influence domain is performed. The simplest approach for altering the influence domains is to vary its size, which can be achieved by varying the nodal influence domain size d. In Fig. 2.15b the effect of the size on the error norm is shown. Both meshless methods show different behavior. For low values of d, the MLPG mixed collocation method shows the best convergence. However, this method quickly becomes less accurate when increasing the domain size. In contrast, the EFG method shows an improvement in convergence for a larger domain size. Overall, the EFG method is more accurate than the MLPG mixed collocation method.

Third, the error norm is determined for different orders of the monomial basis. Orders one until three are considered, where an order of one corresponds to a constant basis, two to a linear basis and three to a quadratic basis. The convergence results are shown in Fig. 2.15c. Note that a quadratic basis in the MLPG mixed collocation method results in a singular system. This is caused by the small nodal influence domain. For the EFG and MLPG mixed collocation method, the error norm of the constant basis is much higher than the convergence of the other bases (almost ten times). Furthermore, the difference between the linear and quadratic basis in the EFG method is small.

Last, the error norm is calculated for the EFG method with a different number of integration points. The number of integration points in each cell is chosen to be equal to 4, 9, 16 and 25. The error norm is given in Fig. 2.15d. This figure clarifies that the number of integration points does not greatly influence the convergence of the solution. However, for a more complicated problem the convergence might be more dependent on the number of integration points.

So far, a regular nodal distribution has been used in the discretization. However, an unlimited number of irregular nodal distributions can be constructed. A complete chapter (Chap. 3) focusses on the effect of the nodal distribution on accuracy and material distribution. For this reason, the effect of the nodal

distribution on the accuracy will not be investigated in this section.

2.4 Characteristics of meshless methods for the MNA

In this chapter, the EFG and MLPG mixed collocation methods have been discussed and applied to the cantilever beam problem. More insight in the characteristics of both methods has been gained by a convergence study. Since the meshless methods will be used for the discretization in the Moving Node Approach in topology optimization, these characteristics are essential and discussed in this section. The favorable characteristics are derived from the EFG and MLPG mixed collocation method.

In general, the EFG method is more precise than the MLPG mixed collocation method. However, the MLPG mixed collocation method shows optimal performance for small nodal influence domains. This reduces the computational costs of this method. In contrast, larger nodal influence domains result in more accurate solutions in the EFG method.

Although this characteristic causes higher computational costs, it also provides for higher flexibility in the nodal distribution. I.e. the nodes can be moved more freely through the problem domain, without creating holes. Thus, in the EFG method the nodal distribution does not have to be regular. In contrast, the nodal distribution in the MLPG mixed collocation is not flexible. Since the nodal influence domains are small, perturbations in the position of the nodes result in gaps in the problem domain.

The MNA is based on the redistribution of mass containing nodes. This nodal movement requires flexibility of the underlying meshless method. For this reason, the size of the nodal domain should not be too small.

Therefore, a requirement for the MNA should be:

The meshless method should be accurate for relatively large nodal influence domains.

Chapter 3

Effect of the nodal distribution in the EFG method

In order to find the optimal layout of the problem domain with the MNA in topology optimization, the nodes present in the underlying meshless method are redistributed. These changes in the nodal position will affect not only the layout of the problem domain, but also the accuracy of the solution to the physical problem. In this chapter the effect of the nodal distribution on the accuracy and on the material distribution will be investigated.

For the cantilever beam problem, discussed in Chap. 2, the EFG method showed the highest potential. This is mainly due to the accurate results for relatively large nodal influence domains. The large size of the domains allows in a flexible distribution of nodes. Therefore, the effect of the nodal distribution will be tested on the EFG method.

First, the effect of the nodal position on the accuracy will be investigated in Sec. 3.1. Random nodal distributions are considered in two exemplary linear elasticity problems and from these a global effect on the accuracy of the EFG method can be determined. Moreover, local effects of the nodal distribution determined in the underlying MLS approximation are investigated.

Second, in Sec. 3.2 the influence of the nodal distribution on the material layout will be examined. In principle, only material is present at coordinates in which the support domain contains nodes. By considering various problem domains, the relation between nodal distribution and material distribution can be established.

3.1 Effect of the nodal distributions on accuracy

In this section, the effect of the nodal distribution on the accuracy of approximations will be investigated. By comparing various nodal distributions, a more tangible understanding of the influence of the nodal position is attained. This exploration is performed for the EFG method in two steps. First, in Sec. 3.1.1 the global precision of the solution to two linear elastic exemplary problems is determined for various random nodal distributions. Second, the accuracy of the MLS approximation is investigated for locally changing nodal distributions in Sec. 3.1.2. All tests performed in this section have a homogeneous material distribution in common. So, only the effect of the nodal position on the precision of the discretization is considered in this section.

3.1.1 Global effect of nodal distribution

In this part, the global effect of randomly distributed nodes is determined. With the help of two scalar quantities, a tangible understanding of the sensitivity of the discretization to the nodal distribution can be expressed and compared.

The first scalar quantity is the error norm (Eq. 2.116), which has already been used in Sec. 2.3. It expresses the relative difference in elastic energy between the numerical and analytical solution. Since only exemplary problems are considered for which the analytical solution is known, the error norm can be determined.

The second scalar quantity is the compliance of the structure:

$$C = \boldsymbol{F}^{\mathrm{T}} \hat{\boldsymbol{U}}^{h}, \tag{3.1}$$

where C is the compliance, $\boldsymbol{F}$ is the vector containing the nodal force (Eq. 2.62) and $\hat{\boldsymbol{U}}^{h}$ is the approximated nodal displacement vector. There are two main reasons for using the compliance. First, the compliance can be interpreted as the inverse of the global stiffness of the structure. In FEM, larger mesh sizes often lead to stiffening. Similarly, in meshless methods the compliance can be used for understanding the effect of the nodal distributions. Second, particular topology optimization methods focus on the minimization of the compliance. By investigating the effect of the nodal distribution on the compliance, the effect of an optimization algorithm on the nodal movement can be determined.

The effect of the nodal distribution on the error norm (Eq. 2.116) and the compliance (Eq. 3.1) are discussed for two exemplary problems with similar domains: the uniaxial beam and the cantilever beam. The domain of these problems is shown in Fig. 4.6. The difference between these two problems is the traction

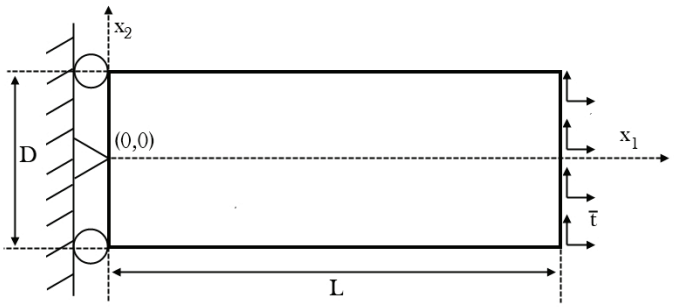

Figure 3.1: Problem domain and boundary conditions for the uniaxial and cantilever beam exemplary problems.

boundary condition. For the uniaxial beam, the traction vector $\bar{\boldsymbol{t}}$ equals

$$\bar{t} = \begin{bmatrix} P \\ 0 \end{bmatrix}. \tag{3.2}$$

The traction vector $\bar{\boldsymbol{t}}$ for the cantilever beam is

$$\bar{t} = \begin{bmatrix} 0 \\ -\frac{P}{2I}\left[\frac{D^2}{4} - y^2\right] \end{bmatrix} \quad \text{with} \quad I = \frac{D^3}{12}, \tag{3.3}$$

where P is the characteristic pressure. In Sec. 2.3 the analytical solution for the displacement and stress of the cantilever beam problem has already been given (Eq. 2.111 and Eq. 2.113). The analytical solution is also known for the uniaxial beam problem:

$$u_1^a(\boldsymbol{x}) = \frac{Px_1}{E} \quad \text{and} \quad u_2^a(\boldsymbol{x}) = -\frac{\nu P x_2}{E} \tag{3.4}$$

$$\sigma_{11}^a(\boldsymbol{x}) = P, \quad \sigma_{22}^a(\boldsymbol{x}) = 0 \quad \text{and} \quad \sigma_{12}^a(\boldsymbol{x}) = 0, \tag{3.5}$$

where $u_1^a(\boldsymbol{x})$ and $u_2^a(\boldsymbol{x})$ respectively are the analytical displacement in the x_1 and x_2 direction, E is the Young's modulus and ν is the Poisson's ratio.[1]

Further investigation of these two exemplary problem with meshless methods is done with the same model constants as in Sec. 2.3: $D = 12$, $L = 48$, $P = 0.1$, $E = 1$ and $\nu = 0.3$. The essential boundary conditions are prescribed according to the analytical solution at the left boundary of the cantilever beam $u_1(x_1 = 0, -1/2D \leq x_2 \leq 1/2D)$ and $u_2(x_1 = 0, -1/2D \leq x_2 \leq 1/2D)$.

[1]Note that the solution for the uniaxial loaded beam only contains constant terms for the stress and linear terms for the displacement, where the solution to the cantilever beam problem has quadratic terms for the stress and cubic terms for the displacement. Approximation of the stress and displacement in the uniaxial beam is easier than in the cantilever beam.

Table 3.1: Parameters used in the EFG method for the uniaxial and cantilever beam exemplary problems.

Nodes in x_1 direction	$n_1 = 10$
Nodes in x_2 direction	$n_2 = 10$
Influence domain shape	rectangular
Average nodal distance in x_1 direction	$d_1 = L/[n_1 - 1]$
Average nodal distance in x_2 direction	$d_2 = D/[n_2 - 1]$
Local influence domain size	$d = 2.5$
Size of monomial basis	2 (linear)
Integration cells in x_1 direction	$m_1 = 9$
Integration cells in x_2 direction	$m_2 = 9$
Integration points per cell	$n_g = 4$

Both exemplary problems are discretized with the EFG method according to the parameters in Tab. 3.1. Various nodal distributions are considered, generated in three manners: regular, random and semi-random nodal distributions.

The nodes in the regular nodal distribution are positioned on a rectangular grid. This distribution is shown in Fig. 3.2a and has been used in Sec. 2.3 to solve the cantilever beam problem.

The random distribution is created by randomly placing nodes inside the problem domain. An infinite number of random distributions is possible and a sample can be found in Fig. 3.2b. However, only nodal distributions for which the sum of the nodal influence domains cover the complete problem domain are considered. The results for the error norm and compliance will be represented by a probability distribution. By performing 5000 simulations of random nodal distribution, the shape of the probability distribution can be obtained [46].

The semi-random nodal distribution is a combination of the regular and random distribution. The nodes are first placed on a regular rectangular grid, but then randomly perturbed. The maximum size of the random perturbation equals $dr_{\mathrm{n}} d\boldsymbol{x}$, in which $d\boldsymbol{x}$ is the distance between nodes in the regular distribution. In this study, two semi-random distributions with $dr_{\mathrm{n}} = 0.1$ and $dr_{\mathrm{n}} = 1$ are considered. Of each, one sample is shown in Fig. 3.2c and Fig. 3.2d. 5000 samples of the semi-random nodal distributions are considered to find the probability distributions of the error norm and compliance.

Uniaxial beam problem

First, the displacement and stress in the uniaxial beam are determined for a regular nodal distribution. The results are shown in Fig. 3.3. The results for

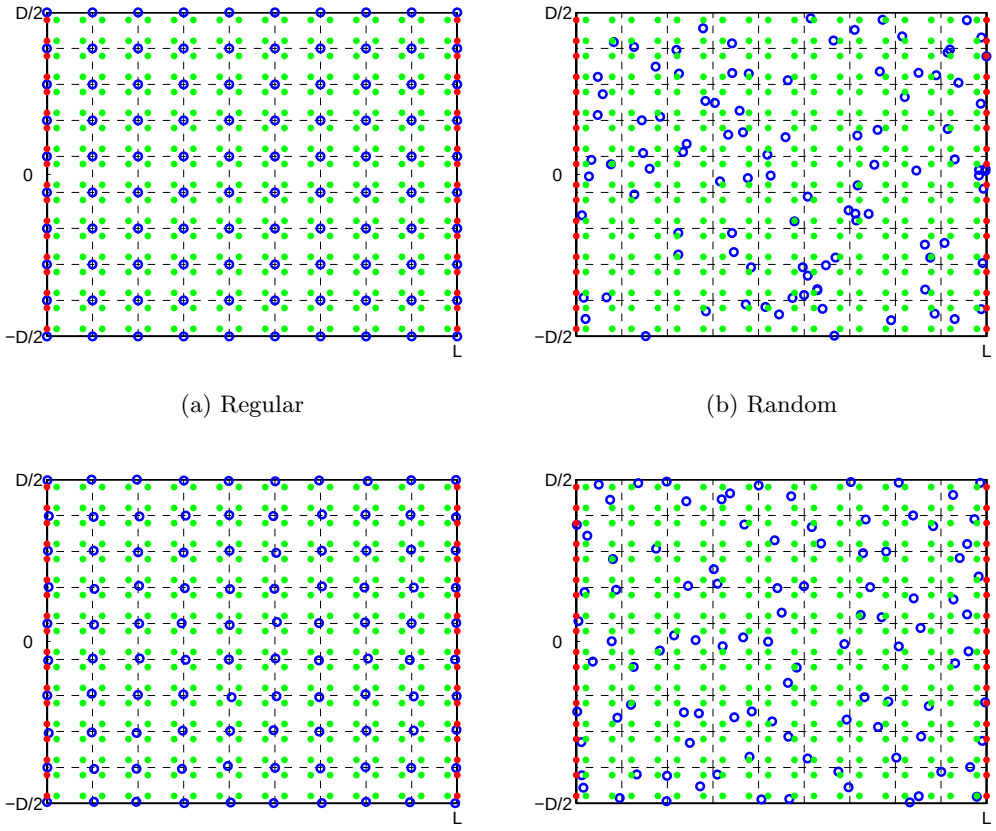

(a) Regular

(b) Random

(c) Semi-random $dr_{\mathrm{r}} = 0.1$

(d) Semi-random $dr_{\mathrm{r}} = 1$

Figure 3.2: Various nodal distributions for the discretization of the problem domain as shown in Fig. 4.6.

both the displacement and stress are in agreement with the analytical solution, which can be clearly seen in Fig. 3.3, and can also be derived from the error norm $||E|| = 7.3 \cdot 10^{-4} \approx 0.073\%$. Fig. 3.3c clarifies that the largest error occurs near the boundaries on which the traction and essential boundary conditions are applied. Moreover, an oscillation in the stress is observed in Fig. 3.3c and Fig. 3.3d. This oscillation is non-physical and therefore results from the discretization method.

Second, the probability distributions for the error norm and compliance of the random and semi-random nodal distributions are determined, and shown in Fig. 3.4.[2] For comparison, the error norm and compliance for the regular distribution are represented by the red dashed lines and the green line denotes the analytical compliance, which equals

$$C^a = \frac{P^2 L D}{E}. \tag{3.6}$$

Fig. 3.4a shows that a random distribution of nodes decreases the accuracy. Large values of the error norm are observed, with a mean (hereafter: M) of 0.056 and a standard deviation (hereafter: S) of 0.018. Similarly, a random nodal distribution decreases the accuracy of the approximated compliance. For the 5000 samples, the approximated compliance is always larger than the analytical compliance. From the error norm and compliance distributions (Fig. 3.4) it can be derived that it is unlikely to reach an error norm and compliance which are lower than in the regular distribution.

Similar results are obtained for the semi-random nodal distribution with $dr_\mathrm{n} = 1$ (Fig. 3.4b). However, the error norm is lower ($M = 0.028$ and $S = 0.0080$) and the compliance for the semi-random distribution with $dr_\mathrm{n} = 1$ shows a smaller deviation from the regular distribution and the analytical solution.

For the semi-random distribution with $dr_\mathrm{n} = 0.1$, a slightly different result is found, shown in Fig. 3.4c. Although the error norm for this nodal distribution ($M = 0.0033$ and $S = 7.7 \cdot 10^{-4}$) is still higher than for the regular distribution ($7.3 \cdot 10^{-4}$), for some samples the compliance is lower.

Cantilever beam problem

Previous analysis of the uniaxial beam problem is repeated on the cantilever beam problem. The approximated displacement and stress in the cantilever beam have already been shown in Sec. 2.3. The probability distributions for the error norm and compliance of the random and semi-random distributions and they are shown

[2] The displacement and stress for two random nodal distribution samples are shown in App. B in Fig. B.1.

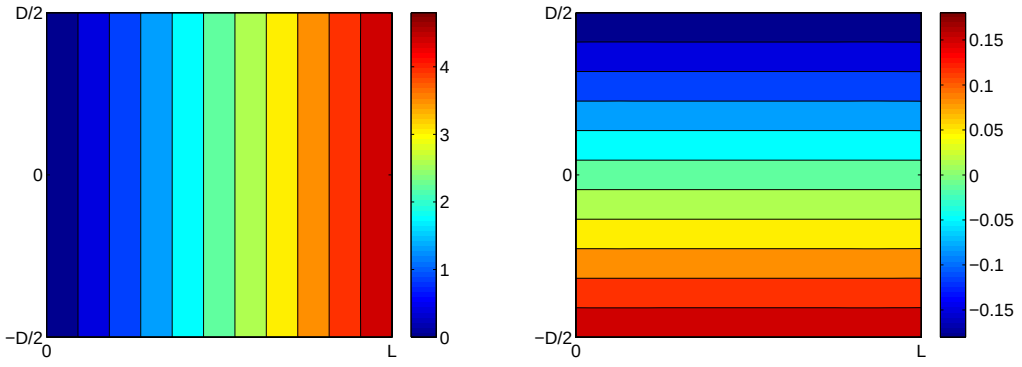

(a) Displacement u_1

(b) Displacement u_2

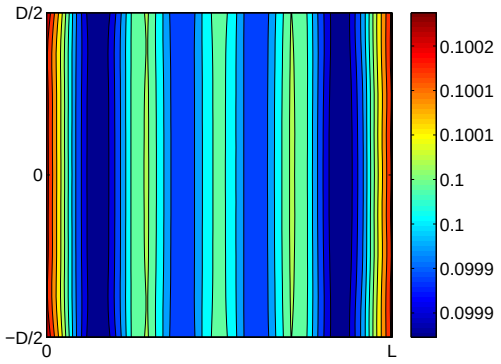

(c) Stress σ_{11}

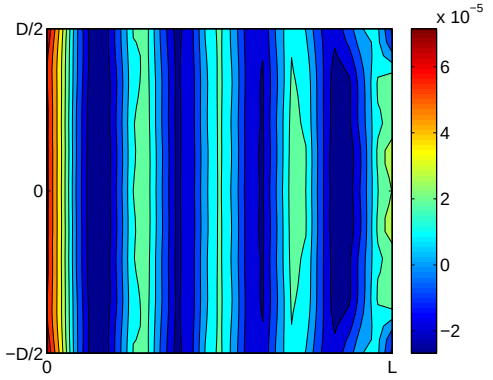

(d) Stress σ_{22}

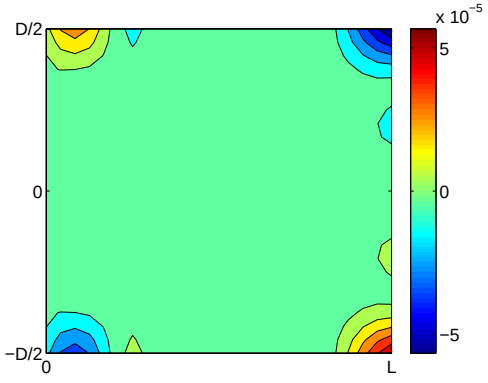

(e) Stress σ_{12}

Figure 3.3: Approximated displacement and stress for the uniaxial beam problem, found with the EFG method.

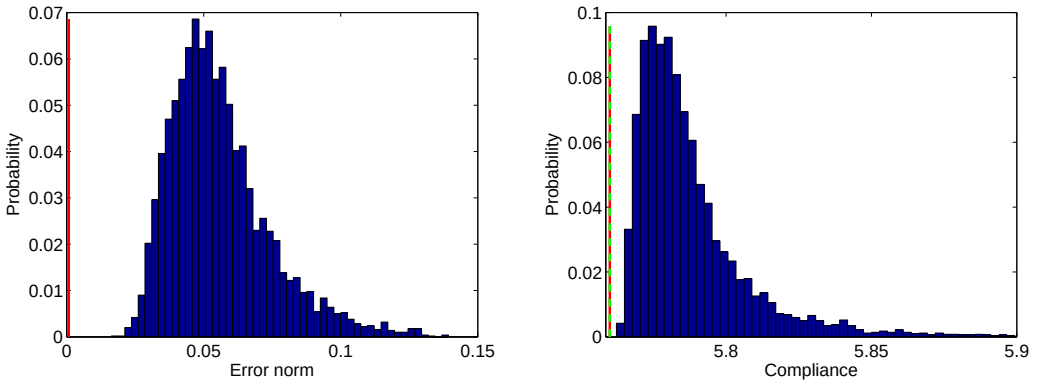

(a) Random

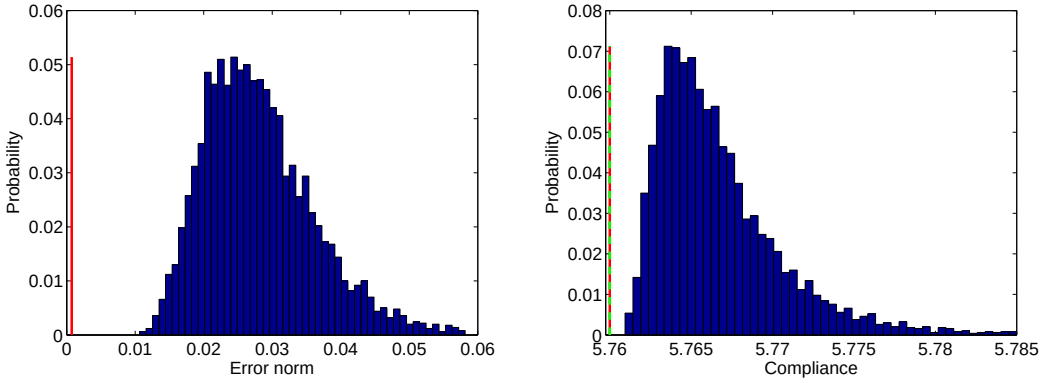

(b) Semi-random $dr_{\mathrm{n}} = 1$

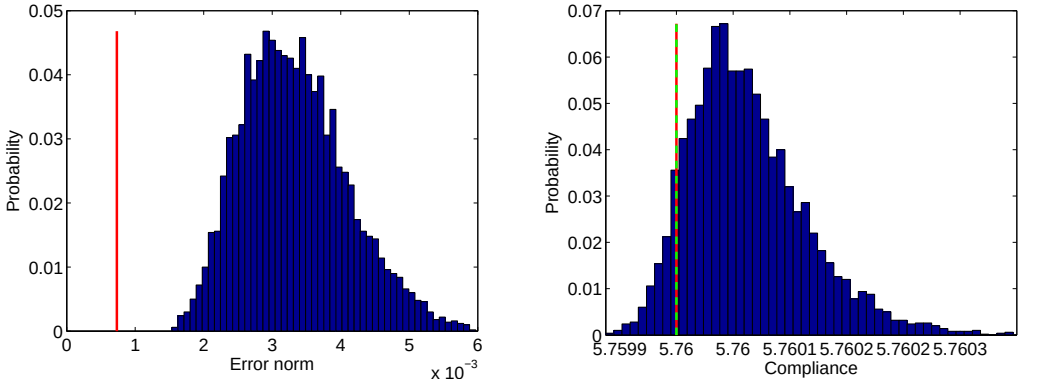

(c) Semi-random $dr_{\mathrm{n}} = 0.1$

Figure 3.4: Probability distributions for the error norm and compliance of the uniaxial beam problem, determined for various nodal distributions. The blue bars denote the results obtained with the random nodal distributions, the red line denotes the results found with the regular nodal distribution and the green dashed line gives the analytical value of the compliance.

in Fig. 3.5. Moreover, the compliance and error norm for the regular distribution and the compliance for the analytical solution are shown, in which the analytical compliance for the cantilever beam equals

$$C^a = \frac{D^3 P^2}{72EI^2}\{\frac{[4+5\nu]\, D^2 L}{4} + 2L^3\}. \tag{3.7}$$

In Fig. 3.5a the error norm and compliance distributions are given for the random nodal distribution.[3] A large error norm is found ($M = 0.53$ and $S = 0.076$). Similarly, the compliance greatly differs from the compliance obtained with the regular nodal distribution and the analytical compliance. For the 5000 samples, the approximated compliance is always lower than the analytical compliance. Thus, the beam stiffens for nodes that are randomly distributed.

Similar results are obtained for the semi-random distribution characterized by $dr_{\mathrm{n}} = 1$, shown in Fig. 3.5b. Compared to the random distribution, the error norm is halved ($M = 0.28$ and $S = 0.035$).

However, for the semi-random distribution with $dr_{\mathrm{n}} = 0.1$ (Fig. 3.5c) a difference arises in comparison to the previous two random distributions. Although the error norm ($M = 0.031$ and $S = 0.0041$) is always higher than for the regular distribution (0.0164), for some samples the compliance is higher. For these samples, the compliance corresponds better to the analytical compliance. However, since the error norm of the semi-random distribution is always higher than the error norm of the regular distribution, the increase in compliance is a numerical oscillation.

Comparison of the uniaxial and cantilever beam

For the uniaxial beam problem, Fig. 3.4 suggests that the error norm and compliance are related. This relation is confirmed by plotting the values of each sample of the error norm versus the compliance. This result in 5000 points, which are distributed along a curve, as shown in Fig. 3.6b. The curve shows that an increase in the error norm results in an increase in the compliance. This figure shows that the semi-random distributions are special cases of the random distribution, i.e. the samples for the random nodal distribution and the two semi-random nodal distributions are in different sections along the same curve.

Similarly, a relation between the error norm and compliance can be discovered for the cantilever beam problem. For each sample, the compliance is plotted versus the error norm, as shown in Fig. 3.6b. Clearly, these two scalar quantities are

[3] The displacement and stress for two random nodal distribution samples are shown in App. B in Fig. B.2.

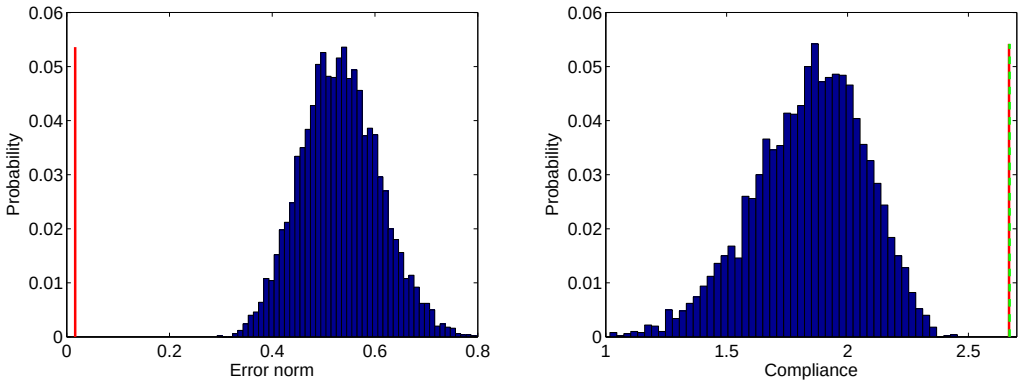

(a) Random

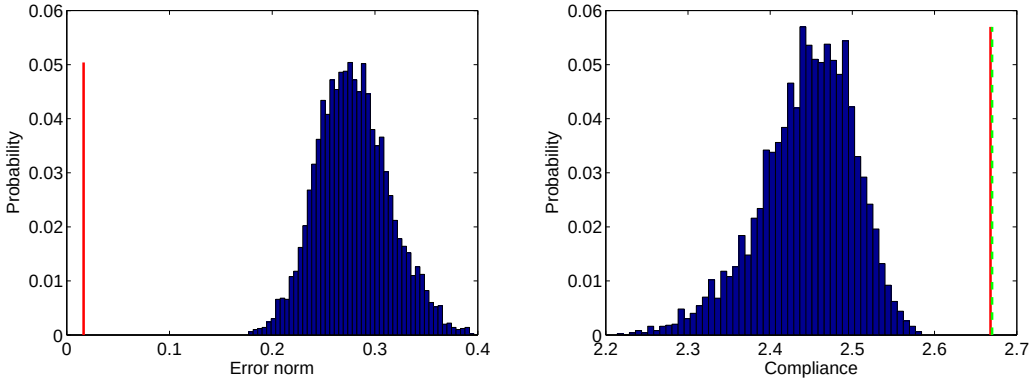

(b) Semi-random $dr_{\mathrm{n}} = 1$

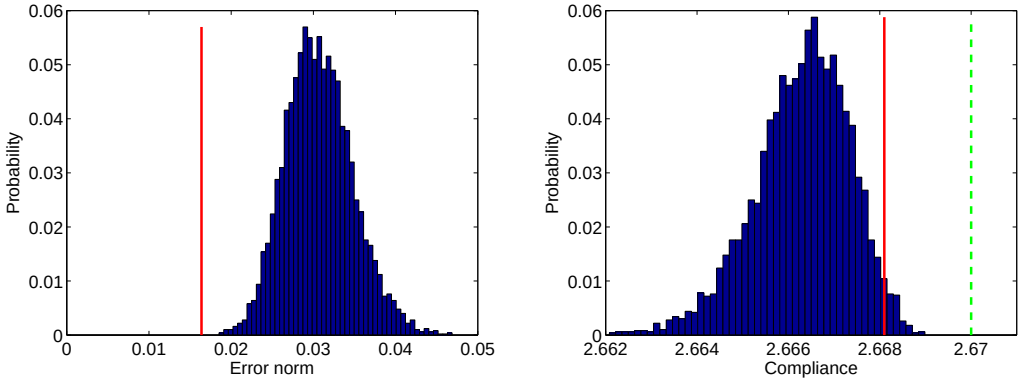

(c) Semi-random $dr_{\mathrm{n}} = 0.1$

Figure 3.5: Probability distributions for the error norm and compliance of the cantilever beam problem, obtained with various nodal distributions. The blue bars denote the results obtained with the random nodal distributions, the red line denotes the results found with the regular nodal distribution and the green dashed line gives the analytical value of the compliance.

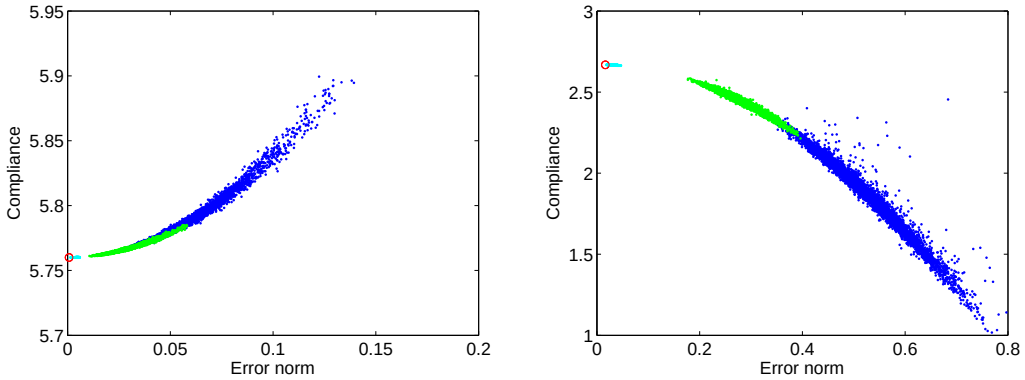

(a) Uniaxial beam (b) Cantilever beam

Figure 3.6: The relation between the error norm and the compliance of the uniaxial and cantilever beam problem. Each dot in the graph represents a sample of a nodal distribution. Here, the dark blue dots are the random distributed samples, the green dots represent the semi-random distribution with $dr_{\mathrm{n}} = 1$ and the light blue dots represent the semi-random distribution with $dr_{\mathrm{n}} = 0.1$.

interlinked. However, a difference in interdependence is observed when comparing the results for the cantilever beam with the results of the uniaxial beam (Fig. 3.6a). The uniaxial beam shows an increase in compliance when the error norm increases.

3.1.2 Local effect of the nodal position in the MLS approximation

The previous analysis showed the large influence of the nodal distribution on the accuracy of the approximation with the EFG method and that the most accurate solution to the uniaxial and cantilever beam problem is obtained with a regular nodal distribution. In order to gain better insight in the origin of this influence, the effect of local changes in a regular nodal distribution is explored. Furthermore, the complexity of the approximation is reduced by performing the analysis on the MLS approximation underlying the EFG method.

In Sec 2.1, a one dimensional function was approximated using MLS. Here, a similar example will be used, given by the scalar function

$$u(x) = x^3 - \frac{x}{2} \tag{3.8}$$

and the derivative of the scalar function

$$u_{,x}(x) = 3x^2 - \frac{1}{2}, \tag{3.9}$$

in which $0 \leq x \leq 1$. In Fig. 3.7 the approximations $u^h(x)$ and $u^h_{,x}(x)$ are shown for

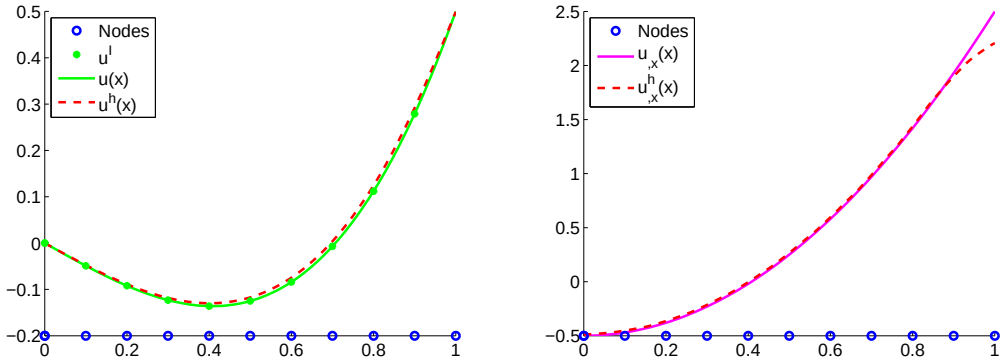

Figure 3.7: MLS approximation $u^h(x)$ and $u^h_{,x}(x)$ of Eq. 3.8 and Eq. 3.9 with n regular distributed nodes.

Table 3.2: Parameters used for the approximation with the MLS method.

Nodes	$n = 11$
Local influence domain size	$d = 2.5$
Size of monomial basis	2 (linear)

the parameters given in Tab. 3.2. Fig. 3.7 shows that the MLS approximations for both the function and its derivative are fairly accurate, although a deviation occurs for the derivative near the right boundary.

Three tests on the accuracy of the approximation will be performed in this section: the effect of the nodal influence domain size, the effect of a local increase in the nodal compaction and the effect of a difference in the nodal compaction between two areas.

The accuracy of the approximation is quantified by the following scalar:

$$||u|| = \frac{\left[\int_0^1 \{u^h - u\}^2 dx\right]^{1/2}}{\left[\int_0^1 u^2 dx\right]^{1/2}}, \tag{3.10}$$

where the $||u||$ gives the relative difference between the integral of the approximation and the considered function (Eq. 3.8). Similarly, the error for the approximation of the derivative is defined as

$$||u_{,x}|| = \frac{\left[\int_0^1 \{u^h_{,x} - u_{,x}\}^2 dx\right]^{1/2}}{\left[\int_0^1 u^2_{,x} dx\right]^{1/2}}. \tag{3.11}$$

The integrals in $||u||$ and $||u_{,x}||$ are evaluated with Gauss quadrature, in which ten

integration cells are used. To determine the precision of the numerical integration, two and eight integration points in each cell are considered separately.

Effect of nodal influence domain size

Prior to exploring the effect of the position of the nodes on the approximation, the effect of the nodal influence domain size d on the accuracy is examined.

The size of the influence domain is varied between $d = 1.1$ and $d = 5.5$. For these sizes, the errors, as defined in Eq. 3.10 and Eq. 3.11, are shown in Fig. 3.8a and Fig. 3.8b. Only small dissimilarities are observed for the two integration configurations. The accuracy of the approximation $||u||$ decreases for larger values of d. The error of the derivative of the function $||u_{,x}||$ shows a minimum at the influence domain size $d = 1.9$.

To explain this behavior, the approximation with a small influence domain $d = 1.1$ is considered first and is shown in Fig. 3.8c. The approximation to the function u^h is very accurate. However, the small influence domain makes the approximation highly variable. This adaptability causes the approximation to become very precise in the neighborhood of nodes, but reduces the accuracy between the nodes. This effect is clearly shown by the approximation of the derivative $u_{,x}$, which shows an incremental behavior.

In contrast, a large influence domain $d = 5.5$ results in a smooth approximation of u^h and $u^h_{,x}$, which is shown in Fig. 3.8d. Both u^h and $u^h_{,x}$ do not accurately approximate the nodal values. Larger values of the nodal influence domain smooth the approximations u^h and $u^h_{,x}$ further. In extreme, this effect results in approximations consisting only of terms that are included in the monomial basis $\boldsymbol{p}$ and its derivative $\boldsymbol{p}_{,x}$. The resulting MLS approximation then becomes a normal Least Squares fit. This is illustrated in Fig. 3.9, in which the monomial basis consists of a constant and a linear term, and the size of the influence domain is equal to $d = 250$.

Effect of local increase in nodal compaction

Now that the effect of the nodal influence domain size on the accuracy of the MLS approximation has been explored, the next step is to examine the effect of local changes in the nodal compaction. One extra node is added to the problem domain at different positions, and for each of the configurations the errors $||u||$ and $||u_{,x}||$ are determined. The position of the node is denoted by dx, which is the distance from the node to the left boundary.

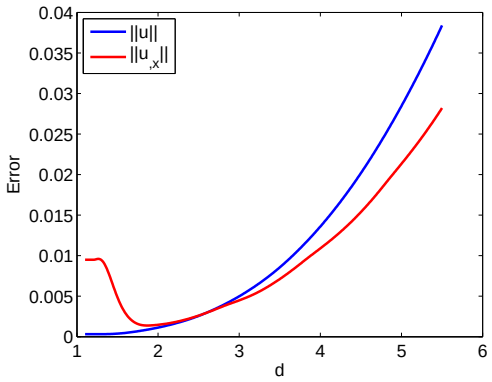

(a) Error for 2 integration points

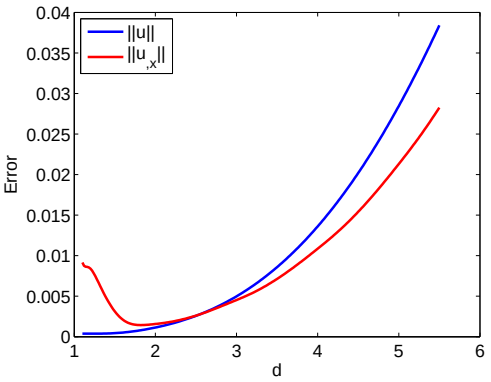

(b) Error for 8 integration points

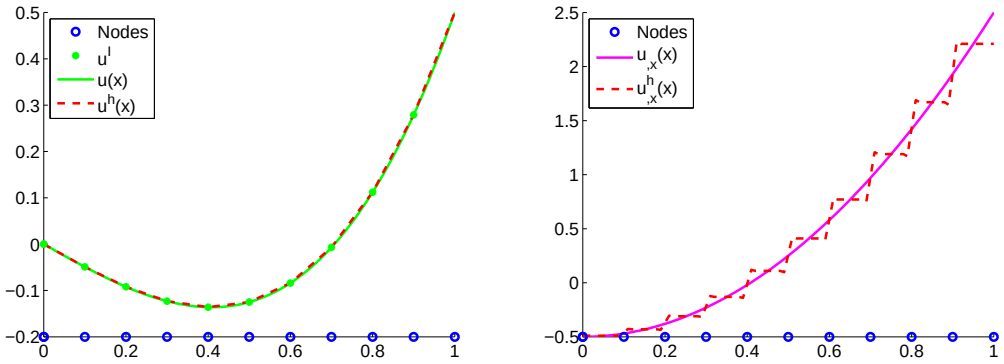

(c) $d = 1.1$

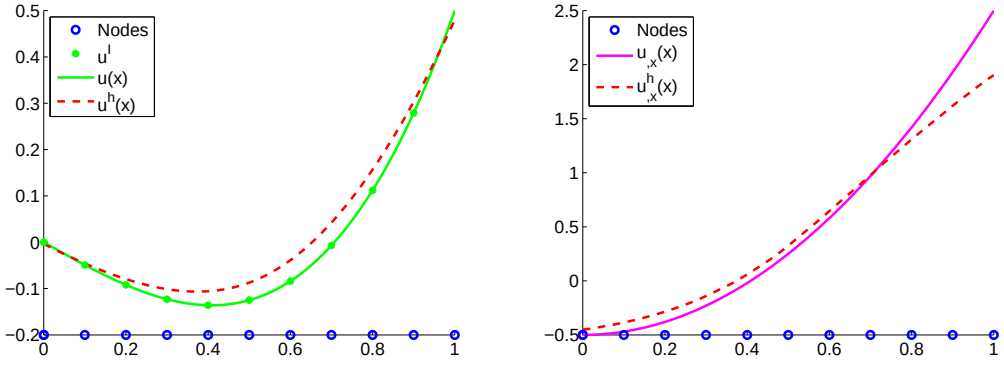

(d) $d = 5.5$

Figure 3.8: The accuracy of the MLS approximation for different nodal influence domain sizes d. The approximations u^h and $u^h_{,x}$ are for $d = 1.1$ and $d = 5.5$.

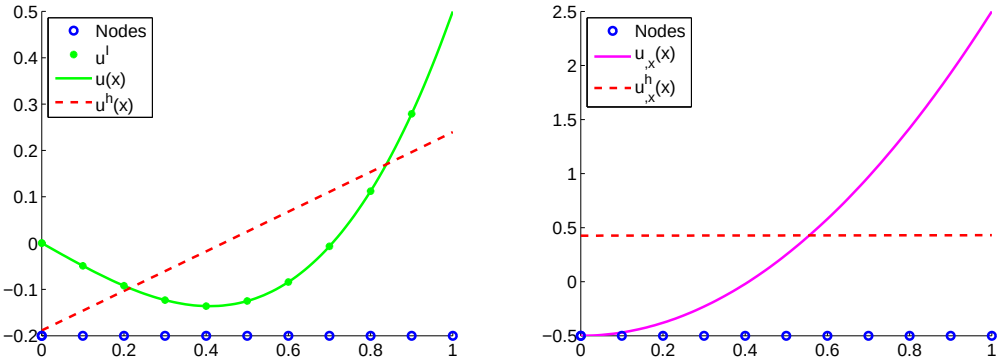

Figure 3.9: The approximations u^h and $u^h_{,x}$ for $d = 250$.

The values obtained for the errors $||u||$ and $||u_{,x}||$ are shown in Fig. 3.10a and Fig. 3.10a. First, these figures clearly show that adding an extra node does not necessarily result in a higher accuracy. The approximation of the derivative u^h depends greatly on the position of the extra node. In Fig. 3.10a, almost all nodal positions dx result in lower accuracy. To explain this effect, the two different positions of the extra node, the approximations u^h and $u^h_{,x}$ are shown in Fig. 3.10c and Fig. 3.10d. The precision of u^h for the two different nodal distributions increases locally around the coordinates of the extra node. This has the negative effect that $u^h_{,x}$ shows oscillations and is thus not approximated correctly.

These oscillations makes the numerical integration more difficult. This effect is shown Fig. 3.10a and Fig. 3.10a, in which the integration of $||u_{,x}||$ depends on the number of integration points in each cell.

Effect of divergence in nodal compaction between two areas

The previous test shows that a local change in nodal compaction does not necessarily result in a better approximation. The change in accuracy, caused by varying the nodal compaction for the approximations u^h and $u^h_{,x}$, is further explored here. By locally increasing the nodal compaction further than in the previous test, the effect of a discrete change in nodal compaction is investigated.

In order to introduce the increment in the nodal compaction, the domain is split into two. The number of nodes in the right part of the problem domain remains the same (five nodes), while the number of nodes in the left halve of the problem domain is increased to numbers between five and forty nodes. The error (Eq. 3.10 and Eq. 3.11) is calculated separately for both halves.

The result for the errors $||u||$ and $||u_{,x}||$ are shown in Fig. 3.11a and Fig. 3.11b. First, note that there is a large difference between the numerical integration for

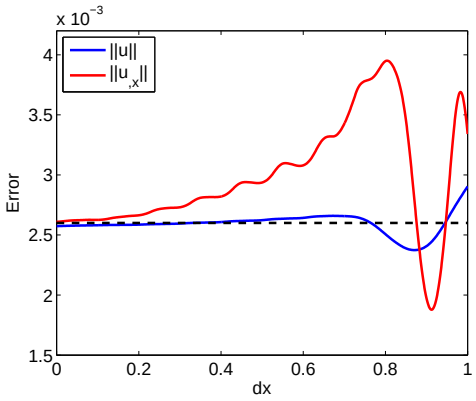

(a) Error for 2 integration points

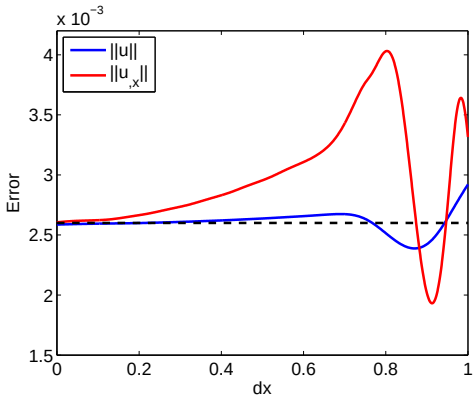

(b) Error for 8 integration points

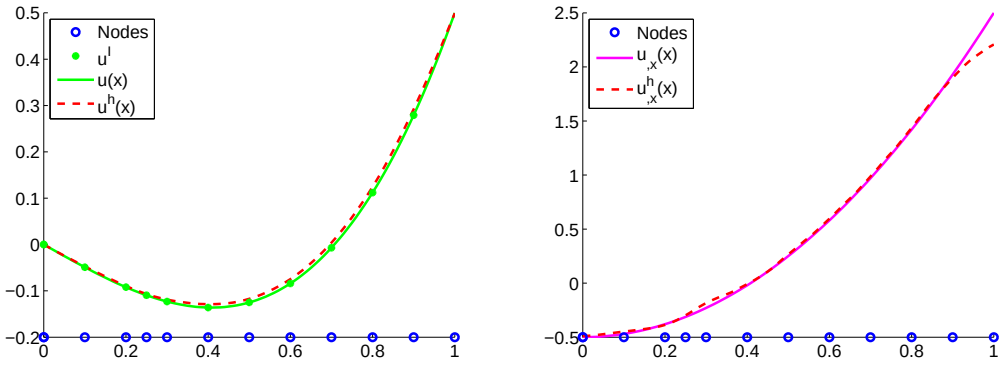

(c) Example $dx = 0.25$

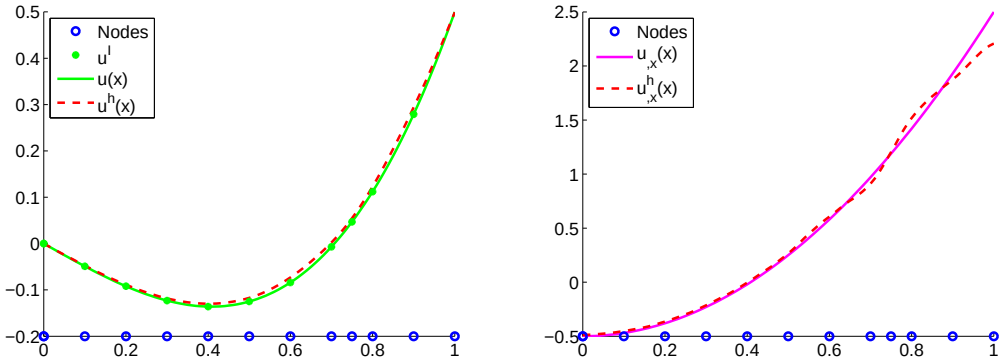

(d) Example $dx = 0.75$

Figure 3.10: Change in accuracy of the MLS approximation by locally adding an extra node. The approximations u^h and $u^h_{,x}$ are given for two positions of the extra node and dx represents the distance between the position of the extra node and the left boundary.

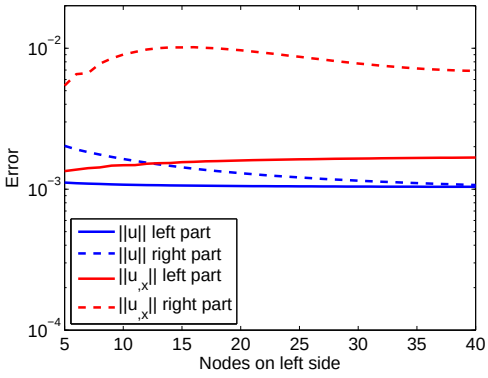

(a) Error for 2 integration points

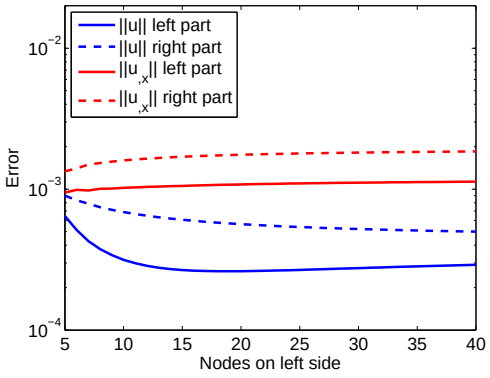

(b) Error for 8 integration points

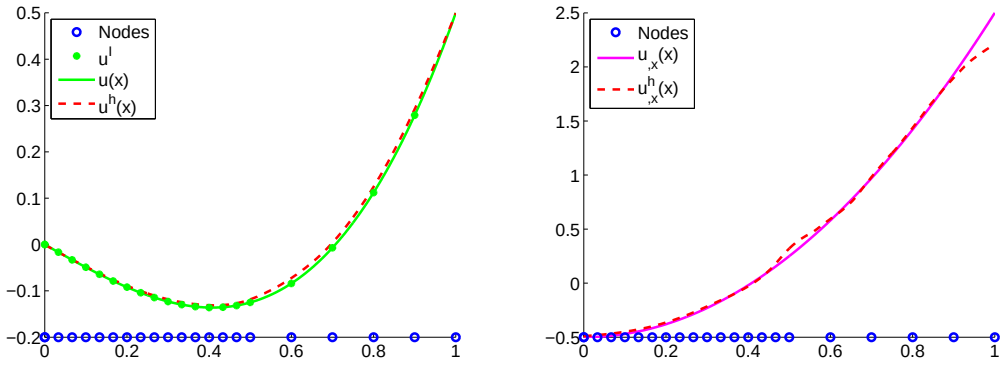

(c) 15 nodes on the left

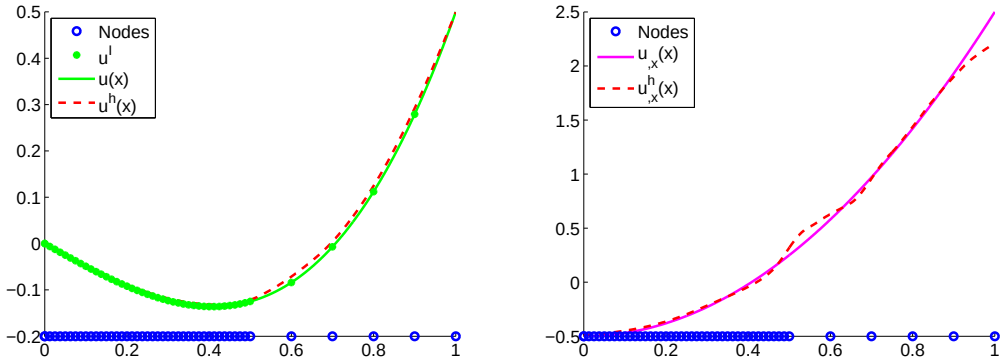

(d) 40 nodes on the left

Figure 3.11: Change in accuracy of the MLS approximation by divergence in nodal compaction between two areas. The approximations u^h and $u^h_{,x}$ are given for two values of the nodal compaction on the left side: 15 nodes and 40 nodes.

two and eight integration points. Although this error does not influence the results of the MLS approximation, it will influence the results of the EFG method.

Second, Fig. 3.11b shows that both u^h and $u^h_{,x}$ depend on the nodal compaction on the left part of the domain. Overall, $||u||$ decreases and $||u_{,x}||$ increases when there are more nodes in the domain. This error increase is caused by an oscillation in the approximation of the derivative. In Fig. 3.11c this oscillation is shown for fifteen nodes on the left side and in Fig. 3.11d for forty nodes. For these two nodal distributions, the approximation of u^h is only slightly affected.

3.2 Effect of the nodal position on the material distribution

So far only domains with homogeneously distributed material have been considered, i.e. the distribution of nodes was chosen such that at each coordinate $\boldsymbol{x}$ in the problem domain the support domain Ω^x contained enough nodes. In the MNA the problem domain is altered by changing the position of the nodes. Therefore, it is necessary to gain a clear understanding of the influence of the nodal position on the distribution of material. Moreover, so far the background mesh in the EFG method always coincided with the problem domain. However, for curved boundaries in topology optimization the background mesh will not exactly coincide with the problem domain.

In this section, the influence of the nodal position on the material distribution is discussed first. Second, the accuracy of the solution to the uniaxial and cantilever beam problems are determined for problem domains that do not coincide with the background mesh.

3.2.1 Complexly shaped material distribution

Part of a problem domain Ω and part of its boundary Γ are shown in Fig. 4.6. The boundary Γ is used to distribute nodes inside the problem domain. However, in most problems the boundary is not exactly known, and will be determined from the nodes. In this section the boundary following from the nodal distribution will be discussed. Note that the boundary of the problem domain does not coincide with the boundary of the rectangular integration cells (black dashed lines) and thus some of the integration cells, completely or partly, fall outside the problem domain Ω.

Material is distributed at a coordinate $\boldsymbol{x}$ inside the problem domain when two conditions are fulfilled. First, the coordinate must lie within an integration

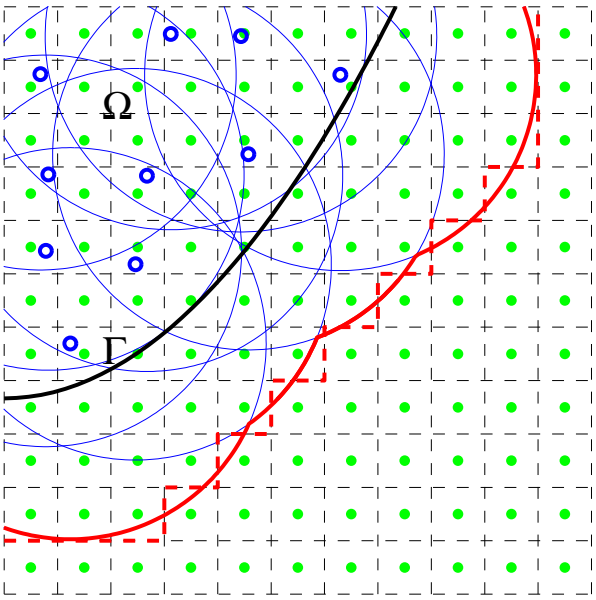

Figure 3.12: Example of a problem domain Ω enclosed by its boundary Γ that does not coincide with the background mesh. Here, the blue circles are the nodes, the blue lines are the boundaries of the nodal influence domain, the dashes black lines are the boundaries of the integration cells and the green dots are the integration points. The red line corresponds with the material domain and the dashed red line is the discrete boundary of the material domain.

cell. Second, the coordinate must have a node in its support domain.[4] When the domain boundary Γ is not exactly covered by the boundary of integration cells, these two conditions result in a distribution of material that does not coincide with the problem domain.

This effect is shown in Fig. 3.12. For some coordinates outside the problem domain Ω, the two conditions are fulfilled. This results in a shift of the boundary from the original position (black line) to the red line. If integration would be exact, all coordinates within the red boundary are covered by material and all coordinates outside the red boundary do not contain any material. However, since integration is done numerically, another shift of the boundary occurs.

A typical background mesh is shown in Fig. 3.12, in which the integration cells contain one integration point. For all integration points within the red boundary, the shape functions can be determined and material is distributed. Since the integration points represent part of the complete area, the real boundary of the problem domain becomes discrete, following the boundary of the integration

[4]This condition holds for a monomial basis $\boldsymbol{p}$ containing only one term. If the monomial basis contains more than one term, the support domain should contain more nodes.

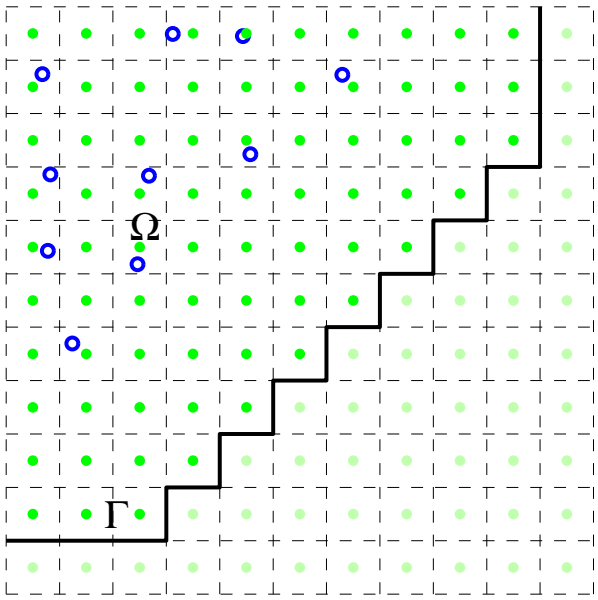

Figure 3.13: Example of a problem domain Ω enclosed by its boundary Γ. The bright green dots are the active integration points, the light green dots are the inactive integration points, the dashed black lines are the boundaries of the integration cell and the blue circles are the nodes.

points.[5] This boundary is depicted in Fig. 3.12 by the red dashed line. Fig. 3.13 shows the final material distribution Ω enclosed by the boundary Γ. Only the shape functions for the bright green integration points are unequal to zero.

Actually, the aforementioned second conditions should be taken more strict. More terms in the monomial basis $\boldsymbol{p}$ increase the number of nodes that should be present inside the support domain of each coordinate $\boldsymbol{x}$. When considering the MLS approximation, matrix $\boldsymbol{A}(\boldsymbol{x})$ has to be inverted to find the coefficients $\boldsymbol{a}(\boldsymbol{x})$(see Eq. 2.34). The size of $\boldsymbol{A}(\boldsymbol{x})$ is given by the number of monomials in $\boldsymbol{p}$. There should be enough nodes in the support domain of $\boldsymbol{x}$ to prevent the $\boldsymbol{A}(\boldsymbol{x})$ from being singular.

In further study, only the integration points with a non-singular $\boldsymbol{A}(\boldsymbol{x})$ matrix are taken into account. Thus, depending on the order of the monomial basis and the size of the influence domain d, the boundary of the material distribution is either closer or further away from the boundary of the preferred problem domain.

[5]This representation of the discrete boundary can only be visualized for the case of one integration point, because integration with Gauss Quadrature with one integration cell can only evaluate constant functions. For higher order Gauss Integration the discreteness of the integration still exists, but it can't be shown as a discrete boundary as in Fig. 3.12.

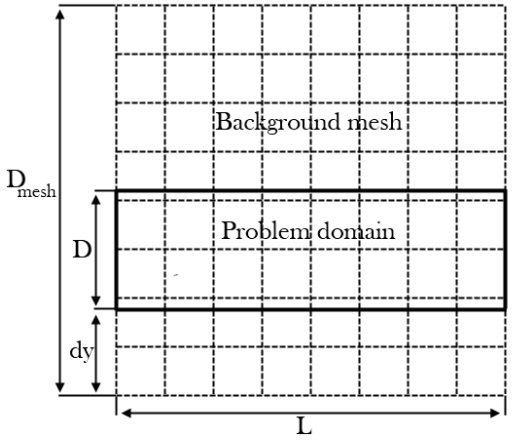

Figure 3.14: The problem domain in the uniaxial beam for various configurations of the background mesh, given by $0 \leq dy \leq D_{mesh} - D$ or $0 \leq dy \leq 8$.

Table 3.3: Parameters for the uniaxial beam, used in the EFG method.

Nodes in x_1 direction	$n_1 = 10$
Nodes in x_2 direction	$n_2 = 10$
Influence domain shape	rectangular
Average nodal distance in x_1 direction	$d_1 = L/[n_1 - 1]$
Average nodal distance in x_2 direction	$d_2 = D/[n_2 - 1]$
Local influence domain size	$d = 2.5$
Size of monomial basis	2 (linear)
Integration cells in x_1 direction	$m_1 = 9$
Integration cells in x_2 direction	$m_2 = 27$
Boundary integration cells in x_2 direction	$m_2 = 9$
Integration points per cell	$n_g = 4$

3.2.2 Material distribution exemplary problem

In this section, the effect caused by non-coinciding material and problem domain is illustrated by use of an exemplary problem. Different configurations between the nodes and background mesh are considered. For these configurations the error norm and compliance are determined and compared.

The problem domain as shown in Fig. 4.6 is considered in this section. The model constants are $D = 4$, $L = 48$, $E = 1$ and $\nu = 0.3$. The different configurations of the discretization are constructed by moving the problem domain vertically through a fixed background mesh with a height of $D_{mesh} = 12$. These configurations are shown in Fig. 3.14, in which the distance with respect to the lower boundary of the integration cells is given by $0 \leq dy \leq D_{mesh} - D$ or $0 \leq dy \leq 8$.

The problem domain is discretized with a regular nodal distribution. In con-

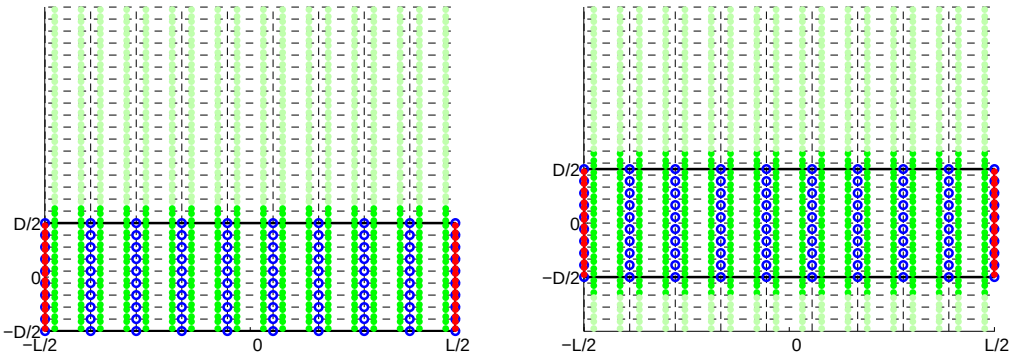

(a) Integration points nodal influence domains are considered

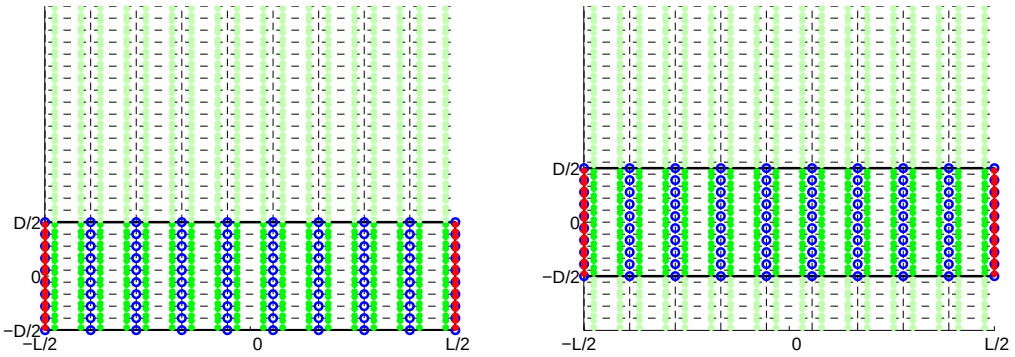

(b) Integration points outside the problem domain are deactivated

Figure 3.15: Discretization of the problem domain with non-coinciding background mesh.

trast to the internal integration points, the boundary integration points are fixated to the problem domain. Unless otherwise noted, the parameters used to solve the uniaxial beam problem are given in Tab. 3.3. The discretization is shown in Fig. 3.15a for $dy = 0$ and $dy = 2$. The black line represents the boundary of the problem domain, which is filled with nodes represented by the blue circles. The bright green dots are the active internal integration points, the lighter green dots are the inactive integration points and the red points are the boundary integration points. The material distribution in Fig. 3.15a is given by the active integration points. Clearly, these integration points lie outside the problem domain. This results in a volume increase. A normalized volume is calculated by dividing the volume of the material distribution by the volume of the original problem domain.

To determine the influence of the background mesh position on the material distribution, the results for the uniaxial beam are obtained for $0 \leq dy \leq 8$. In Fig. 3.16 the error norm, compliance and normalized volume are depicted in blue.[6] The analytical value for the compliance is given by the green dashed line. The results show a normalized volume greater than one, which results in a compliance lower than the analytical compliance. Moreover, two other effects can be identified. The first is an oscillatory behavior of the error norm and compliance. This effect is caused by the interaction between the fixed equally spaced integration cells and the non-coinciding problem boundary. Moving the problem domain continuously for $0 \leq dy \leq 8$, results in a material domain that changes discontinuous (shown as the normalized volume in Fig. 3.16). This also results in a discontinuous change in the compliance and the error norm. The second effect is observed when the problem domain is close to the top and bottom boundaries of the background mesh. At these positions the material is reduced, since less integration points are present at these boundaries.

To let the material domain fit more closely to the problem domain, the discretization of the problem domain can be improved by manually deactivating the integration points outside the problem domain. Two samples of these arrangements are shown in Fig. 3.15b. In Fig. 3.16 the results are shown (in red) when only considering the integration points inside the problem domain.[7] For these arrangements, the normalized volume equals one.[8] Moreover, a lower error norm is observed and the compliance corresponds better to the analytical compliance.

[6] The displacement and stress for $dy = 0, 4, 4.1$ are shown in App. B in Fig. B.3.

[7] The displacement and stress for $dy = 0, 4, 4.1$ are shown in App. B in Fig. B.4.

[8] The volume stays constant since each time a new integration point enters the problem domain at the top, another integration cells leaves the problem domain at the bottom. This does not necessarily have to be the case, and a different size of integration cells could change the normalized volume with the position dy.

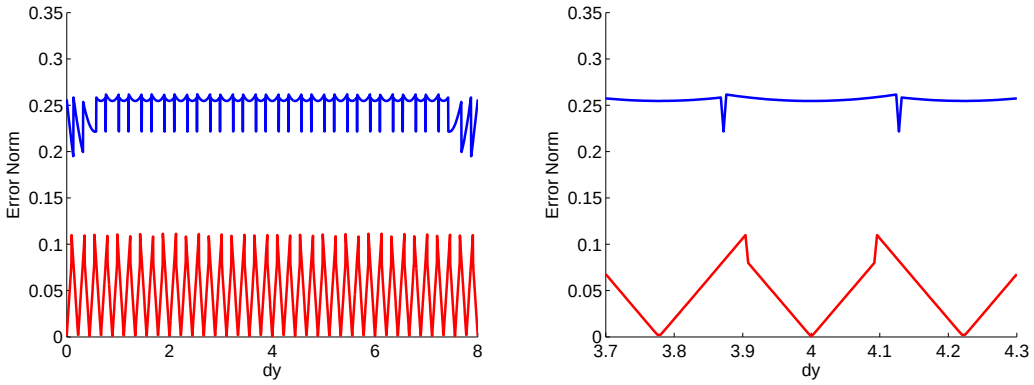

(a) Error norm

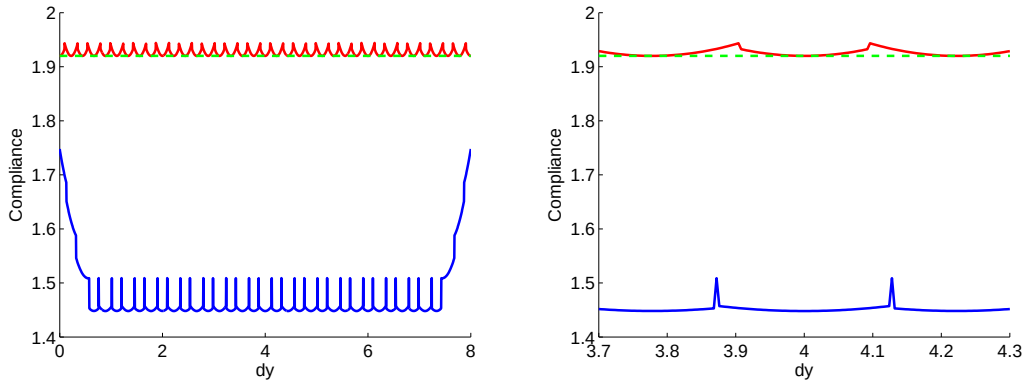

(b) Compliance

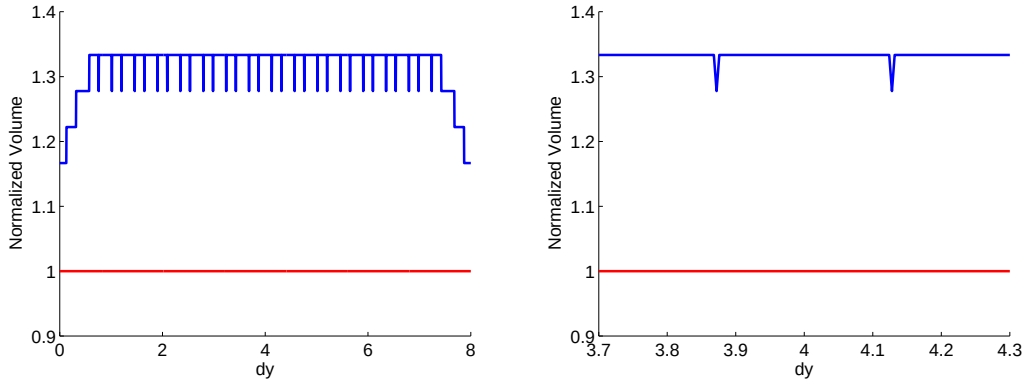

(c) Normalized volume

Figure 3.16: Compliance and error norm for various configurations of the problem domain and background mesh. These configuration are given by $0 \leq dy \leq D_{mesh} - D$ or $0 \leq dy \leq 8$ and shown in Fig. 3.14. Moreover, the blue lines denote the results obtained by considering integration points inside the nodal influence domains, and the red lines denote the results obtained by only considering the integration points inside the problem domain.

3.3 Requirements for the MNA

In Sec. 3.1.1 the effect of nodal distributions on the accuracy of the EFG method has been investigated. Distributing the nodes randomly, results in inaccurate approximations. Furthermore, for the MLS approximation (Sec. 3.1.2) local changes in the nodal compaction cause oscillations in the approximation of the derivative. These oscillations also influence the solutions obtained with the EFG method for irregular nodal distribution.

To find the optimal layout with the MNA in topology optimization, the nodes will be moved through the domain. It is likely that the movement of the nodes, results in an irregular nodal distribution. For example, consider a topology optimization of a cantilever beam, in which the domain volume should be halved and the compliance should be minimized. According to Fig. 3.5 it is possible to redistribute the nodes and lower the compliance, while maintaining the same volume. However, this low compliance corresponds to a highly inaccurate solution of the cantilever beam problem and should be avoided.

To overcome the problems caused by an irregular nodal distribution, a requirement for the MNA should be:

The nodes used in the discretization of the EFG method should remain equally spaced.

The effect of the nodal distribution on the material distribution has also been examined. There are some difficulties in the representation of material. First, Sec. 3.2 showed that various nodal distributions can result in the same material distribution. Nodes which lie close to the boundaries of the background mesh or are enclosed by other nodes, do not influence the material domain. Moreover, Sec. 3.2 showed that near boundaries of the problem domain material is distributed, while no nodes are present. This is caused by an interaction between the integration points from the background mesh and the nodal influence domains. The same interaction also results in a discrete material distribution.

These problems are mainly caused by the MLS approximation and the numerical integration. In the approximation, the sum of the shape functions equals one inside the nodal influence domains. If a coordinate does not lie inside any nodal influence domain, all shape functions are zero. Therefore the material distribution is discontinuous, i.e. either material exists or it does not exist. The shape of this discontinuous material distribution is therefore not influenced by internal

nodes, and only material near boundaries can be added or removed by changing the nodal position.

In the MNA these aforementioned problems in the material distribution should be avoided. A possible approach to solve these problems is to let the density of the material depend on the nodal compaction. The material distribution then becomes directly related to the nodal position, also for internal nodes. Moreover, the discrete nature of the material boundary can be softened by changing the density of the material continuously. Since the compaction of nodes decreases near boundaries, the material density decreases too.

Therefore, the following question arises:

Does the material distribution become more suited for the MNA by directly relating the material density to the compaction of the nodal distribution?

Chapter 4

Material distribution defined by nodal compaction

In Chap. 3 two difficulties have been identified for the discretization of structures with the EFG method. The first difficulty is the decrease in accuracy of the EFG method for irregular nodal distributions (see Sec. 3.1). In the current EFG method formulation, internal nodes can be displaced without changing the material distribution. However, these differences in the nodal distribution affect the accuracy of the discretization. The second difficulty arises in the discretization of complexly shaped structures (see Sec. 3.2). For these discretizations, an interaction between the background mesh and the nodal influence domains results in a discontinuous material distribution. Moreover, in the material distribution relatively large areas do not contain nodes, decreasing the solution accuracy. These two problems can be avoided for the discretization of regular material domains by using regular nodal distributions and by fitting the background mesh to the problem domain. However, complex material domains and irregular nodal distributions are likely to occur in the MNA in topology optimization. Therefore, a different approach needs to be applied in the MNA.

In order to solve the above-mentioned problems, this chapter introduces a continuous material density that depends on the nodal compaction. Applying this material density to the EFG method results in a material distribution without discontinuities. Moreover, the material density introduces a direct coupling between the nodal position and the shape, i.e. displacing nodes will result in changes of the shape. This chapter comprises the discussion and evaluation of the material density that depends on the nodal compaction. Sec. 4.1 describes the material density based on the nodal compaction. In this section the constant density material distribution (hereafter: original material distribution) is replaced with a material

distribution in which the density is based on the nodal compaction (hereafter: nodal compaction material distribution). In Sec. 4.2 the nodal compaction material distribution is evaluated by solving several exemplary problems with fixed nodal distributions. With these simulations the characteristics and performance of this material distribution can be compared to the original material distribution. Furthermore, Sec. 4.3 explores disparities in behavior of the structure for variations in the nodal distribution. These differences are expressed as the sensitivity of the compliance to changes in the nodal position (hereafter: compliance sensitivity). The underlying cause of the variations in behavior are then derived from the compliance sensitivity. Finally, the possibilities for applying the nodal compaction material distribution in the MNA in topology optimization are discussed in Sec. 4.4.

4.1 Material density based on the nodal compaction

In this section, a continuous material density depending on the nodal compaction is introduced in order to overcome some of the difficulties arising when describing irregular material distributions with the EFG method. A typical meshless method in which the material density is continuous and depends on the nodal compaction is the SPH method [16]. Similarly, this approach can be applied to introduce a continuous material density in the EFG method. The SPH method is based on the kernel approximation (see Sec. 2.1.2), in which the density is expressed as

$$\rho(\boldsymbol{x}) = \sum_{I=1}^{n} m^I W(\boldsymbol{x} - \boldsymbol{x}^I, d^\rho), \tag{4.1}$$

where n is the number of nodes, W is a kernel function, m^I is a mass belonging to node I and d^ρ characterizes the size of the support domain Ω^x of $\boldsymbol{x}$. Following from this equation a fixed amount of mass m^I is distributed around each node I according to the shape and size of the kernel function.

Fig. 4.1 shows the density distributions for a one-dimensional regular nodal distribution with $d^\rho = 1, 1.25, 1.5, 1.75, 2, 2.25$. In these examples the cubic spline weight function (Eq. 2.16) is used and the nodal mass equals $m^I = dn = L/(n-1)$, where dn is the distance between nodes.[1] From the same figure the influence of the domain size d^ρ on the density distribution can be determined by comparing

[1] This choice of the mass results in a normalized density. The normalized density has an average value of one in regions with regular distributed nodes and has a density of zero for regions without nodes. Intermediate densities are present near outer nodes and can also be present between internal nodes.

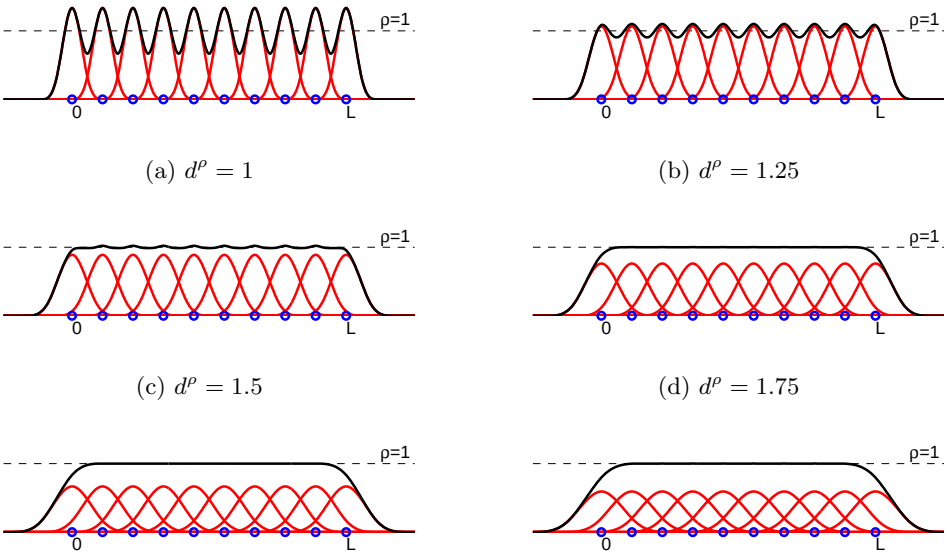

(a) $d^\rho = 1$ (b) $d^\rho = 1.25$

(c) $d^\rho = 1.5$ (d) $d^\rho = 1.75$

(e) $d^\rho = 2$ (f) $d^\rho = 2.25$

Figure 4.1: One-dimensional examples of the material density for a regular nodal distribution. The blue circles denote the nodal positions, the red lines denote the kernel functions, the black line denotes the density.

the various density distributions. The density oscillates for smaller values of d^ρ. Moreover, only small areas with nonzero density exist near the outer nodes. In contrast, larger values of d^ρ give a smoother density distribution, resulting in larger areas with nonzero density near the outer nodes.

Fig. 4.2 shows examples of density distributions for a two-dimensional square nodal distribution. In these examples, the density has been normalized using a nodal mass is $m^I = dn_1 dn_2$. Here, dn_1 and dn_2 is the distance between nodes in the x_1 and x_2 direction, respectively. Similar oscillating and smoothing effects to those in the one-dimensional examples of the density distribution can be observed (Fig. 4.1).

When using the nodal compaction material distribution in the EFG method, the total mass of the structure equals

$$m_{tot} = \int_\Omega \rho(\boldsymbol{x}) d\Omega = \sum_{I=1}^{n} m^I, \tag{4.2}$$

which follows from the unity conditions of the kernel function (Eq. 2.13) and the constant nodal mass m^I. This is the exact value of the total mass. However, numerical integration of the density in the EFG method could result in a variations of the total mass.

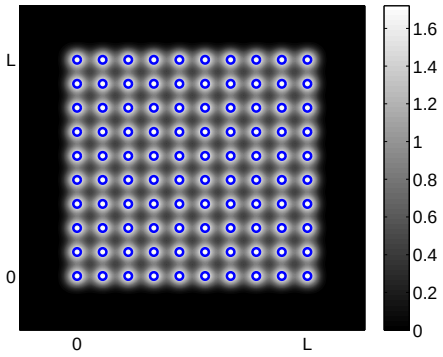

(a) $d^\rho = 1$

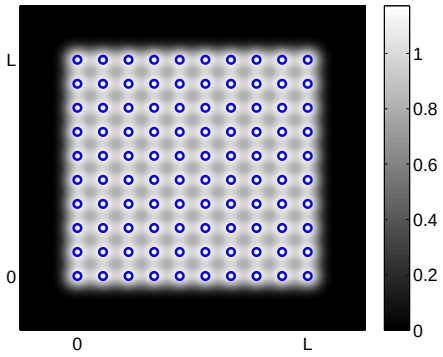

(b) $d^\rho = 1.25$

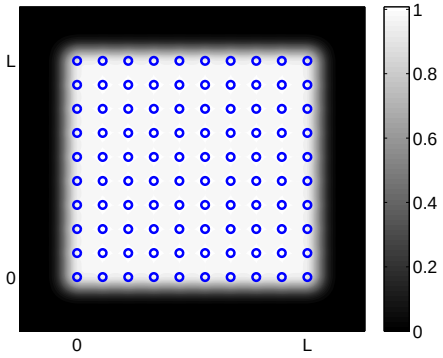

(c) $d^\rho = 1.5$

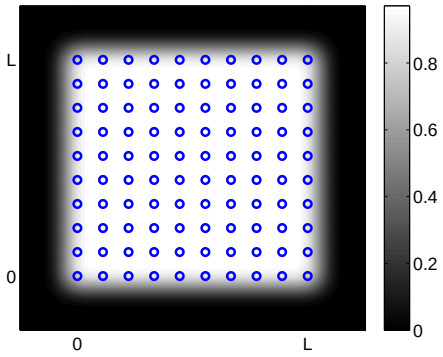

(d) $d^\rho = 1.75$

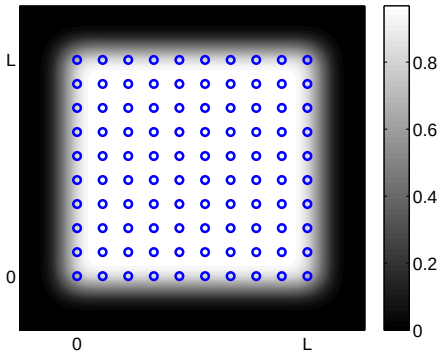

(e) $d^\rho = 2$

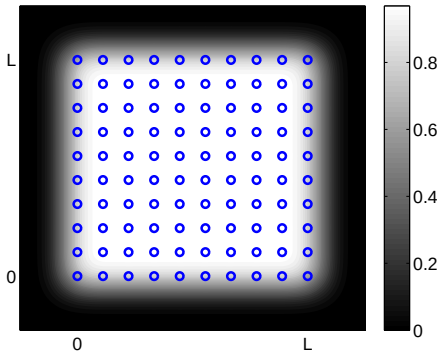

(f) $d^\rho = 2.25$

Figure 4.2: Two-dimensional examples of the material density for a regular nodal distribution. The blue circles denote the nodal positions and the grey contours the density.

The nodal compaction material distribution is introduced in the EFG method by scaling the stiffness of the material with the normalized density:

$$E^{\rho}(\boldsymbol{x}) = \rho(\boldsymbol{x})E, \tag{4.3}$$

in which E is the constant Young's modulus of the original material distribution and $E^{\rho}(\boldsymbol{x})$ is the scaled Young's modulus in the nodal compaction material distribution. By replacing E with $E^{\rho}(\boldsymbol{x})$ in the EFG method, the Young's modulus becomes dependent on the nodal compaction.

Note that the nodal influence domain size d used in the MLS approximation does not need to be the same as the nodal influence domain size d^{ρ}. However, to ensure a continuous density distribution in the neighborhood of outer nodes, d^{ρ} should be smaller than d. Moreover, d^{ρ} should be chosen small enough such that $\boldsymbol{A}$ in the MLS approximation (Eq. 2.32) does not become singular. Although, using values of d^{ρ} that are too small will lead to oscillations in the density distribution. So far using $2.5 \leq d \leq 3.5$ provided the most favorable characteristics of the EFG method. Therefore, following from the above-mentioned bounds to d^{ρ}, choosing $d^{\rho} = 1.5$ for further investigation seems reasonable.

4.2 Characteristics of regular nodal distributions

The nodal compaction material distribution has been introduced in Sec. 4.1 to provide for a substitution of the original material distribution. Difficulties arising from the original material distribution are hopefully reduced or avoided by this substitute. However, at this point the full potential of the nodal compaction material distribution is not exactly known. Therefore, the performance and general characteristics of the EFG method comprising the nodal compaction material distribution is investigated in this section. To increase insight in the nodal compaction material distribution, this first investigation comprises only regular nodal distributions.

The further investigation of the nodal compaction material distribution is based on the two-dimensional cantilever beam exemplary problem, and consists of three parts. First, in Sec. 4.2.1 the displacement and stress in the cantilever beam are compared for the original and nodal compaction material distribution. The general characteristics of the EFG method comprising the nodal compaction material distribution can be determined from this first exploration. Second, in Sec. 4.2.2 the influence of the background mesh position relative to the nodal positions is investigated. Again, the displacement and stress in the cantilever

beam are compared for the nodal compaction and original material distribution. These results provide insight in the influence of the background mesh on the material distribution. Third, a study is performed in Sec. 4.2.3 on the influence of the nodal positions on the material distribution. In principle the nodal positions define the shape. However, non-physical coupling between nodes caused by the large nodal influence domains might occur. Therefore, various nodal distributions with differences in the nodal positions are examined. Again, the investigation is performed based on an exemplary problem.

For all three aforementioned studies, the performance of the EFG method comprising the nodal compaction material distribution is derived from the compliance C and the total mass m_{tot}. Here, the total mass of the structure is determined from numerically integrating the density at the Gauss integration points.

4.2.1 General characteristics

In this section a study is performed on the general characteristics of the EFG method comprising the nodal compaction material distribution. The dissimilarities between the original and nodal compaction material distribution are obtained by comparing the solutions of an exemplary problem. From these differences the general characteristics of the nodal compaction material distribution can be derived.

Similar to previous studies, the cantilever beam problem is used as the exemplary problem. The problem domain and background mesh for the cantilever beam are shown in Fig. 4.3b, with model constants $D = 1$, $L = 1$, $E = 1$ and $\nu = 0.3$. The left edge of the problem domain is fixed and on the right edge a constant downward traction $P = 0.1$ is applied. The problem domain is discretized with a regular nodal distribution, such that the internal normalized density is approximately one. The left and right edge of the problem domain are discretized with boundary integration cells. The discretization parameters of the nodal distribution and the background mesh are given in Tab. 4.1. For these parameters the nodes and integration points are shown in Fig. 4.3b. Here, the background mesh has been chosen large enough such that the nodal influence domains do not cross the global boundary of the background mesh (hereafter: semi-infinite background mesh). Although the nodal distribution is regular, the combination between this background mesh and nodal distribution captures the essence of the discretization of complexly shaped domains, i.e. the non-coincidence of the background mesh with the nodal distribution. Therefore, the investigation of these regular material distributions also provide insight in more complexly material distributions.

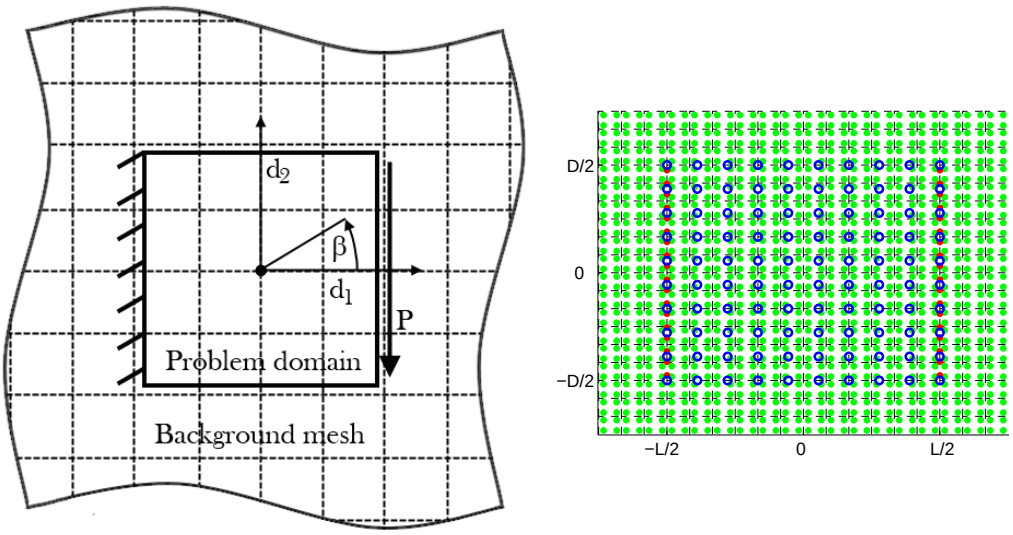

(a) Model (b) Discretization

Figure 4.3: Problem domain and background mesh of a typical cantilever beam problem. By translating the background mesh according to d_1 and d_2 and by rotating the background mesh according to β the influence of the position of the background mesh on the solution to the cantilever beam problem can be investigated. The problem domain is discretized with nodes (blue circles) and integration points (green and red dots).

Table 4.1: EFG method parameters.

Nodes in x_1 direction	$n_1 = 10$
Nodes in x_2 direction	$n_2 = 10$
Influence domain shape	rectangular
Average nodal distance in x_1 direction	$dn_1 = L/[n_1 - 1]$
Average nodal distance in x_2 direction	$dn_2 = D/[n_2 - 1]$
Local influence domain size	$d = 3.5$
Density influence domain size	$d^\rho = 1.5$
Nodal mass per node	$m^I = dn_1 dn_2$
Size of monomial basis	2 (linear)
Size background cell in x_1 direction	$dm_1 = dn_1$
Size background mesh in x_2 direction	$dm_2 = dn_2$
Integration points per cell	4
Number of boundary cells along left and right edge	9

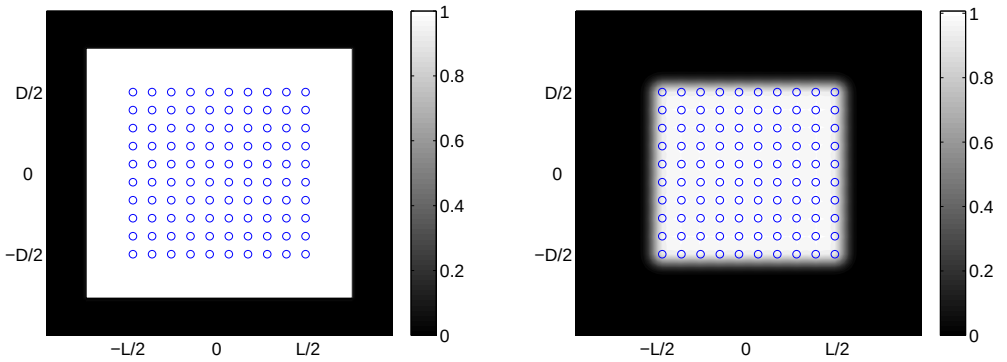

(a) Original material distribution

(b) Nodal compaction material distribution

Figure 4.4: Density and nodal distributions for the cantilever beam problem (Fig. 4.3). The blue circles denote the nodes and the grey contours the density.

First, the normalized density of the original and nodal compaction material distributions are shown in Fig. 4.4. Since a semi-infinite background mesh is used, additional mass is distributed near the outer nodes. In these regions the original material distribution deviates the most from the nodal compaction material distribution. This difference also appears in the total mass of the structures, which equals 2.42 and 1.24 for the original and nodal compaction material distribution respectively. The dissimilarity between the density distributions results in variations in the compliance. For the original material distribution the compliance equals 0.035 and for the nodal compaction material distribution the compliance equals 0.055.

Second, the displacement and stress in the cantilever beam for both material distributions are shown in Fig. 4.5 and Fig. 4.6. For these distributions, the displacement of the cantilever beam has the same profile. However, the difference in total mass results in a large variation in the the magnitude of the displacement. Moreover, the solution of the original material distribution shows erratic stress peaks near the outer nodes. In contrast, the stress near outer nodes in the nodal compaction material distribution reduces to zero, which is the result of the decrease in density.

The outcome of the considered exemplary problem shows that the accuracy of the solution deteriorates in areas without nodes. Since the density in the nodal compaction material distribution is reduced in these areas, the influence of these areas on the accuracy is also decreased. Therefore, the nodal compaction material distribution provides for an effective method of increasing the accuracy of the solution for complexly shaped domains, provided that the nodal distribution

is regular.

4.2.2 Changes in the background mesh position

Previous sections showed that the nodal compaction material distribution reduces the material density in areas without nodes. This reduces the erratic stress peaks present in the solution occurring when using the original material distribution. In this section the study on the performance of the nodal compaction material distribution is continued by investigating the influence of the background mesh on the solution. In principle, this influence should not appear in the material distribution, since it is purely a numerical artifact. However, Sec. 3.2.2 showed that the background mesh causes discontinuities in the material distribution. Therefore, displacement of the background mesh resulted in discontinuous behavior of the solution. The nodal compaction material distribution has been introduced to reduce these problems. However, this material distribution should be further tested to determine its full potential. Therefore, this section explores the influence of displacements in the background mesh relative to the nodal position when using the nodal compaction material distribution. The results are compared to results obtained when using the original material distribution.

The aforementioned investigation is performed on the same cantilever beam problem as in Sec. 4.2.1. This relatively simple problem will provide enough insight in the workings of the nodal compaction material distribution. For the cantilever beam problem, the changes in compliance and mass are determined for a translation of the background mesh by a distance[2] of $0 \leq d_1 \leq dn_1$ and $0 \leq d_2 \leq dn_2$ and a rotation of the background mesh to an angle[3] $0 \leq \beta \leq \pi/4$.

The mass and compliance for these translations and rotations are shown in Fig. 4.7. In this figure the mass and compliance have been normalized with the mass and compliance of the initial configuration ($d_1 = d_2 = \beta = 0$). For the original material distribution, the mass changes discontinuously when rotating the background mesh (Fig. 4.7c),[4] resulting in a compliance discontinuity when an integration point is added or removed from the material domain. Similarly, discontinuities arise in the compliance for translations of the background mesh.

[2] Because the background mesh is periodic, larger values of the translation d_1 and d_2 give the same results.

[3] Since the size of the cells of the background mesh, the size of the problem domain and the distance between the nodes in both directions are equal, larger values for the angle β give the same result.

[4] This discontinuity is not found for the translation of the background mesh (Fig. 4.7a and Fig. 4.7b). The mass is constant because the number of integration points is constant. Each time an integration points leaves the material domain on one side, a different integration points enters the material domain on the opposite side. However, a different choice in background mesh size could result in discontinuities in the mass.

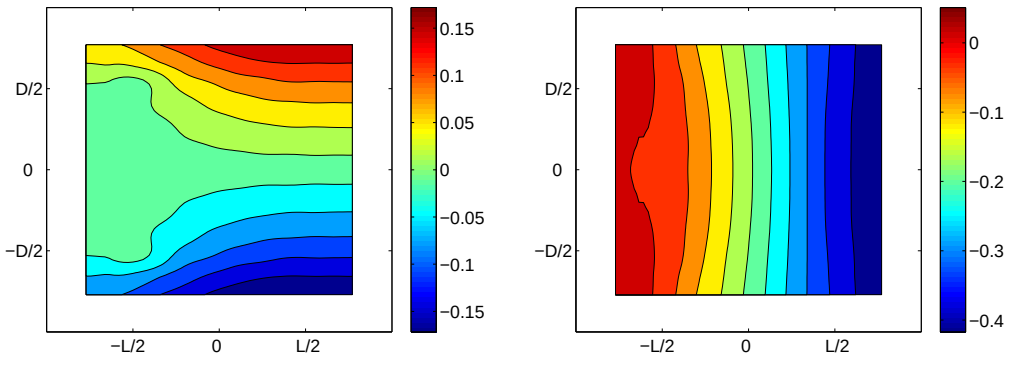

(a) $u_1^h(\boldsymbol{x})$

(b) $u_2^h(\boldsymbol{x})$

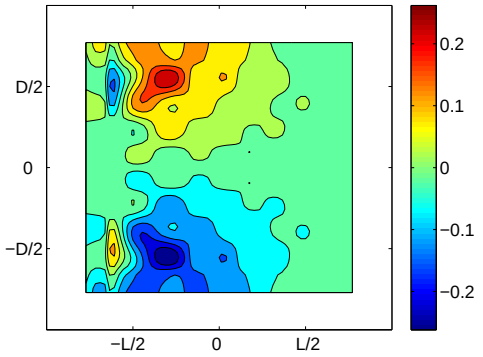

(c) $\sigma_{11}^h(\boldsymbol{x})$

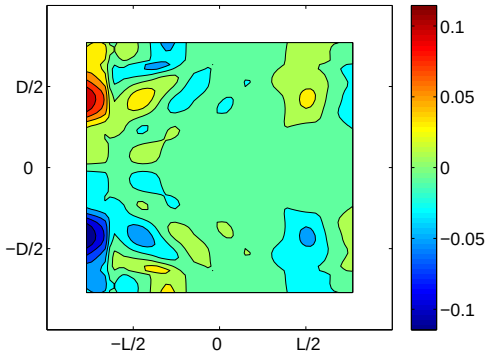

(d) $\sigma_{22}^h(\boldsymbol{x})$

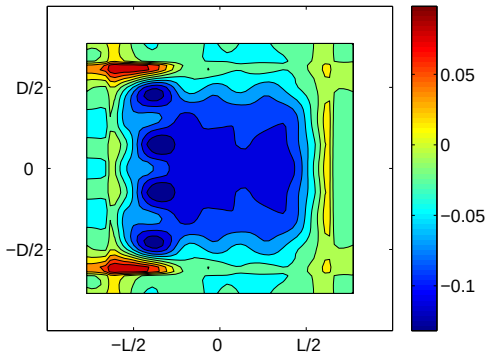

(e) $\sigma_{12}^h(\boldsymbol{x})$

Figure 4.5: Displacement and stress in the cantilever beam for a regular nodal distribution, found with the EFG method comprising the original material distribution.

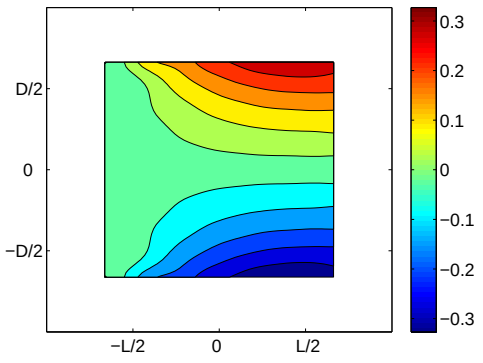

(a) $u_1^h(\boldsymbol{x})$

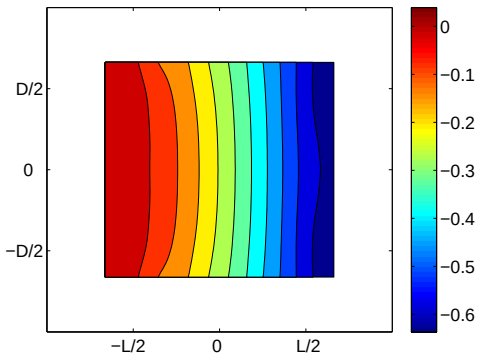

(b) $u_2^h(\boldsymbol{x})$

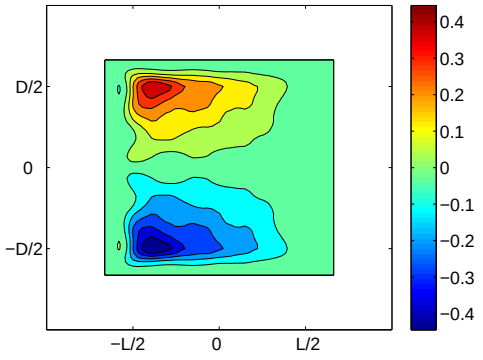

(c) $\sigma_{11}^h(\boldsymbol{x})$

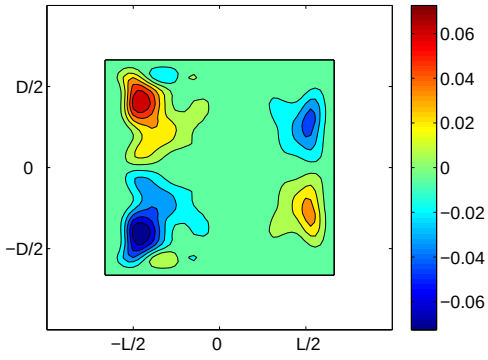

(d) $\sigma_{22}^h(\boldsymbol{x})$

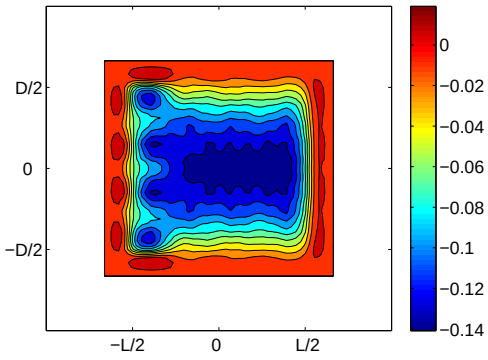

(e) $\sigma_{12}^h(\boldsymbol{x})$

Figure 4.6: Displacement and stress in the cantilever beam for a regular nodal distribution, found with the EFG method comprising the nodal compaction material distribution.

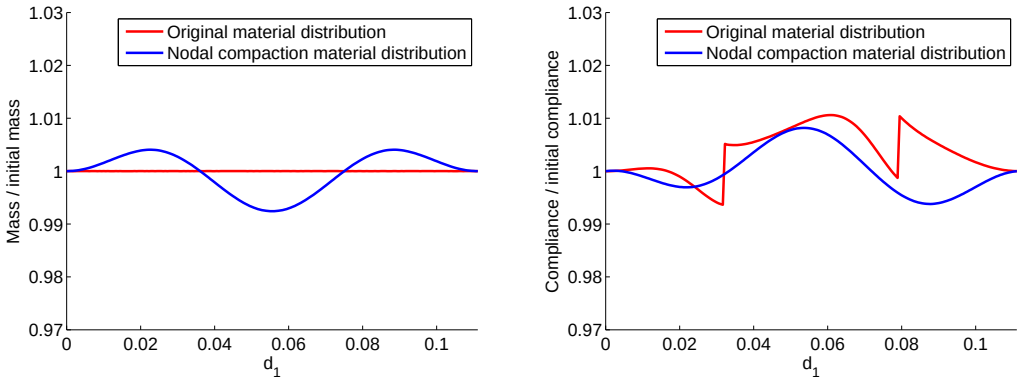

(a) $0 \leq d_1 \leq dm_1$, $d_2 = 0$ and $\beta = 0$

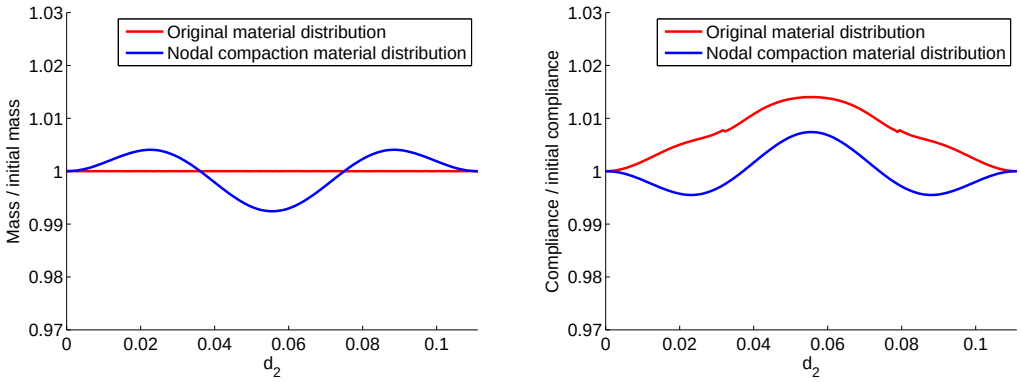

(b) $d_1 = 0$, $0 \leq d_2 \leq dm_2$ and $\beta = 0$

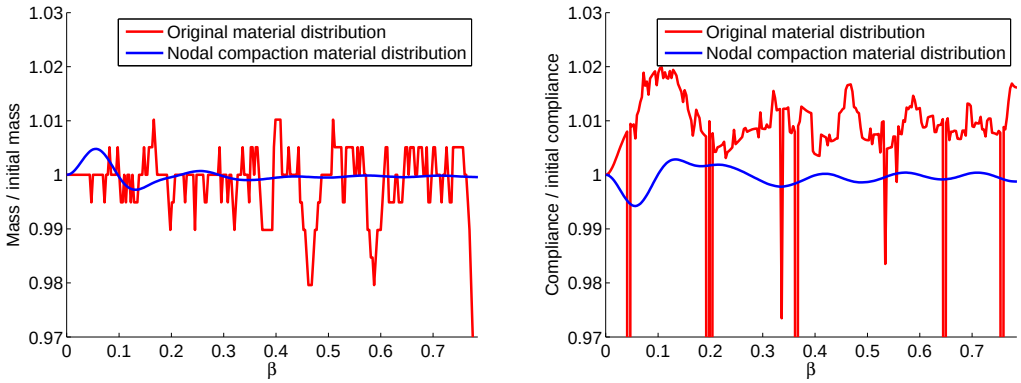

(c) $d_1 = 0$, $d_2 = 0$ and $0 \leq \beta \leq \pi/4$

Figure 4.7: Mass and compliance of the cantilever beam for various positions of the background mesh relative to the nodal distribution. The background mesh is translated by d_1 and d_2 and rotated by β according to Fig. 4.3.

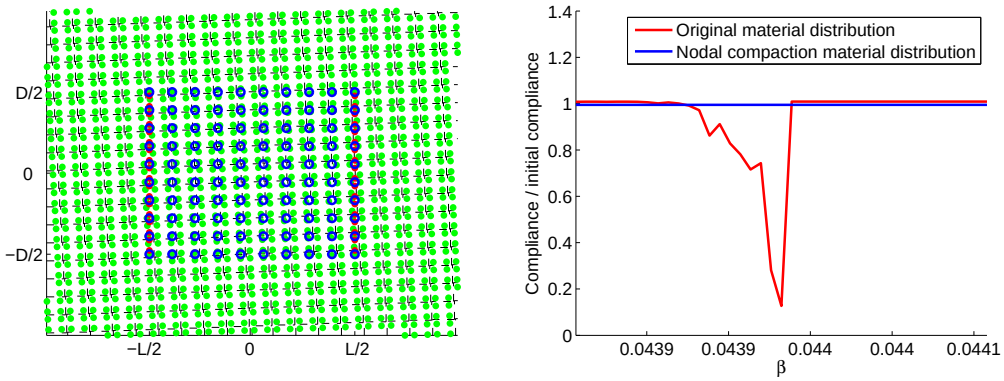

(a) Background mesh and nodes for $\beta = 7/500\pi$ (b) Compliance for $6.98/500\pi \leq \beta \leq 7.02/500\pi$

Figure 4.8: Closeup of the artificial stiffening in the cantilever beam problem (Fig. 4.3), occurring for specific background mesh angles β.

In contrast, the nodal compaction material distribution does not show these discontinuities in the mass and the compliance, as shown in Fig. 4.7. However, both quantities are slightly affected (changes in the mass and compliance less than 1%) by the position and angle of the background mesh.

Furthermore, for some angles of the background mesh the original material distribution shows an unexpected effect. The compliance decreases drastically while maintaining approximately the same mass. For instance, for $\beta = 7/500\pi$ compared to $\beta = 0$ the compliance decreases more than five times. To determine the origins of this effect, the background mesh and nodal configuration for $\beta = 7/500\pi$ are shown in Fig. 4.8a. It appears that for this angle a diagonal alignment exists between the integration points and the nodes. This alignment introduces an artificial numerical increase in stiffness. Fig. 4.8b shows that the decrease in compliance occurs for more angles around $\beta = 7/500\pi$, however the range is relatively small. For these problematic angles, the nodal compaction material distribution does not show any artificial stiffening.

The results obtained for the considered exemplary problem show that the discontinuities occurring in the EFG method comprising the original material distribution are circumvented by use of the nodal compaction material distribution. Furthermore, the unexpected stiffening effect does not occur in the nodal compaction material distribution, which probably results from the smooth description of the density. Therefore, the nodal compaction material distribution is better suited for the description of complexly shaped structures. However, the influence of the regularity of the nodal distribution should also be investigated to substantiate this argument.

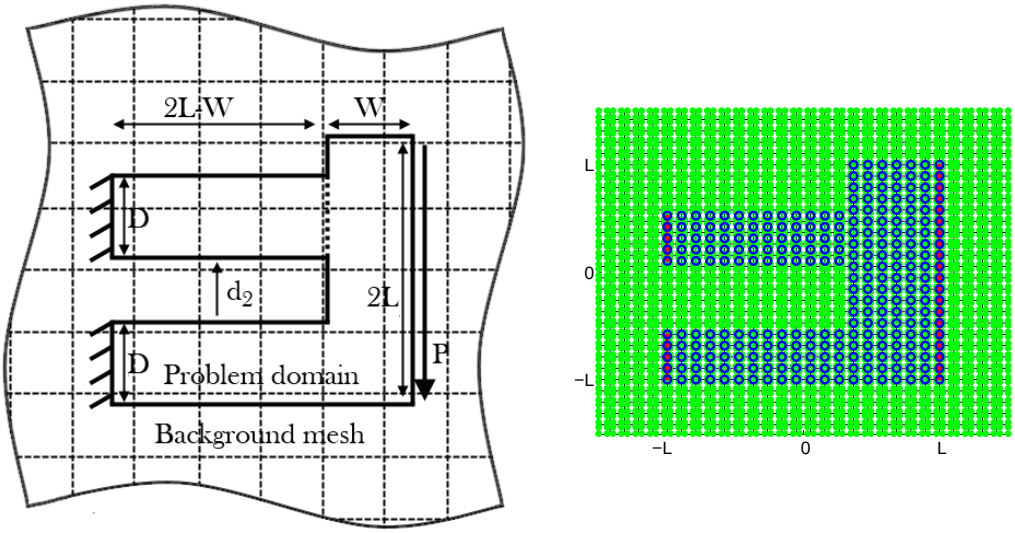

(a) Model (b) Discretization

Figure 4.9: Problem domain and background mesh of the exemplary problem used for the exploration of the effects occurring when displacing the nodes relative to each other. The discretization of the problem domain is done by nodes (blue circles) and integration points (green and red dots).

4.2.3 Relative displacement of nodes

The previous section investigated the effect of the position of the background mesh relative to the nodal distribution. Another influence on the solution accuracy can come from the position of the nodes relative to each other. In Sec. 3.1 the effect of the nodal distribution on the accuracy of the EFG method has been investigated. It has been shown that the nodal distribution can influence the solution without changing the material distribution. In contrast, when using the nodal compaction material distribution in the EFG method, the shape of the material is directly related to the nodal distribution. To deepen the understanding of this relation, this section investigates the influence of altering the regular nodal distribution.

The exploration is performed based on the exemplary problem shown in Fig. 4.9. The problem domain is fixed on the left edge and loaded with a downward traction P on the right edge. By varying d_2, the two parts of the problem domain on the left side can be separated, creating a variation in the material distribution. The discretization parameters are given in Tab. 4.2 and the model constants are $D = 5dn_2$, $W = 7dn_1$, $L = 2$, $E = 1$ and $\nu = 0.3$. Fig. 4.9b shows the discretization of the problem domain. Similarly to previous section, the results of the exemplary problem are the compliance and mass. These two quantities are normalized by the compliance and mass of the initial configuration ($d_2 = 0$), given

Table 4.2: EFG method parameters.

Number of nodes	$n = 270$
Influence domain shape	rectangular
Average nodal distance in x_1 direction	$dn_1 = 2/19$
Average nodal distance in x_2 direction	$dn_2 = 2/19$
Local influence domain size	$d = 3.5$
Density influence domain size	$d^\rho = 1.5$
Nodal mass per node	$m^I = dn_1 dn_2$
Size of monomial basis	2 (linear)
Size background cell in x_1 direction	$dm_1 = dn_1$
Size background mesh in x_2 direction	$dm_2 = dn_2$
Integration points per cell	4
Number of boundary cells along left edge	8
Number of boundary cells along right edge	19

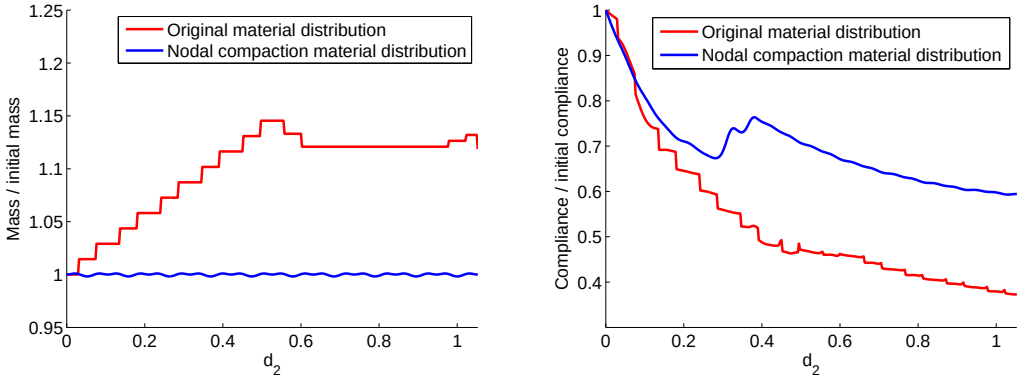

Figure 4.10: Mass and compliance for various nodal displacements for the problem as depicted in Fig. 4.3. In order to achieve the separation of the material domains, part of nodes is moved up by a value of d_2.

by $m_{tot} = 4.95$ and $C = 0.65$ for the original material distribution and $m_{tot} = 2.99$ and $C = 1.32$ for the nodal compaction material distribution.

Next, the normalized mass and compliance are obtained for $0 \leq d_2 \leq 20/19$, shown in Fig. 4.10.[5] Besides the initial disparity in mass between both material distributions, the original material distribution shows an increase in total mass when the two parts are separated. For the same material distribution, moving part of the nodes upwards results in a stiffer structure. Moreover, additional stiffening of the structure results form the increase in mass. This stiffening occurs discontinuous, resulting from the discontinuity in the original material distribution.

[5]For both material distributions, the displacement and stress for $d_2 = 0, 5/19, 10/19, 20/19$ are shown in App. B in Fig. B.5, Fig. B.6, Fig. B.7 and Fig. B.8, respectively.

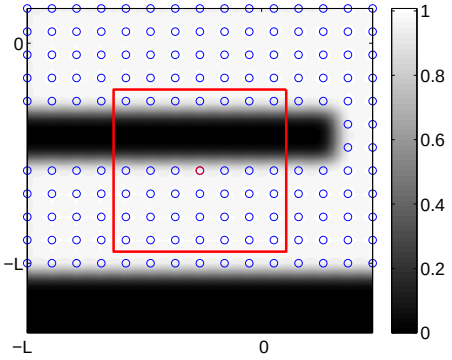

Figure 4.11: Density distribution (grey contour) near the boundaries of the separated material domains. The influence domain (red line) of a node (red circle) close to the gap reaches over the zero density area, resulting in a coupling between separate parts of the structure.

In contrast to the original material distribution, the mass and compliance for the nodal compaction material distribution behave continuously. Only slight oscillations appear in the mass, thus the total mass is approximately conserved. Moreover, the compliance increases for $0.3 < d_2 < 0.4$. In principle, this increase should not occur, since separation of the two parts results in a stiffer structure. The behavior of the compliance can be explained by considering a nodal influence domain of a node close to the created gap, as shown in Fig. 4.11. The nodal influence domain reaches over the region with zero density, resulting in a coupling between the material on both sides of the gap. Thus, the two parts of the structure are not detached as the density suggests.

A possible solution to this problem is to use $d^\rho = d$. As a consequence, the nodal influence domain d will never cover a region with zero density. For an accurate solution, d should be chosen relatively large. Therefore, d^ρ also becomes relatively large, resulting in very smooth density distributions with large intermediate density areas near the outer nodes (Fig. 4.1). Moreover, when choosing $d^\rho = d$, only a constant monomial basis can be used to prevent matrix $\boldsymbol{A}$ in the MLS approximation from becoming singular. This constant monomial basis reduces the accuracy of the solution.

To determine the effect of using $d^\rho = d$ and a constant monomial basis, the mass and compliance are shown in Fig. 4.12. In the same figure, the mass and compliance are shown when using $d^\rho = 1.5$, $d = 3.5$ and a linear monomial basis. The increase in compliance does not exist when $d^\rho = d$. Some small oscillations are still present in the compliance, probably resulting from a relative change in position of the background mesh to the nodal distribution. Moreover, the oscillation in the total mass is smaller for $d^\rho = d$, since the density distribution

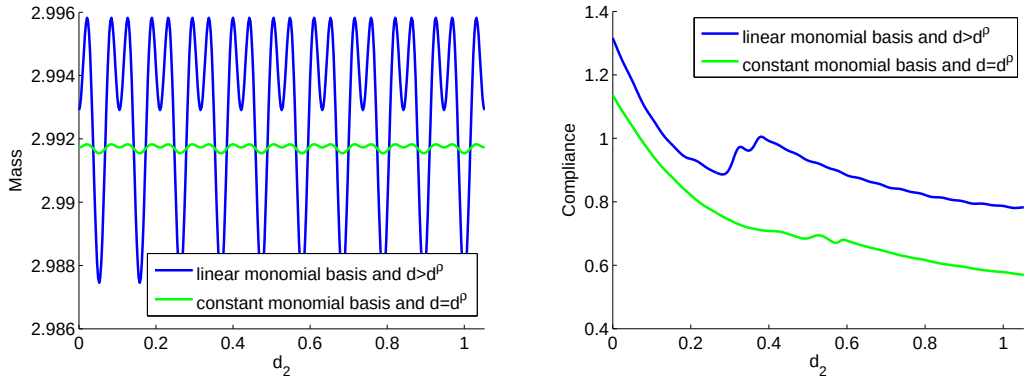

Figure 4.12: Mass and compliance for various displacements of the nodal distributions as depicted in Fig. 4.3. In order to achieve a separation between two material domains, part of the nodes is moved up by a value of d_2.

is smoother and thus integration of the density becomes easier.

4.3 Compliance sensitivity

In Sec. 4.2.3 the performance and characteristics of the EFG method comprising the nodal compaction material distribution have been investigated. From various exemplary problems the quality of the solutions has been compared to the original material distribution. In general, the nodal compaction material distribution showed favorable characteristics. For instance, this distribution circumvented discontinuities in the material distribution. Furthermore, at coordinates with few neighboring nodes the density is decreased, removing the erratic stress peaks in these areas. However, these tests have been performed on regular distributed nodal distributions. Therefore these tests do not include the influence of irregular nodal distributions on the EFG accuracy, which proved to be a problem in the original material distribution (Sec. 3.1).This section investigates the influence of the nodal position on the EFG accuracy.

Displacing the nodes in the nodal compaction material distribution affects the EFG solution in two ways. First, as was shown in Sec. 3.1 the nodal position influences the quality of the discretization. This is an unfavorable effect, since previous analysis showed that irregular nodal distributions decrease the accuracy of the solution. Second, the nodal position influences the shape, since the density depends on the nodal position. Repeating the random nodal distribution tests from Sec. 3.1.1 will not clearly demonstrate the separate contributions of both effects. Instead, a different approach to determine the influence of the nodal position is used in this section.

So far, the global behavior of the structure has been expressed by the compliance. By determining the derivative of the compliance to the nodal position (hereafter: compliance sensitivity), the influence of nodal displacements on the compliance is found. The compliance sensitivity can be expressed as

$$\frac{\partial C}{\partial x_i^I} \quad \text{or} \quad C_{,Ii}, \tag{4.4}$$

where C is the compliance, x_i^I is the coordinate of node I in direction i, $I = 1...n$ and $i = 1, 2$ in two dimensions. From the compliance sensitivity it can be determined that the dependency of the solution is due to changes in the shape or due to the quality of the discretization. Determining the separate contributions of both effects can be done by calculating the compliance sensitivity with two methods. First, in Sec. 4.3.1 the compliance sensitivity is determined by the Finite Differences method [20]. With this method, the compliance sensitivity consists of both the contributions from the change in shape and the quality of the discretization. For this method, the original and nodal compaction material distribution are compared. Second, in Sec. 4.3.2 the compliance sensitivity is determined analytically, in which the contribution of the discretization quality is neglected. This compliance sensitivity then only represents the effect of the nodal position on the shape. Only the nodal compaction material distribution is considered for this method, since the material density in the original material distribution is constant.

For the two methods, an exemplary problem is used to quantify the compliance sensitivity. The problem domain and background mesh for this exemplary problem are shown in Fig. 4.13a. The model constants are $D = 1$, $L = 1$, $E = 1$ and $\nu = 0.3$. The left edge of the problem domain is fixed and the center part of the right edge with length $1/5D$ is loaded with a downward traction. The parameters used for the discretization are given in Tab. 4.3, and the corresponding discretization is shown in Fig. 4.13b.

4.3.1 Finite Difference compliance sensitivity

In order to determine the compliance sensitivity $C_{,Ii}$ numerically, the Finite Difference method can be applied:

$$\frac{\partial C}{\partial x_i^I} = \frac{C(x_i^I + d_i) - C}{d_i}, \tag{4.5}$$

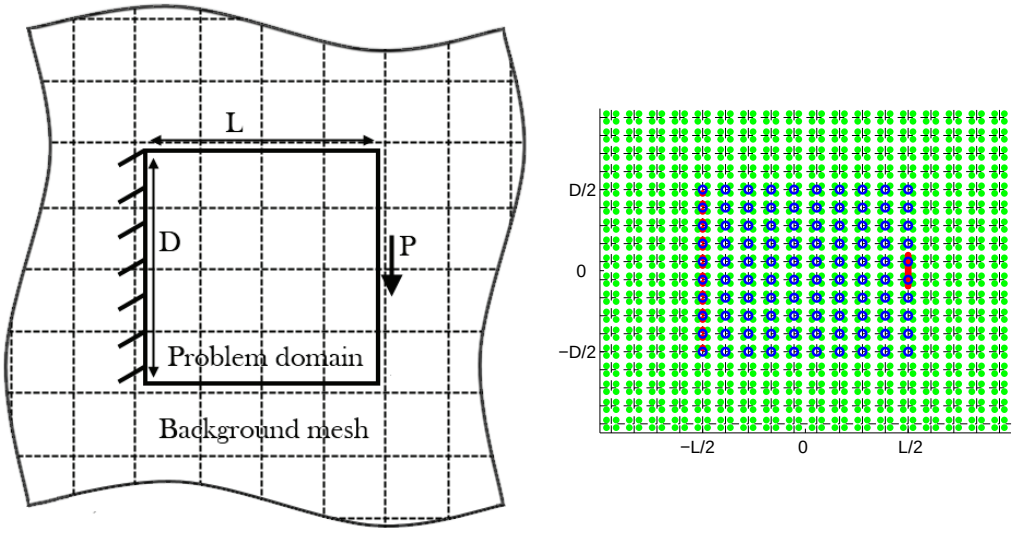

(a) Model (b) Discretization

Figure 4.13: Problem domain and background mesh of the exemplary problem used for quantifying the compliance sensitivity. The discretization of the problem domain is done by nodes (blue circles) and integration points (green and red dots).

Table 4.3: EFG method parameters.

Number of nodes in x_1 direction	$n_1 = 10$
Number of nodes in x_2 direction	$n_2 = 10$
Influence domain shape	rectangular
Average nodal distance in x_1 direction	$dn_1 = L/(n_1 - 1)$
Average nodal distance in x_2 direction	$dn_2 = D/(n_2 - 1)$
Local influence domain size	$d = 3.5$
Density influence domain size	$d^\rho = 3.5$
Nodal mass per node	$m^I = dn_1 dn_2$
Size of monomial basis	1 (constant)
Size background cell in x_1 direction	$dm_1 = dn_1$
Size background mesh in x_2 direction	$dm_2 = dn_2$
Integration points per cell	4
Number of boundary cells along left edge	9
Number of boundary cells along right edge	9

in which $C(x_i^I + d_i)$ is the compliance for a displacement d_i of node I and d_i is the step size in direction x_i.[6] For each node in the discretization of the problem domain in Fig. 4.13b, the compliance sensitivity is determined in the x_1 and x_2 direction. Since each node has a influence on the compliance in the x_1 and x_2 direction, the compliance sensitivity can be visualized by a vector plot. The compliance sensitivity is shown by this vector plot in Fig. 4.14 for the original and nodal compaction material distribution. The green lines in the vector plot start at the corresponding nodal coordinate and point in the direction of decreasing compliance.[7]

The vector plots show that for both material distributions the direction of the vectors of the outer nodes oscillates. Moreover, the compliance is more sensitive to changes in the nodal positions along the boundary than internally. However, for the nodal compaction material distribution, the sensitivity along the boundary is much smaller and the internal compliance sensitivity is much larger than for the original material distribution. This last difference is more clearly shown for the central sixteen nodes in Fig. 4.14c and Fig. 4.14d.

The dissimilarities between the compliance sensitivity of the original and nodal compaction material distribution are caused by the differences in density. The magnitude of the compliance sensitivity in the original material distribution purely results from a change in the discretization. For the nodal compaction material distribution the nodal positions both influence the quality of the discretization and the material density. Thus, the introduction of a material density depending on the nodal compaction results in a compliance which is sensitive to the shape of the structure. However, some numerical artifacts still result in oscillations of the compliance sensitivity. To isolate the contribution of the nodal position on the material density, next section discusses an analytical approach for the compliance sensitivity.

4.3.2 Analytical compliance sensitivity

The compliance sensitivity to the shape of the structure can be determined by merely considering the influence of the nodal position on the density distribution. However, this investigation can not be performed with the numerical Finite Differences method used in previous section. In order to remove the compliance sensitivity due to the discretization quality, the nodal sensitivity of the density

[6] The magnitude of the step size is determined from a convergence study with various sizes of d_i. For the example from Fig. 4.13 a value of $d_i = dn_i/1000$ is used.

[7] In the vector plot, the magnitude of the vectors are scaled by a factor s to improve the visibility.

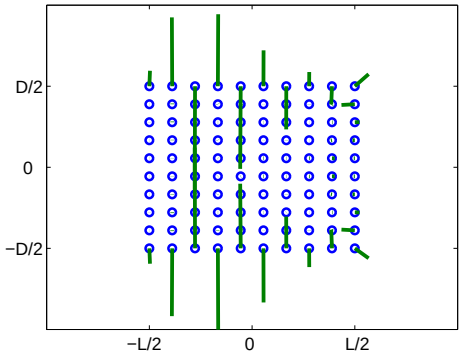

(a) Original material distribution $s = 70$

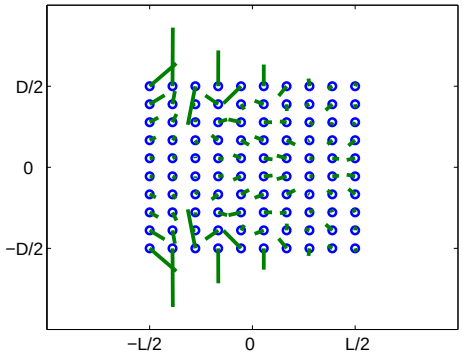

(b) Nodal compaction material distribution $s = 350$

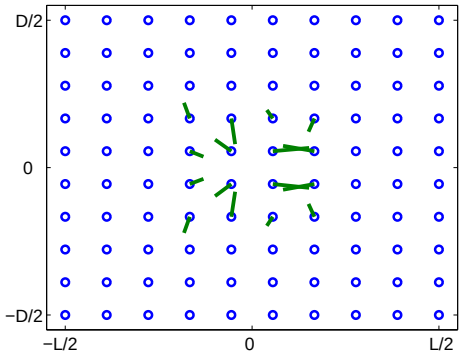

(c) Original material distribution $s = 3000$

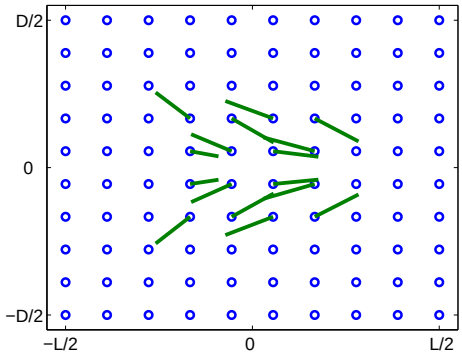

(d) Nodal compaction material distribution $s = 1000$

Figure 4.14: Vector plot of the compliance sensitivity for changes in the nodal positions. The green lines in the vector plot start at the corresponding nodal coordinate and point in the direction of decreasing compliance. To improve visibility the magnitude of the vectors are scaled by a factor s.

distribution is derived analytically. In this derivation the influence of the nodal position on the discretization quality is neglected. The derivation is given next, followed by the results obtained with this method for the exemplary problem in Fig. 4.13.

The compliance is given by

$$C = \boldsymbol{F}^{\mathrm{T}} \hat{\boldsymbol{U}}^h. \tag{4.6}$$

The nodal position sensitivity is then

$$\frac{\partial C}{\partial x_i^I} = \frac{\partial \boldsymbol{F}^{\mathrm{T}}}{\partial x_i^I} \hat{\boldsymbol{U}}^h + \boldsymbol{F}^{\mathrm{T}} \frac{\partial \hat{\boldsymbol{U}}^h}{\partial x_i^I}. \tag{4.7}$$

Since the force vector $\boldsymbol{F}$ does not depend on the material density, its derivative is neglected:

$$\frac{\partial C}{\partial x_i^I} = \boldsymbol{F}^{\mathrm{T}} \frac{\partial \hat{\boldsymbol{U}}^h}{\partial x_i^I} = \{\hat{\boldsymbol{U}}^h\}^{\mathrm{T}} \boldsymbol{K}^{\mathrm{T}} \frac{\partial \hat{\boldsymbol{U}}^h}{\partial x_i^I}. \tag{4.8}$$

The stiffness matrix $\boldsymbol{K}$ can be written as a sum of all the integration point contributions according to

$$\boldsymbol{K} = \sum_{K=1}^{n_i} \rho(\boldsymbol{x}^K) \boldsymbol{K}_e^K, \tag{4.9}$$

in which

$$\boldsymbol{K}_e^K = \sum_{I=1}^{n} \sum_{J=1}^{n} \left[\boldsymbol{B}^I\right]^{\mathrm{T}} \boldsymbol{D} \boldsymbol{B}^J J^K, \tag{4.10}$$

n_i is the number of integration points and J^K is a constant belonging to the integration point. Here, the Young's Modulus has been replaced with a Young's modulus depending on the nodal position (Eq.4.3). Eq. 4.8 then becomes

$$\frac{\partial C}{\partial x_i^I} = \{\hat{\boldsymbol{U}}^h\}^{\mathrm{T}} \sum_{K=1}^{n_i} \rho(\boldsymbol{x}^K) \{\boldsymbol{K}_e^K\}^{\mathrm{T}} \frac{\partial \hat{\boldsymbol{U}}^h}{\partial x_i^I}. \tag{4.11}$$

In order to determine the derivative of the displacement vector $\hat{\boldsymbol{U}}^h$ consider

$$\boldsymbol{K} \hat{\boldsymbol{U}}^h = \boldsymbol{F}, \tag{4.12}$$

for which the following derivative holds:

$$\frac{\partial \boldsymbol{K}}{\partial x_i^I} \hat{\boldsymbol{U}}^h + \boldsymbol{K} \frac{\partial \hat{\boldsymbol{U}}^h}{\partial x_i^I} = \frac{\partial \boldsymbol{F}}{\partial x_i^I} = 0, \tag{4.13}$$

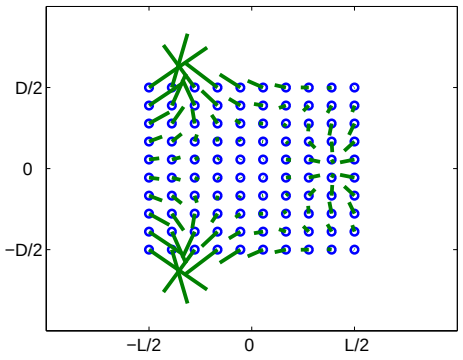

Figure 4.15: The compliance sensitivities for the original material distribution when only taking into account the influence of the nodal position on the density distribution. The green lines in the vector plot start at the corresponding nodal coordinate and point in the direction of decreasing compliance. The vectors are scaled according to $s = 1000$.

or

$$\frac{\partial\{\sum_{K=1}^{n_i}\rho(\boldsymbol{x}^K)\boldsymbol{K}_e^K\}}{\partial x_i^I}\hat{\boldsymbol{U}}^h + \sum_{K=1}^{n_i}\rho(\boldsymbol{x}^K)\boldsymbol{K}_e^K\frac{\partial\hat{\boldsymbol{U}}^h}{\partial x_i^I} = 0. \tag{4.14}$$

The stiffness matrix K_e^K is independent of the density and is therefore neglected:

$$\frac{\partial\{\sum_{K=1}^{n_i}\rho(\boldsymbol{x}^K)\}}{\partial x_i^I}\hat{\boldsymbol{U}}^h + \sum_{K=1}^{n_i}\rho(\boldsymbol{x}^K)\frac{\partial\hat{\boldsymbol{U}}^h}{\partial x_i^I} = 0, \tag{4.15}$$

or

$$\frac{\partial\hat{\boldsymbol{U}}^h}{\partial x_i^I} = -\sum_{K=1}^{n_i}\frac{\frac{\partial\{\rho(\boldsymbol{x}^K)\}}{\partial x_i^I}}{\rho(\boldsymbol{x}^K)}\hat{\boldsymbol{U}}^h. \tag{4.16}$$

Combining Eq. 4.16 and Eq. 4.11 results in the compliance sensitivity with only the contribution due to influence of the nodal position on the shape:

$$\frac{\partial C}{\partial x_i^I} = -\{\hat{\boldsymbol{U}}^h\}^{\mathrm{T}}\sum_{K=1}^{n_i}\left[\boldsymbol{K}_e^K\right]^{\mathrm{T}}\frac{\partial\rho(\boldsymbol{x}^K)}{\partial x_i^I}\hat{\boldsymbol{U}}^h, \tag{4.17}$$

in which

$$\frac{\partial\rho(\boldsymbol{x}^K)}{\partial x_i^I} = \sum_{J=1}^{n}\frac{\partial W(\boldsymbol{x}^K - \boldsymbol{x}^{\boldsymbol{J}}, d^\rho)}{\partial x_i^I}m^J. \tag{4.18}$$

For each node used to discretize the problem domain in Fig. 4.13a, the compliance sensitivity is determined in the x_1 and x_2 direction. The compliance sensitivity is shown by a vector plot in Fig. 4.15. No oscillations are present in the sensitivity. Actually, these results have a relevant physical significance. The

sensitivity vectors point in the direction of decreasing compliance. Comparing these results to the results of previous section (Sec. 4.3.1) relativizes the contributions to the compliance sensitivity. Thus showing the major influence of the discretization on the solution accuracy.

4.4 Nodal compaction material distribution in the MNA

In this chapter the nodal compaction material distribution has been introduced to resolve some problems with the original material distribution. These problems are mainly caused by the discontinuous material distribution, arising from the interaction between the nodal influence domains and the background mesh. Since the material distribution in the nodal compaction material distribution is continuous, the quality of the EFG solution for complexly shaped structures is increased. This improvement is a prerequisite for the MNA in topology optimization to function. With the nodal compaction material distribution the shape is directly related to the nodal distribution. The nodal positions can then be used as the design variables in topology optimization to alter the layout.

The relation between the nodal position and the shape also results in a compliance sensitivity that depends on the material distribution. This sensitivity can be used to direct the nodes towards a decrease in compliance. However, the compliance sensitivity also depends on the quality of the discretization. According to this dependency the accuracy of the EFG method is lower for irregular nodal distributions. Therefore, the possibility of node redistribution is limited. When neglecting the contribution of the discretization quality on the compliance sensitivity, the resulting sensitivity only depends on the shape of the structure. This compliance sensitivity behaves predictable and can therefore be used to direct the nodes towards the optimal shape. An additional requirement for the nodal positions is necessary in order to take advantage of this predictable compliance sensitivity. This requirement should result in regular nodal distributions during the optimization process to maintain the quality of the discretization. .

To take advantage of the predictable compliance sensitivity the following requirement should hold:

The nodes should remain regularly spaced.

Furthermore, although the introduction of the nodal compaction material distri-

bution improved the possibility for the description of complexly shaped domains, for these shapes the large nodal influence domain can cause additional coupling between separated structural parts. In the MNA this additional coupling can result in artificial stiffening and therefore introduces non-physical coupling between the nodes. Therefore, the large nodal influence domains could affect the convergence to the real optimal structural layout in the MNA. However, the full effects of the nodal influence domains could best be explored in a topology optimization setting.

Chapter 5

The MNA in topology optimization

Recapitulating the previous two chapters, in Chap. 3 the influence of the nodal position on the accuracy of the EFG discretization has been investigated. The most accurate results were obtained with regular nodal distributions. Moreover, the capability of the EFG method to discretize irregular shaped structures proved to be difficult. One difficulty is the presence of discontinuities in the material distribution caused by the interaction between the background mesh and the nodal distribution. Because of these difficulties, the nodal positions in this original material distribution are not suitable as design variables in topology optimization. In Chap. 4 the nodal compaction material distribution has been introduced to improve the capability of the EFG method to discretize irregular shaped structures and to remove the discontinuities present in the solution. In this material distribution the density depends on the nodal compaction, resulting in a material distribution which is sensitive to the nodal positions.

The above-mentioned changes to the EFG method create opportunities for a flow-inspired topology optimization method. This chapter explores the possibilities of such an approach in topology optimization by using the nodal positions as design variables. In order to determine the full potential of the MNA in topology optimization, it would be ideal to explore and test its workings thoroughly. Nevertheless, for a first exploration of the potential of the MNA a basic but effective research suffices. Therefore, the research performed in this chapter comprises the proposition and testing of a fairly simple MNA algorithm. Based on the previous chapters, Sec. 5.1 proposes an MNA optimization algorithm, which includes three additional requirements. The optimization algorithm is tested by three exemplary problems in Sec. 5.2. With these findings, the characteristics and opportunities

of the MNA are discussed in Sec. 5.3.

5.1 An MNA topology optimization algorithm

In order to investigate the characteristics of the MNA in topology optimization, a transparent MNA optimization algorithm is proposed in this section. This algorithm is based on the meshless EFG method (see Chap. 2). Furthermore, some previously discussed difficulties in the original EFG method formulation are reduced by using the nodal compaction material distribution (see Chap. 4).

The quality of the structure can be expressed by the compliance. By changing the shape of the structure, the compliance of the structure can be altered. The optimal layout of the structure is defined as the layout with the lowest compliance. In order to determine additional requirements for the MNA in topology optimization, a discussion on general characteristics of such an approach follows.

In the MNA the shape of the structure is altered by changing the position of mass containing nodes. Since the mass is constant for each node, the total mass of the structure does not change during the design optimization process. Therefore, the total mass of the structure does not have to be constrained.

An algorithm for the displacement of nodes towards the optimal layout of the structure is introduced in Sec. 5.1.3. In this algorithm, the nodes are displaced in the direction of the compliance sensitivity in order to find the optimal layout. However, Sec. 4.3 showed that compliance sensitivity is affected by the EFG discretization. Moreover, irregular nodal distributions introduce inaccuracies in the EFG formulation. One possible solution to circumvent these problems is to use two types of nodes by decoupling the discretization function (hereafter: discretization nodes) and the mass distribution function (hereafter: mass nodes). The accuracy of the discretization can be preserved by fixating the discretization nodes, while the shape of the structure can be altered by displacing the mass nodes. This decoupling will be applied in the proposed MNA and is therefore further discussed in Sec. 5.1.2.

Since the material density depends only on the nodal compaction, normalized densities can occur with a value higher than one. In practice, these densities are difficult to fabricate and should therefore be avoided. This can be achieved by using an asymptotic function for the density. A typical asymptotic density function is discussed in Sec. 5.1.3.

The combination of these aforementioned elements forms an MNA meshless

method-based topology optimization algorithm. Note that this section is merely concerned with the possibility of such an approach and is not necessarily concerned with determining the best possible MNA topology optimization algorithm. In the remainder of this section the three above-mentioned additional requirements for the MNA in topology optimization are discussed. The requirements are: an algorithm for the nodal movement, decoupling of the discretization and the mass distribution function and the asymptotic density function.

5.1.1 Nodal movement

The first additional requirement for the MNA in topology optimization is an algorithm that provides the nodal movement. In this section a fairly simple and transparent algorithm is proposed. When using the nodal compaction material distribution (see Sec. 4.1), the structural layout is defined by the nodal positions. The layout can be altered by displacing the nodes. When moving the nodes in the direction of the compliance sensitivity (see Sec. 4.3), the compliance will probably decrease. Therefore, each node is accelerated in the direction of the compliance sensitivity. The flow-inspired optimization algorithm can then be described by the following differential equation:

$$\frac{\partial^2 x_i^I(t)}{\partial t^2} - c\frac{\partial x_i^I(t)}{\partial t} = \frac{\partial C(x_i^I(t))}{\partial x_i^I(t)} \quad \text{for} \quad I = 1...n \quad \text{and} \quad i = 1, 2, \tag{5.1}$$

in which t indicates the time and c is a velocity damping constant. This equation can be rewritten as

$$\frac{\partial v_i^I(t)}{\partial t} = cv_i^I(t) + \frac{\partial C(x_i^I(t))}{\partial x_i^I(t)} \quad \text{for} \quad I = 1...n \quad \text{and} \quad i = 1, 2, \tag{5.2}$$

where $v_i^I(t)$ is the velocity of node I in direction x_i, defined by

$$v_i^I(t) = \frac{\partial x_i^I(t)}{\partial t}. \tag{5.3}$$

In order to solve Eq. 5.2, the equation is discretized with the numerical Euler Forward method [20], which results in

$$v_i^I(t^{k+1}) = v_i^I(t^k) + \Delta t\{cv_i^I(t^k) + \frac{\partial C(x_i^I(t^k))}{\partial x_i^I(t^k)}\} \quad \text{for} \quad I = 1...n \quad \text{and} \quad i = 1, 2. \tag{5.4}$$

Here, Δt is the size of the time step, t^k is the current time step and t^{k+1} corresponds to the subsequent time step. The nodal positions after each time step are updated

according to

$$x_i^I(t^{k+1}) = x_i^I(t^k) + \Delta t v_i^I(t^{k+1}) \quad \text{for} \quad I = 1...n \quad \text{and} \quad i = 1, 2. \tag{5.5}$$

The velocity damping constant should be limited to $0 \leq c \leq 1$ in order to avoid divergence of the nodal velocities. Moreover, a damping constant with a value close to one will result in smooth flows and global oscillations in the mass flow. In contrast, low values of the damping constant result in highly adaptive nodal movement and local oscillations in the mass flow. In order to increase the convergence rate of the proposed nodal movement algorithm, the compliance sensitivity can be scaled according to

$$C_{,Ii}^s = \frac{C_{,Ii}}{\sqrt{\{C_{,I1}\}^2 + \{C_{,I2}\}^2}} \quad \text{for} \quad I = 1...n \quad \text{and} \quad i = 1, 2, \tag{5.6}$$

where $C_{,Ii}^s$ is the scaled compliance sensitivity of node I in direction x_i.

5.1.2 Decoupling of discretization and mass distribution functions

The second additional requirement for the MNA in topology optimization is the decoupling of the discretization and mass distribution functions of the nodes. So far, the discretization function and mass distribution function have been performed by the same nodes (hereafter: coupled nodes). In order to maintain the accuracy of the EFG method, the nodes should be regularly spaced. However, since the nodes are displaced in the MNA, irregular nodal distributions are likely to occur. These nodal distributions lower the accuracy of the EFG method.

To circumvent the influence of the nodal positions on the EFG formulation, the discretization function and the mass distribution function can be decoupled by introducing two types of nodes: discretization nodes and mass nodes (hereafter: decoupled nodes). The accuracy of the discretization can be preserved by fixating the discretization nodes, while the shape of the structure can be altered by displacing the mass nodes. Since only the density is affected by the displacement of the mass nodes, the exact compliance sensitivity is given by Eq. 4.17.

For the decoupled nodes, the linear elasticity equations can be solved more precisely for irregular shapes. However, only mass can be distributed in regions that contain discretization nodes. Therefore, the discretization nodes have to cover the complete domain in which material is distributed. In topology optimization, this domain is often referred to as the design space. It is likely that the discretization nodes will cover regions with zero density (regions without mass nodes), resulting

in a singular stiffness matrix. To prevent this singularity, a minimum density is assigned to the complete design space, independent of the presence of mass nodes. The minimum density is introduced in the density from Eq. 4.1 according to

$$\rho(\boldsymbol{x}) = \rho^{min} + \{1 - \rho^{min}\} \sum_{I=1}^{n} m^I W(\boldsymbol{x} - \boldsymbol{x}^I, d^\rho), \tag{5.7}$$

in which ρ^{min} is the minimum density. ρ^{min} should be small enough to reduce the influence of this additional density on the material distribution. However, ρ^{min} should be large enough to avoid a singular stiffness matrix.

Decoupling the two nodal functions could also have negative effects on the EFG discretization. Sec. 4.2.3 discussed problems that have been caused by the relatively large nodal influence domain. These problems are probably aggravated for the decoupled nodes. Discretization nodes will be present in regions with low density (regions without mass nodes), introducing additional coupling between regions separated by a low material density region. This additional coupling will affect the optimization process and thus the final optimized shape. However, since this decoupling provides for an effective manner to reduce the problems arising from irregular nodal distributions, decoupling is still applied in the proposed MNA algorithm.

5.1.3 Asymptotic density function

The final additional requirement for the MNA in topology optimization is the asymptotic density function, which is explained in this section. The material density from Eq. 4.1 depends on the nodal compaction. In this material distribution, the normalized densities can become larger than one in areas with high nodal compaction, resulting in material densities which are difficult to fabricate. An asymptotic function for the density is introduced to limit the maximum normalized density:

$$\rho^{as}(\rho(\boldsymbol{x})) = \frac{a\rho(\boldsymbol{x})}{\{\rho(\boldsymbol{x})\}^b + a}, \tag{5.8}$$

with

$$\frac{\partial \rho^{as}(\rho(\boldsymbol{x}))}{\partial \rho(\boldsymbol{x})} = \frac{a\{1-n\}\{\rho(\boldsymbol{x})\}^b + c^2}{\left[\{\rho(\boldsymbol{x})\}^b + a\right]^2}. \tag{5.9}$$

Here, $\rho^{as}(\rho(\boldsymbol{x}))$ is the asymptotic density function and a and b are constants that define the shape of the asymptotic function.

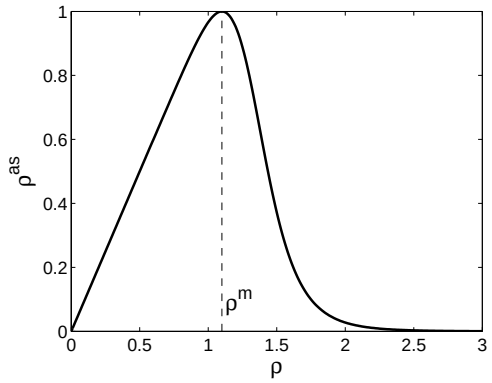

Figure 5.1: The asymptotic density function used in the MNA topology optimization algorithm. This density function is applied in order to limit the value of the normalized material density to one.

The constants a and b are chosen such that

$$\rho^{as}(\rho(\boldsymbol{x}) = \rho^m) = 1 \quad \text{and} \quad \frac{\partial \rho^{as}(\rho(\boldsymbol{x}) = \rho^m)}{\partial \rho(\boldsymbol{x})} = 0, \tag{5.10}$$

where ρ^m is the value of $\rho(\boldsymbol{x})$ for which $\rho^{as}(\rho(\boldsymbol{x}))$ equals one and is at a maximum. The constants can then be expressed in terms of ρ^m according to

$$b = \frac{1}{\rho^m - 1} + 1, \tag{5.11}$$

$$a = \frac{\{\rho^m\}^b}{\rho^m - 1}. \tag{5.12}$$

The asymptotic density function ρ^{as} is shown in Fig. 5.1 for $\rho^m = 1.1$. The compliance sensitivity from Eq. 4.17 changes when using this asymptotic density function. The correct sensitivity can be found by replacing the derivative of the density from Eq. 4.1 by the derivative of the asymptotic density function, which equals

$$\frac{\partial \rho^{as}(\boldsymbol{x}^K)}{\partial x_i^I} = \frac{\partial \rho^{as}(\rho(\boldsymbol{x}^K))}{\partial \rho(\boldsymbol{x}^K)} \frac{\partial \rho(\boldsymbol{x}^K)}{\partial x_i^I}. \tag{5.13}$$

The asymptotic density function provides for an effective method to exclude normalized material densities with a value larger than one. Moreover, no constraints have to be applied to the nodal positions when using this asymptotic function. Therefore, the resulting material description depends continuously on the nodal position. This provides for favorable properties that can be utilized in the MNA.

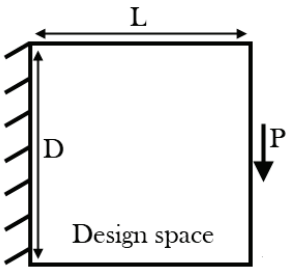

Figure 5.2: Design space and boundary conditions for the topology optimization exemplary problems.

Table 5.1: EFG method parameters.

	Lower res.	Higher res.
Number of cells in x_1 direction	$m_1 = 9L$	$2m_1$
Number of cells in x_2 direction	$m_2 = 9D$	$2m_2$
Number of discretization nodes in x_1 direction	$m_1 + 1$	$2m_1 + 1$
Number of discretization nodes in x_2 direction	$m_2 + 1$	$2m_2 + 1$
Nodal influence domain shape	rectangular	rectangular
Nodal influence domain size d	2.5	2.5
Size of monomial basis	2 (linear)	2 (linear)
Integration points per cell	4	4
Number of boundary cells along left edge	m_2	$2m_2$
Number of boundary cells along right edge	m_2	$2m_2$

5.2 MNA topology optimization exemplary problems

To determine the feasibility of the MNA topology optimization algorithm proposed in Sec. 5.1, the MNA algorithm is used to find the optimal shape of a two-dimensional cantilever beam. The design space of the beam is shown in Fig. 5.2, where the design space is the domain in which material can be distributed. Three design spaces with varying size are considered: $L = 1$ and $D = 2$; $L = 2$ and $D = 1$; $L = 3$ and $D = 1$. The remaining model constants are $E = 1$ and $\nu = 0.3$. Moreover, the left edge of the design space is fixed and on the center part of the right edge with size $1/5D$ a downward traction $P = 0.1$ is applied. The design space is discretized using the parameters from Tab. 5.1.

The initial material distribution in the design space is defined by the positions of the mass node. For the three varying design spaces, mass nodes are distributed in the center region with width L and height $1/3D$. The properties and positions of these mass nodes are given by the parameters in Tab. 5.2. Each node is initially randomly perturbed to avoid unstable optimization paths. Furthermore, the time step equals $\Delta t_0 = L/m_1$, which is small enough to avoid instabilities in

Table 5.2: Initial density distribution parameters

	Lower res.	Higher res.
Number of mass nodes in x_1 dir.	$9L$	$18L$
Number of mass nodes in x_2 dir.	$3D$	$6D$
Initial nodal distance in x_1 dir.	$L/(9L-1)$	$L/(18L-1)$
Initial nodal distance in x_2 dir.	$D/(3D-1)$	$D/(6D-1)$
Influence domain shape	rectangular	rectangular
Local influence domain size d^ρ	1.5	1.5
Nodal mass m^I	$L/(9L-1)D/(3D-1)$	$L/(18L-1))D/(6D-1)$
Minimal density ρ^{min}	10^{-6}	10^{-6}

the nodal movement. The optimized shape will be affected by the detail of the nodal distributions and the background mesh. In order to investigate this effect, two various nodal distribution and background mesh resolutions are considered: a lower resolution and a higher resolution. For the design space with size $L = 1$ and $D = 2$ Fig. 5.3 shows the lower and higher resolution. The total mass m_{tot} varies for the lower and higher resolution. Therefore comparison of the lower and higher resolutions is not straightforward. From the results of the optimization process only general characteristics of the MNA topology optimization method can be observed.

Some density distributions obtained during the optimization process of the design space with size $D = 2$ and $L = 1$ are shown in Fig. 5.4.[1] The density distributions are given for t^k with $k = 1, 25, 50, 100, 200$ for both the lower and higher resolution. The results show that the structure flows to a different layout, finally reaching an equilibrium. Interestingly, the nodes do not leave the design space and remain approximately equally spaced. The total mass of the structure during the optimization process is shown in Fig. 5.5a. In this figure the total mass has been normalized by the sum of the nodal masses ($\sum_{I=1}^{n} m^I$). During the optimization process, the asymptotic density function results in a converging normalized mass towards a value lower than one. The total mass is also reduced when nodes are close to the boundary of the design space, which explains the higher normalized mass of the higher resolution. The compliance of the structure during the optimization process is also shown in Fig. 5.5a. The compliance converges to a value lower than the initial compliance. Assuming that the linear elasticity equations are solved accurately with the EFG method, an improved structure has been found with the MNA.

Similar results are obtained for the structural optimization using the design

[1] For these density distributions the displacement and stress are shown in App. B in Fig. B.9.

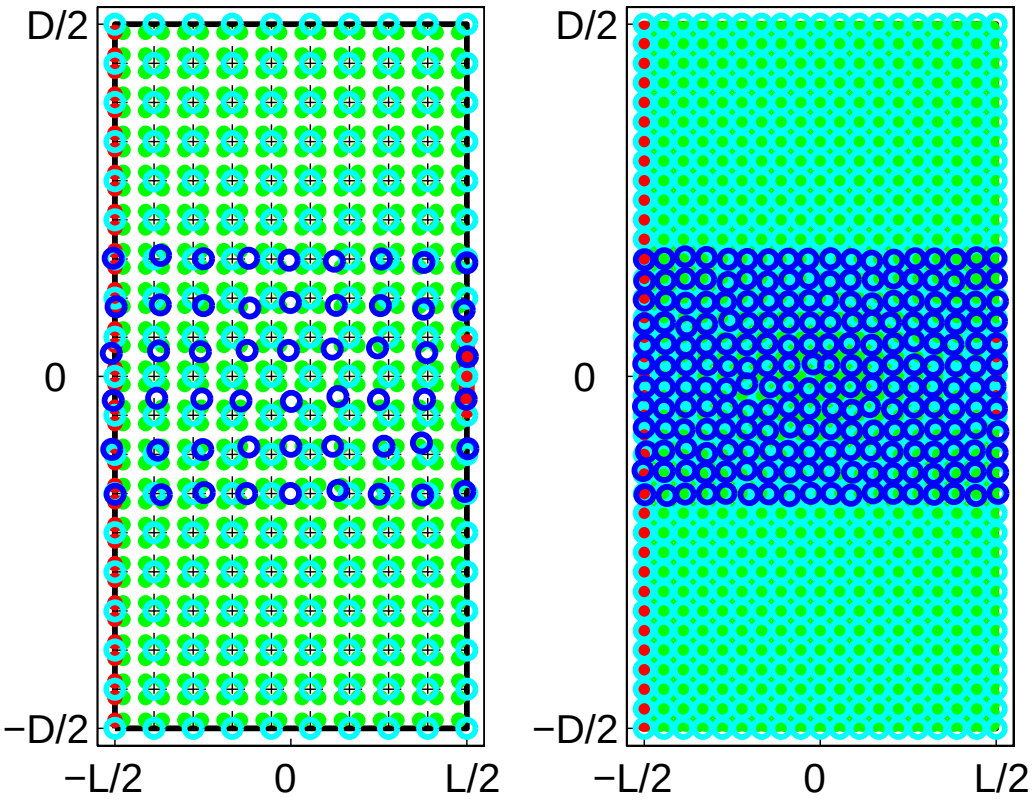

(a) Lower resolution

(b) Higher resolution

Figure 5.3: Mass nodes, discretization nodes, background mesh and boundary integration points for the design space from Fig. 5.2 with $L = 1$ and $D = 2$. The blue circles correspond to the mass nodes, the cyan circles correspond to the discretization nodes, the green dots denote the integration points and the red dots denote the boundary integration points. The specific parameters of the discretization and the initial mass distribution are given in Tab. 5.1 and Tab. 5.2.

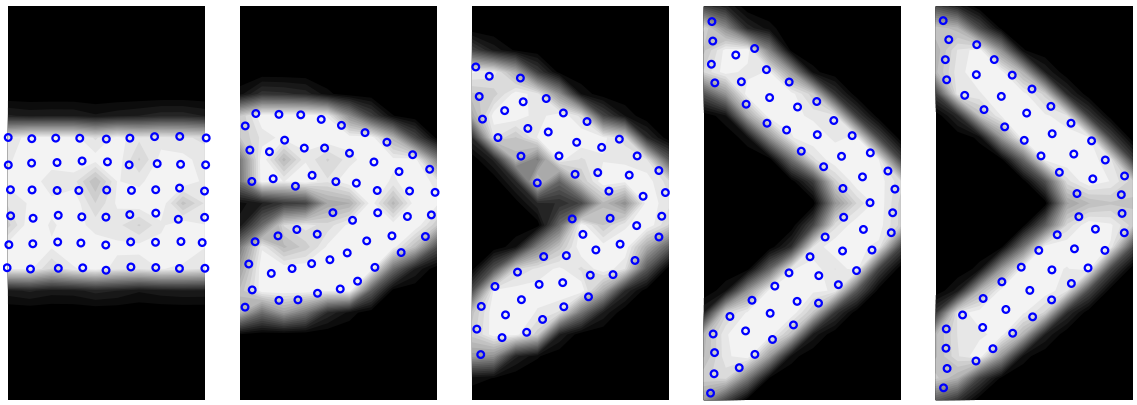

(a) Lower resolution

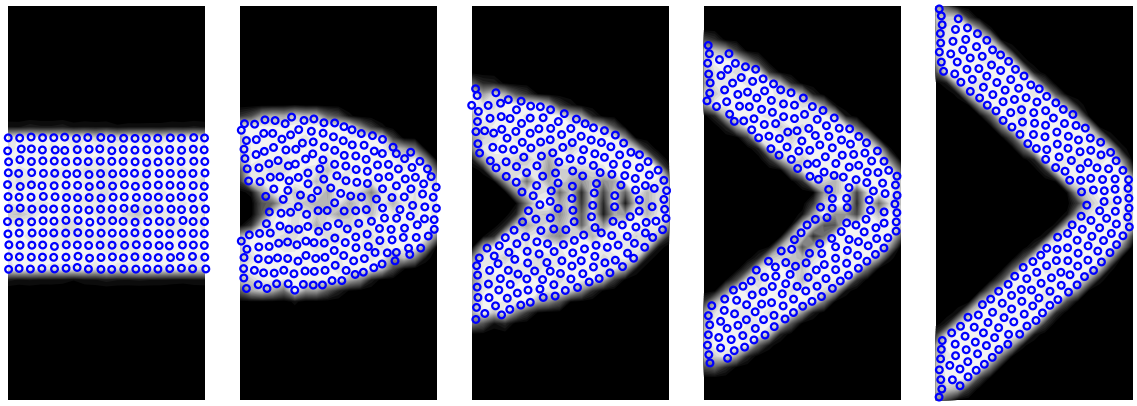

(b) Higher resolution

Figure 5.4: Density distributions during optimization process of a cantilever beam with the design space and boundary conditions as depicted in Fig. 5.2. The size of the design space is equal to $D = 2$ and $L = 1$ and the density distribution is shown at time t^k with $k = 1, 25, 50, 100, 200$. The grey contour corresponds to the density and the blue nodes to the mass nodes. Both a lower and higher resolution for the discretization nodal distribution and the background mesh are considered, given by the parameters from Tab. 5.1 and Tab. 5.2.

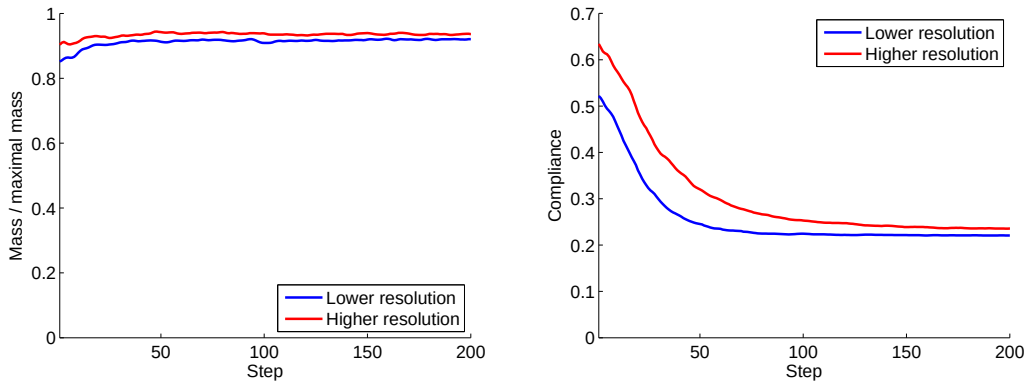

(a) $L = 1$ and $D = 2$

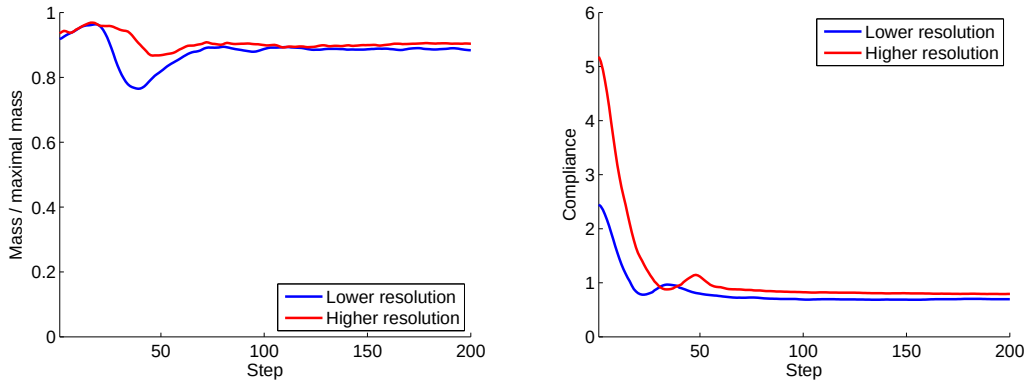

(b) $L = 2$ and $D = 1$

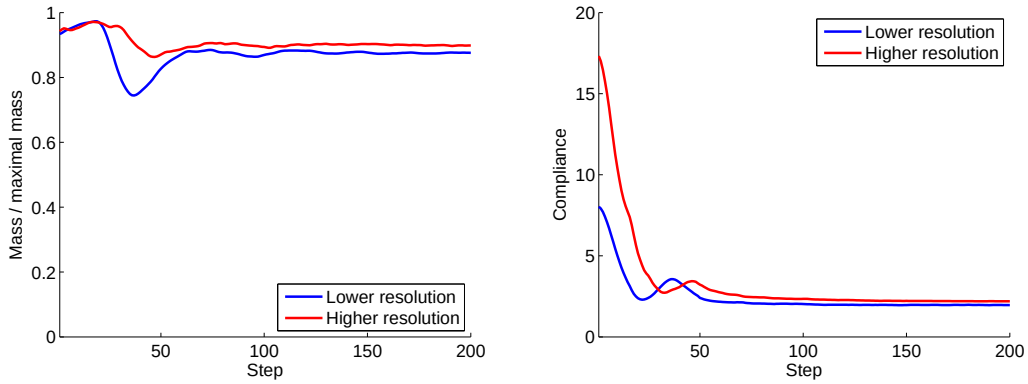

(c) $L = 3$ and $D = 1$

Figure 5.5: Normalized mass and compliance during the optimization of the design space from Fig. 5.2. k corresponds to the time step according to t^k.

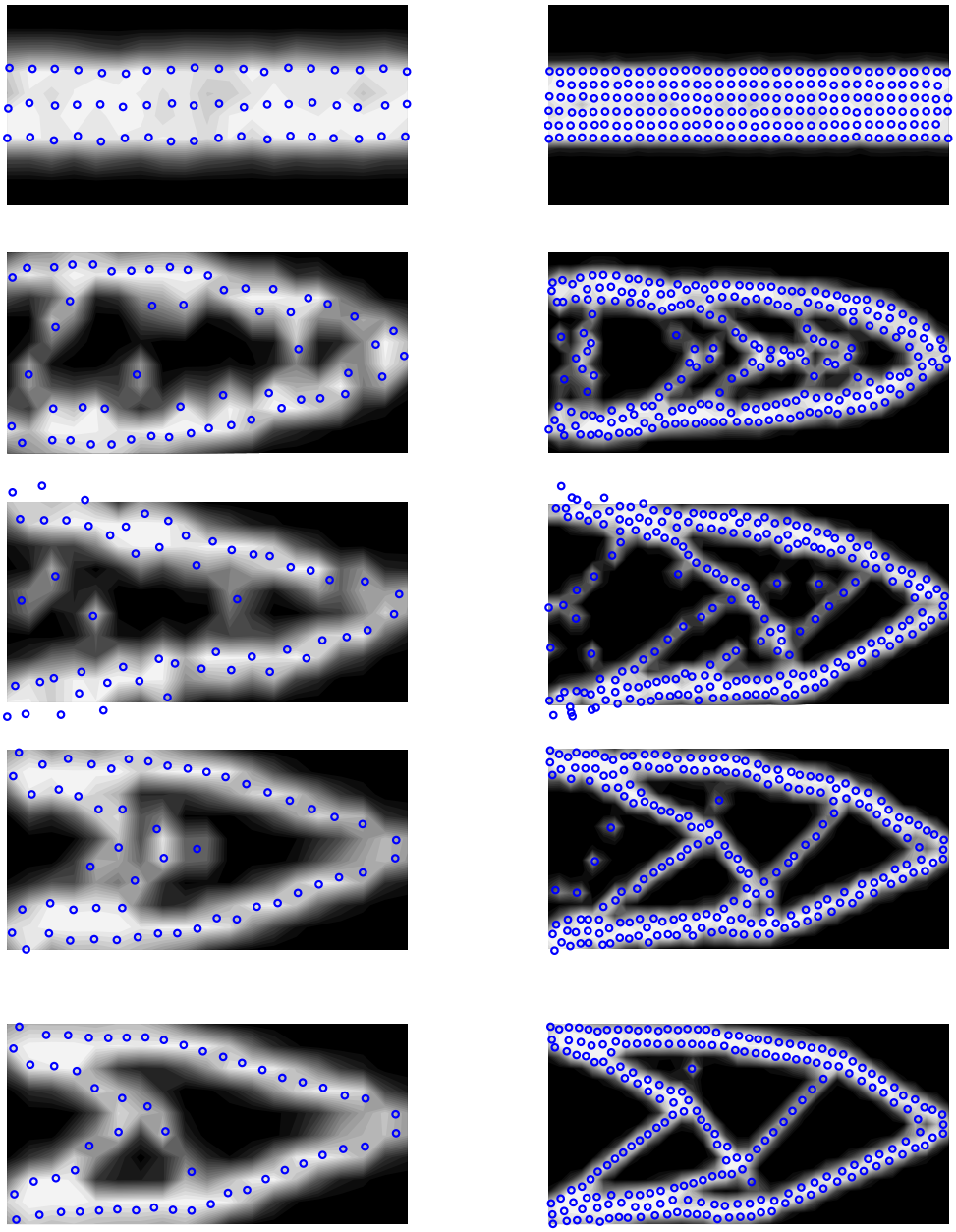

(a) Lower resolution

(b) Higher resolution

Figure 5.6: Density distributions during optimization process of a cantilever beam with the design space and boundary conditions as depicted in Fig. 5.2. The size of the design space is equal to $D = 1$ and $L = 2$ and the density distribution is shown at time t^k with $k = 1, 25, 50, 100, 200$. The grey contour corresponds to the density and the blue nodes to the mass nodes. Both a lower and higher resolution for the discretization nodal distribution and the background mesh are considered, given by the parameters from Tab. 5.1 and Tab. 5.2.

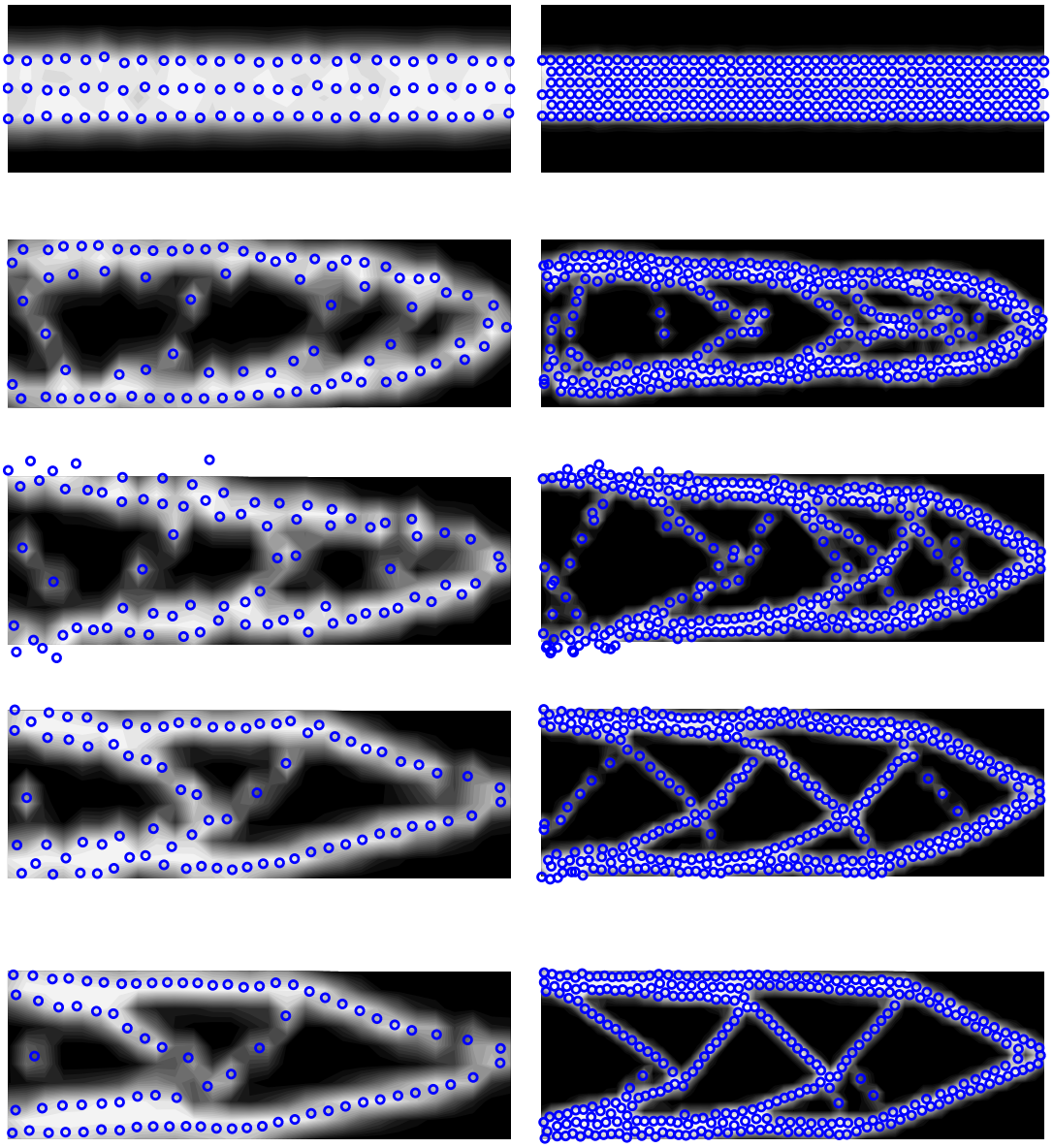

(a) Lower resolution (b) Higher resolution

Figure 5.7: Density distributions during optimization process of a cantilever beam with the design space and boundary conditions as depicted in Fig. 5.2. The size of the design space is equal to $D = 1$ and $L = 3$ and the density distribution is shown at time t^k with $k = 1, 25, 50, 100, 200$. The grey contour corresponds to the density and the blue nodes to the mass nodes. Both a lower and higher resolution for the discretization nodal distribution and the background mesh are considered, given by the parameters from Tab. 5.1 and Tab. 5.2.

spaces with size $L = 2$ and $D = 1$ and $L = 3$ and $D = 1$. Again, both a lower and higher discretization resolution have been used. For both design spaces, five density distributions obtained during the optimization process are shown in Fig. 5.6 and Fig. 5.7.[2] In both examples, the optimization process converges to an equilibrium nodal distribution. The shapes from these optimized nodal distributions shows some variations compared to the optimized shape of the design space with size $L = 1$ and $D = 2$. For instance, thin nodal arrays are present in the final optimized shape. These nodal arrays correspond to thin structural members. Furthermore, during the optimization process some nodes flow outside the design space. However, these nodes always return to the design space because of the compliance sensitivity. This can be explained by considering the total mass and compliance of the structure during the optimization process, as shown in Fig. 5.5b and Fig. 5.5c respectively. The total mass reduces when nodes leave the design space, which results in a reduction of the compliance. Therefore, the compliance sensitivity will direct the nodes back towards the design space. For some of the density distribution in Fig. 5.6 and Fig. 5.7, mass nodes appear to be disconnected from the other mass nodes. However, these nodes are in fact not disconnected. The relative large nodal influence domain present in the EFG formulation causes a coupling between nodes in relative large areas. This coupling can even occur between discretization nodes separated by low density regions (see Sec. 4.2.3), introducing additional non-physical stiffness in the structure. Based on the aforementioned findings, the general characteristics of the MNA in topology optimization are discussed in Sec. 5.3.

5.3 Characteristics of the MNA

In the previous sections of this chapter, an MNA optimization algorithm has been proposed and tested. For three exemplary problems a stiffer structure has been found with this flow-inspired topology optimization algorithm. Thus it has been shown that with a reasonably simple optimization algorithm a fixed amount of mass can be redistributed to increase the stiffness of a structure. In the proposed MNA algorithm the mass flows to a more optimal layout, resulting in a very intuitive and transparent optimization process. Although there is room for improvement of this algorithm, interesting characteristics of the MNA in topology optimization can be derived from the results obtained in Sec. 5.2. Next, a

[2]For the density distributions of the design space with size $L = 2$ and $D = 1$ the displacement and stress are shown in App. B in Fig. B.10.

discussion of these characteristics follows.

One of the interesting characteristics of the MNA is the conservation of mass. In the MNA, the shape is altered by displacing nodes with a fixed amount of mass. This provides for a topology optimization method in which no mass constraint has to be applied. The mass of the initial unimproved structure is therefore equal to the optimized structural mass. However, in the proposed optimization algorithm this is not completely true. The total mass decreases when nodal influence domains intersect the boundary of the design space. Moreover, the asymptotic density function causes a reduction in mass in areas with a high nodal compaction. Though, these two effects only cause a reduction in mass and therefore no constraint for the maximum mass has to be applied.

Another interesting characteristic of the MNA is the relative low number of required design variables. In the MNA, the mass distribution is directly linked to the nodal distribution, i.e. mass is distributed in areas which contain mass nodes. Therefore, design variables are only present in mass containing areas. This characteristic can reduce the computational cost of the sensitivity analysis, especially for large structures with low mass. These structures are often comprised of thin members. Since the mass of these structures is relatively low, the shape can be expressed by a low number of design variables. This could therefore result in a more efficient optimization process.

The proposed MNA algorithm also contains some problems. For instance, inaccuracies arise from the relatively large nodal influence domains in the EFG method. These inaccuracies are caused by the additional non-physical coupling between discretization nodes. This reduces the possibility of the EFG method to accurately describe highly irregular shapes. Therefore, these problems affect the optimization process in the MNA.

Furthermore, the redistribution of mass is highly path dependent, i.e. the shape can only be altered at the structural boundaries. For instance, this could pose a problem for the formation of new members in the structure or the redistribution of mass between two opposite sides of the design space. Problems are also present in the material density. In principle, to improve the manufacturability of the structure, the optimized material distribution should only contain normalized densities with a value of zero or one. In the MNA algorithm normalized densities are limited to values between zero and one. However, intermediate densities can still exist. These intermediate densities should merely be a tool to reduce the discontinuities of the shape of the structure during the optimization process and should not be present in the final solution.

In conclusion, the MNA in topology optimization shows interesting characteristics, especially the conservation of mass and the low number of required design variables are positive characteristics. Further research should be performed to improve this topology optimization approach and discover its full potential.

Summary

In this thesis the possibility of a flow-inspired Meshless Method based topology optimization method is explored. More specific, an investigation is carried out to the possibility of using the position of the nodes from the meshless EFG method as design variables in topology optimization.

In order to determine the possibility of using the nodal positions as design variables, the influence of variations in the nodal distribution on the EFG method accuracy is investigated. It turned out that the solution to the governing equations obtained with the EFG method is highly sensitive to nodal displacements. The most accurate results are obtained for regularly spaced nodal distributions. Moreover, the relation between the nodal distribution and the material distribution is investigated. The discretization of irregular shapes, often encountered in topology optimization, proves difficult. The difficulties arise from discontinuities in the material distribution and the occurrence of large material domains without nodes. These complications are mainly caused by the interaction between the nodal influence domains and the fixed background mesh.

The above-mentioned difficulties are avoided by the introduction of a material density that depends on the nodal compaction. Although the fixed background mesh is still present in this material distribution, the shape of the structure can be altered continuously. Moreover, with this material description the layout of the structure becomes sensitive to changes in the nodal position. This sensitivity can be utilized to alter the shape towards an optimal layout. However, the influence of the nodal position on the EFG method accuracy remains a problem.

Finally, a fairly simple Moving Node Approach (hereafter: MNA) topology optimization algorithm is proposed. In this proposed algorithm the influence of the nodal position on the EFG method is circumvented by using two types of nodes. One node type deals with the discretization of the linear elasticity equations and the other node type deals with the distribution of mass. In order to reach the optimal layout, each mass node is accelerated along the compliance sensitivity.

When applying this MNA algorithm to find the optimal shape of some exemplary problems, a few issues arise during the optimization process due to the large nodal influence domains. However, feasible optimal structural layouts are obtained. The resulting mass flow towards the optimal layout leads to a very intuitive and transparent optimization process. The most relevant characteristics of the proposed algorithm are the constant total mass and the relatively low number of required design variables.

This thesis shows the possibilities and difficulties arising in the MNA in topology optimization. The nodal positions can in principle be used as the design variables in order to obtain the optimal structural layout. However, more research needs to be conducted to further substantiate this argument.

Outlook

In light of the research objective of this thesis and considering that it is an initial exploration, recommendations and suggestions for future research are presented in this section.

Algorithm validation
It is crucial to further validate the topology optimization results obtained by using the MNA algorithm. The accuracy of the optimized shapes obtained with the MNA can be validated by comparing the shapes with shapes obtained with other topology optimization methods. Using this comparative approach it can be determined if the proposed MNA algorithm really reaches the optimal shape. Similarly, the convergence of the MNA can be compared with other already existing topology optimization methods.

Algorithm improvement
An improvement to the current MNA algorithm may be provided by replacing the EFG method with FEM. So far, the discretization nodes have been fixated during the optimization process, to solve problems concerning the discretization quality. This fixed discretization can therefore be replaced with FEM, possibly solving the problems arising from the large nodal influence domains and decreasing the calculation time. The FEM-based MNA will still have the same interesting properties as the EFG-based MNA, i.e. the conservation of mass and the low number of required design variables.

Expansion of capabilities
It would be very valuable to expand the capabilities of the MNA. In the current algorithm, the nodal mass is distributed around the nodes according to fixed nodal influence domain shapes. Instead, the shape and size of these influence domains can be altered to provide for other design variables in the optimization algorithm. For instance, the influence domains can take the shape of thin members. The design variables are then the position of the node, rotation of the node, thickness

and length of the influence domain. The resulting optimization algorithm is a combination between shape and topology optimization. If successful, this method could considerably reduce the number of design variables and increase the manufacturability of the optimized shape.

MNA in practise

In practise, the MNA is a very intuitive and transparent topology optimization method. When transposed into workable software, the MNA could be used as a teaching tool to visualize topology optimization. During the optimization process such a tool would allow for interaction with the mass flow, establishing an insightful experience.

Bibliography

[1] TopOpt research group, "3D topology optimization of a satellite support structure." http://www.topopt.dtu.dk/?q=node/15, January 2012.

[2] "Topology optimization of microfluidic mixers," *International Journal for Numerical Methods in Fluids*, vol. 61, pp. 498–513, 2009.

[3] O. Sigmund and S. Torquato, "Composites with extremal thermal expansion coefficients," *Applied Physics Letters*, vol. 69, no. 21, pp. 3203–3205, 1996.

[4] TopOpt research group, "Topology optimization of crashworthiness of a car." http://www.topopt.dtu.dk/?q=node/14, January 2012.

[5] M. P. Bendsøe and N. Kikuchi, "Generating optimal topologies in structural design using a homogenization method," *Computer Methods in Applied Mechanics and Engineering*, vol. 71, no. 2, pp. 197 – 224, 1988.

[6] M. P. Bendsøe, "Optimal shape design as a material distribution problem," *Structural and Multidisciplinary Optimization*, vol. 1, pp. 193–202, 1989.

[7] M. Bendsøe and O. Sigmund, *Topology optimization: theory, methods, and applications*. Engineering online library, Springer, 2003.

[8] O. Sigmund and J. Petersson, "Numerical instabilities in topology optimization: A survey on procedures dealing with checkerboards, mesh-dependencies and local minima," *Structural and Multidisciplinary Optimization*, vol. 16, pp. 68–75, 1998.

[9] Y. Xie and G. Steven, "A simple evolutionary procedure for structural optimization," *Computers & amp; Structures*, vol. 49, no. 5, pp. 885 – 896, 1993.

[10] D. N. Chu, Y. Xie, A. Hira, and G. Steven, "On various aspects of evolutionary structural optimization for problems with stiffness constraints," *Finite Elements in Analysis and Design*, vol. 24, no. 4, pp. 197 – 212, 1997.

[11] J. Sethian and A. Wiegmann, "Structural boundary design via level set and immersed interface methods," *Journal of Computational Physics*, vol. 163, no. 2, pp. 489 – 528, 2000.

[12] T. Belytschko, Y. Y. Lu, and L. Gu, "Element-free Galerkin methods," *International Journal for Numerical Methods in Engineering*, vol. 37, no. 2, pp. 229–256, 1994.

[13] Z. Juan, L. Shuyao, and L. Guangyao, "The topology optimization design for continuum structures based on the element free Galerkin method," *Engineering Analysis with Boundary Elements*, vol. 34, no. 7, pp. 666 – 672, 2010.

[14] V. P. Nguyen, T. Rabczuk, S. phane Bordas, and M. Duflot, "Meshless methods: A review and computer implementation aspects," *Mathematics and Computers in Simulation*, vol. 79, no. 3, pp. 763 – 813, 2008.

[15] T. Belytschko, Y. Krongauz, D. Organ, M. Fleming, and P. Krysl, "Meshless methods: An overview and recent developments," *Computer Methods in Applied Mechanics and Engineering*, vol. 139, no. 1-4, pp. 3 – 47, 1996.

[16] G. Liu and M. Liu, *Smoothed particle hydrodynamics: a meshfree particle method*. World Scientific, 2003.

[17] R. A. Gingold and J. J. Monaghan, "Smoothed particle hydrodynamics - Theory and application to non-spherical stars," *Monthly Notices R. Astron. Soc.*, vol. 181, pp. 375–389, 1977.

[18] L. B. Lucy, "A numerical approach to the testing of the fission hypothesis," *Astron J.*, vol. 82, pp. 1013–1024, Dec. 1977.

[19] L. D. Libersky, A. G. Petschek, T. C. Carney, J. R. Hipp, and F. A. Allahdadi, "High strain lagrangian hydrodynamics: A three-dimensional SPH code for dynamic material response," *Journal of Computational Physics*, vol. 109, no. 1, pp. 67 – 75, 1993.

[20] J. van Kan, A. Segal, and F. Vermolen, *Numerical methods in scientific computing*. VSSD, 2008.

[21] R. D. Cook, D. S. Malkus, M. E. Plesha, and R. J. Witt, *Concepts and applications of finite element analysis*. John Wiley & Sons, Inc., fourth ed., 2002.

[22] S. N. Atluri and T. Zhu, "A new Meshless Local Petrov-Galerkin (MLPG) approach in computational mechanics," *Computational Mechanics*, vol. 22, pp. 117–127, 1998.

[23] S. Li and S. Atluri, "Topology-optimization of structures based on the MLPG mixed collocation method," *Tech Science Press CMES*, vol. 26, no. 1, pp. 61–74, 2008.

[24] S. Li and S. Atluri, *The MLPG mixed collocation method for material orientation and topology optimization of anisotropic solids and structures*. Tech Science Press, 2010.

[25] J. Zheng, S. Long, Y. Xiong, and G. Li, "A finite volume meshless local Petrov-Galerkin method for topology optimization design of the continuum structures," *CMES: Computer Modeling in Engineering & Sciences*, vol. 42, no. 1, pp. 19–34, 2009.

[26] B. Hassani, M. Khanzadi, and S. Tavakkoli, "An isogeometrical approach to structural topology optimization by optimality criteria," *Structural and Multidisciplinary Optimization*, vol. 45, pp. 223–233, 2012.

[27] T. Belytschko, S. P. Xiao, and C. Parimi, "Topology optimization with implicit functions and regularization," *International Journal for Numerical Methods in Engineering*, vol. 57, no. 8, pp. 1177–1196, 2003.

[28] S. Wang and M. Y. Wang, "Radial basis functions and level set method for structural topology optimization," *International Journal for Numerical Methods in Engineering*, vol. 65, no. 12, pp. 2060–2090, 2006.

[29] J. Zhou and W. Zou, "Meshless approximation combined with implicit topology description for optimization of continua," *Structural and Multidisciplinary Optimization*, vol. 36, pp. 347–353, 2008.

[30] S. Wang, K. Lim, B. Khoo, and M. Wang, "An unconditionally time-stable level set method and its application to shape and topology optimization," *CMES - Computer Modeling in Engineering and Sciences*, vol. 21, no. 1, pp. 1–40, 2007.

[31] H. Ho, B. Lui, and M. Wang, "Parametric structural optimization with radial basis functions and partition of unity method," *Optimization Methods and Software*, vol. 26, no. 4-5, pp. 533–553, 2011.

[32] Z. Luo, N. Zhang, W. Gao, and H. Ma, "Structural shape and topology optimization using a meshless galerkin level set method," *International Journal for Numerical Methods in Engineering*.

[33] S. Cho and J. Kwak, "Topology design optimization of geometrically nonlinear structures using meshfree method," *Computer Methods in Applied Mechanics and Engineering*, vol. 195, no. 44-47, pp. 5909 – 5925, 2006.

[34] Y. Du, L. Chen, and Z. Luo, "Topology synthesis of geometrically nonlinear compliant mechanisms using meshless methods," *Acta Mechanica Solida Sinica*, vol. 21, no. 1, pp. 51 – 61, 2008.

[35] Y. Du, L. Chen, Q. Tian, and Z. Wu, "Topology synthesis of thermomechanical compliant mechanisms with geometrical nonlinearities using meshless method," *Advances in Engineering Software*, vol. 40, no. 5, pp. 315 – 322, 2009.

[36] Y. Du, Q. Tian, and Z. Wu, "Optimal design of compliant thermal-structural microactuators with geometrical nonlinearities," pp. 2118 –2122, 2009.

[37] P. Kundu and I. Cohen, *Fluid mechanics*. Academic Press, Elsevier Science and Technology, 2008.

[38] F. Eng., "Newsletter 2009-01: Fluid flow around a moving propeller found with the SPH method." http://www.femto.eu/, January 2012.

[39] S. Atluri, H. Liu, and Z. Han, "Meshless Local Petrov-Galerkin (MLPG) mixed collocation method for elasticiy problems," *Tech Science Press CMES*, vol. 14, no. 3, pp. 141–152, 2006.

[40] S. N. Atluri and T. Zhu, "A new Meshless Local Petrov-Galerkin (MLPG) approach in computational mechanics," *Computational Mechanics*, vol. 22, pp. 117–127, 1998.

[41] S. N. Atluri, *The meshless method (MLPG) for domain and BIE discretizations*. Tech Science Press, 2004.

[42] J. Monaghan, "Smoothed particle hydrodynamics," *Annual Reviews Incorperation Astronomy and Astrophysics*, vol. 30, pp. 543–574, 1992.

[43] J. Monaghan, "Smoothed particle hydrodynamics," *Reports on Progress in Physics*, vol. 68, pp. 1703–1759, 2005.

[44] J. Zheng, S. Long, and G. Li, "Topology optimization of free vibrating continuum structures based on the element free Galerkin method," *Structural and Multidisciplinary Optimization*, pp. 1–9, 2011.

[45] Z. Han and S. Atluri, "A truly-meshless Galerkin method, through the MLPG "mixed" approach,"

[46] F. M. Dekking, C. Kraaikamp, H. P. Lopuhaä, and L. E. Meester, *A modern Introduction to probability and statistics: Understanding why and how.* Springer, 2005.

Appendix

A Gauss quadrature

Gauss quadrature is used to evaluate an integral numerically. Only the values at certain points along the integration interval, or integration points, are required to evaluate the integration numerically. For one dimension the integration I with interval limits x_1, x_2 can be rewritten in a more general form [21]:

$$I = \int_{x=x_1}^{x=x_2} f(x)dx = \int_{\xi=-1}^{\xi=1} f\left(\frac{1}{2}[1-\xi]x_1 + \frac{1}{2}[1+\xi]x_2\right)\frac{x_2-x_1}{2}d\xi = \int_{-1}^{1}\phi(\xi)d\xi, \tag{5.14}$$

where

$$x = \frac{1}{2}[1-\xi]x_1 + \frac{1}{2}[1+\xi]x_2. \tag{5.15}$$

Numerical integration of I can be estimated with

$$I = \int_{-1}^{1}\phi(\xi)d\xi = \sum_{I=1}^{n} W^I\phi^I, \tag{5.16}$$

in which n is the number of integration points and W^I is the weight at the integration point I. The location of the integration points depends on the number of integration points n. Similarly, the weight of each integration point depends on the number of integration points n. These locations and weights are given in Tab. 5.3 for different values of n.

In two dimensions, numerically evaluating the integral in a rectangular domain can be performed similarly. The integral I with limits x_1, x_2 in x direction and limits y_1, y_2 in y direction can be rewritten as

$$\begin{aligned} I &= \int_{x=x_1}^{x=x_2}\int_{y=y_1}^{y=y_2} f(x,y)dydx = \int_{\xi=-1}^{\xi=1}\int_{\psi=-1}^{\psi=1} f(x,y)\frac{x_2-x_1}{2}\frac{y_2-y_1}{2}d\psi d\xi \\ &= \int_{-1}^{1}\int_{-1}^{1}\phi(\xi,\psi)d\psi d\xi, \end{aligned} \tag{5.17}$$

Table 5.3: Location and weights of n integration points for Gauss quadrature in one dimension

Order n	Location Int. Point	Weigh factors
1	0	2
2	$\pm 1/\sqrt{3}$	1
3	$\pm\sqrt{3/5}$	5/9
	0	8/9
4	$\pm\sqrt{[3-2\sqrt{6/5}]/7}$	$[18+\sqrt{30}]/36$
	$\pm\sqrt{[3+2\sqrt{6/5}]/7}$	$[18-\sqrt{30}]/36$
5	$\pm[1/3]\sqrt{5-2\sqrt{10/7}}$	$[322+13\sqrt{70}]/900$
	$\pm[1/3]\sqrt{5+2\sqrt{10/7}}$	$[322-13\sqrt{70}]/900$
	0	128/225

where

$$x = \frac{1}{2}[1-\xi]x_1 + \frac{1}{2}[1+\xi]x_2$$
$$y = \frac{1}{2}[1-\psi]y_1 + \frac{1}{2}[1+\psi]y_2. \tag{5.18}$$

Numerical integration of the I can be estimated with

$$I = \int_{-1}^{1}\int_{-1}^{1} \phi(\xi,\psi)d\psi d\xi = \sum_{i=1}^{n}\sum_{j=1}^{n} W_i W_j \phi_{ij}, \tag{5.19}$$

in which the weights W_i and W_j can be found in Tab. 5.3 and ϕ_{ij} is the value at corresponding integration point.

B Displacement and stress results

In this chapter of the appendix displacement and stress results are shown for simulation performed in Chap. 3, Chap. 4 and Chap. 5. In these chapters series of simulations have been performed in order to investigate the behavior of the EFG method under different circumstances. For most of these simulation only the compliance C, error norm $||E||$ and mass m_{tot} have been shown in various figures. However, underlying these three scalar quantities are the EFG solutions of the linear elastic equations. For completeness, some of the displacement and stress solutions obtained with the EFG method are presented in this section. To reduce the number of figures, only the magnitude of the displacement u_m and the Von Mises stress σ_{vm} are shown, defined by

$$u_m = \sqrt{u_1^2 + u_2^2}, \tag{5.20}$$

and

$$\sigma_{vm} = \sqrt{\sigma_{11}^2 - \sigma_{11}\sigma_{22} + \sigma_{22}^2 + 3\sigma_{12}^2}. \tag{5.21}$$

Further interpretation of the displacement and stress results is left to the reader.

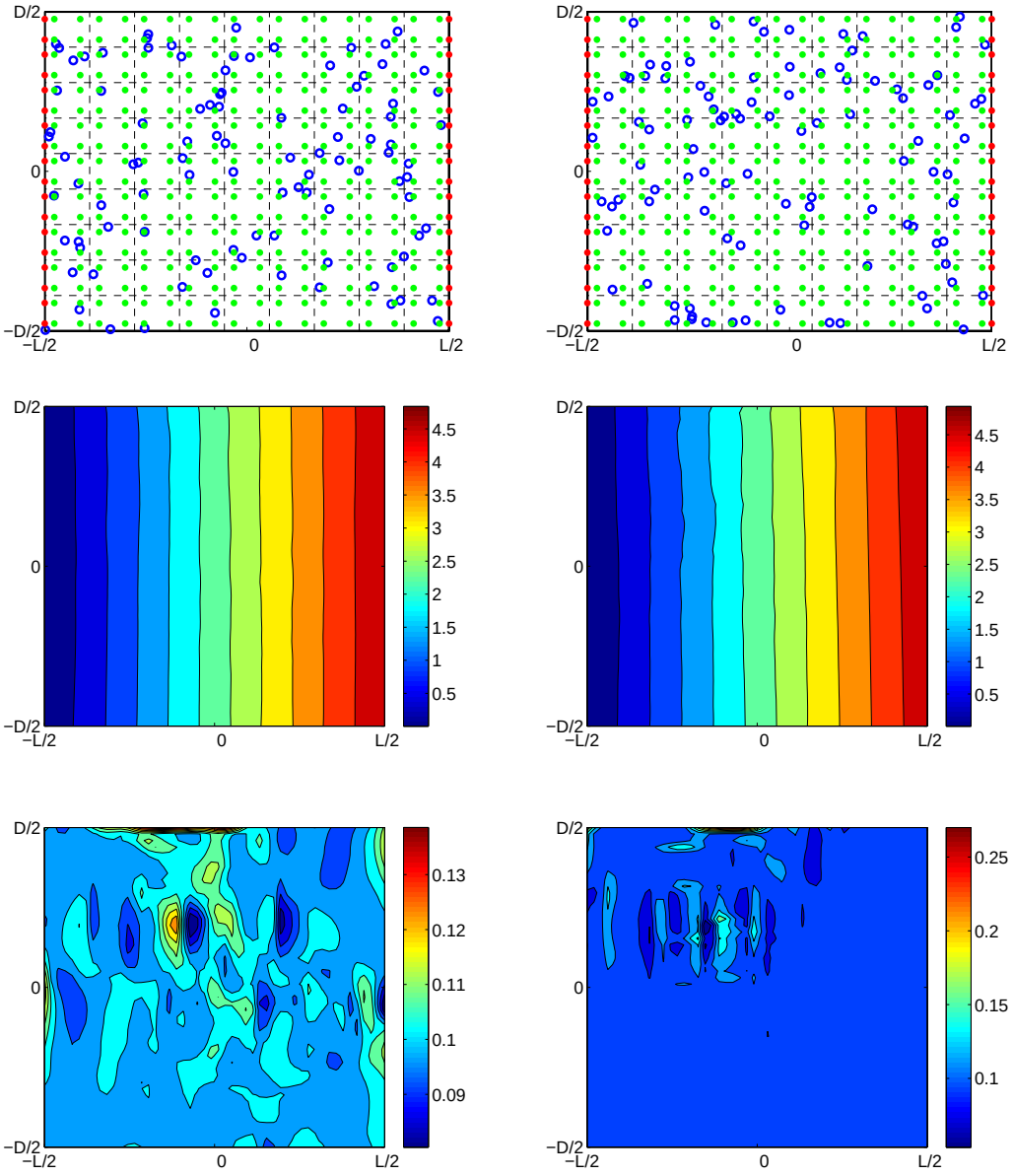

(a) Sample 1: $C = 5.79$ and $||E|| = 0.059$

(b) Sample 2: $C = 5.84$ and $||E|| = 0.10$

Figure B.1: Respectively, the discretization, u_m and σ_{vm} for two samples of the uniaxial beam problem with random nodal distributions discussed in Sec. 3.1.1. The problem is described in Fig. 4.6 and solved with the EFG method according to the parameters in Tab. 3.3.

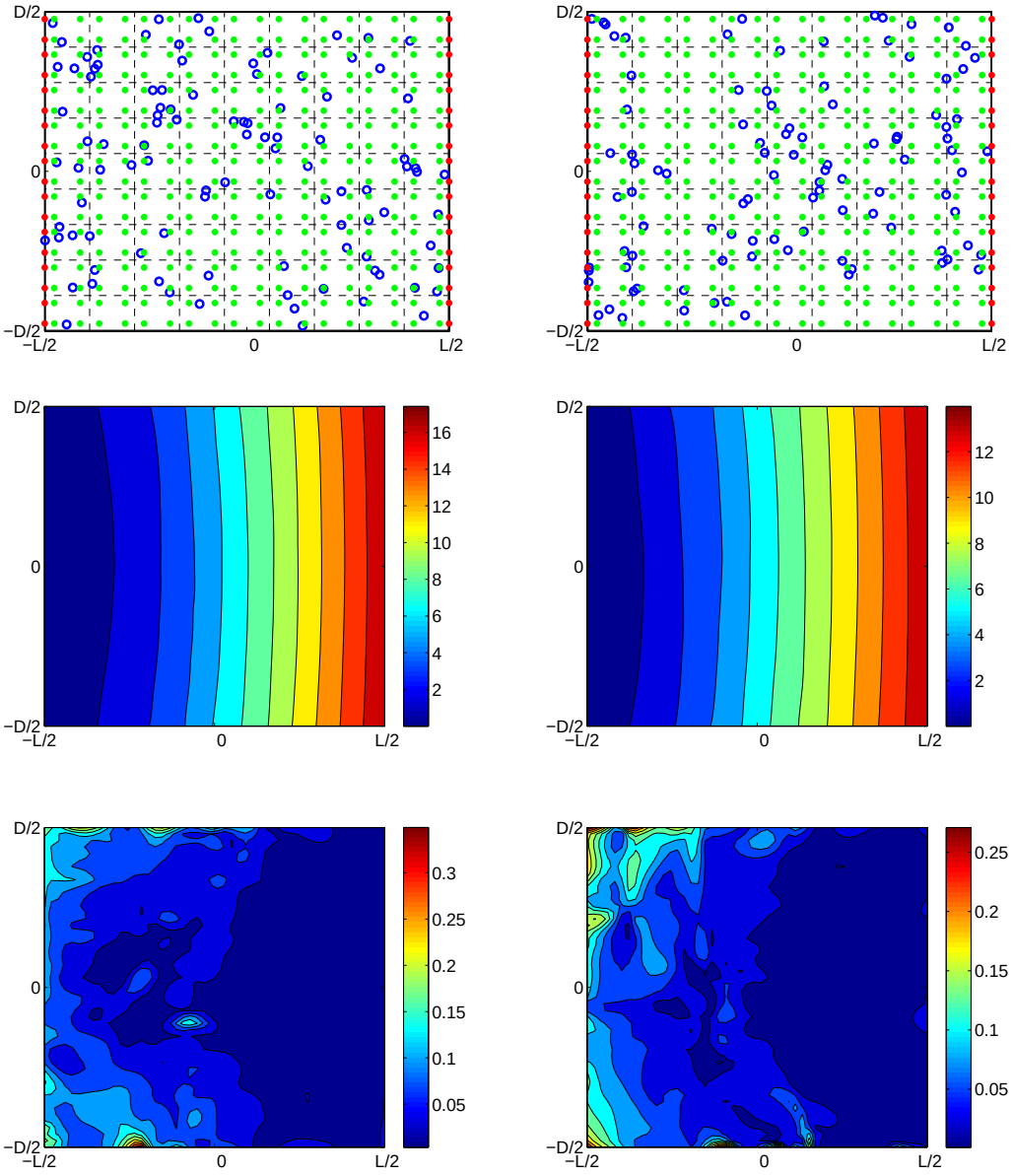

(a) Sample 1: $C = 1.71$ and $||E|| = 0.57$

(b) Sample 2: $C = 1.37$ and $||E|| = 0.67$

Figure B.2: Respectively, the discretization, u_m and σ_{vm} for two samples of the cantilever beam problem with random nodal distributions discussed in Sec. 3.1.1. The problem is described in Fig. 4.6 and solved with the EFG method according to the parameters in Tab. 3.3.

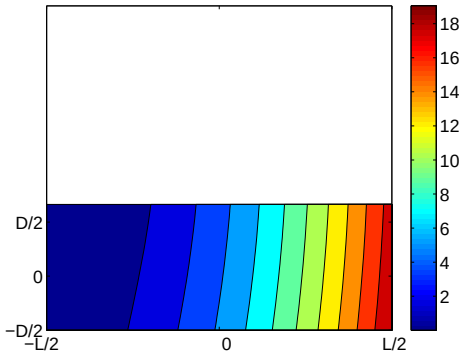

(a) u_m for $d_2 = 0$

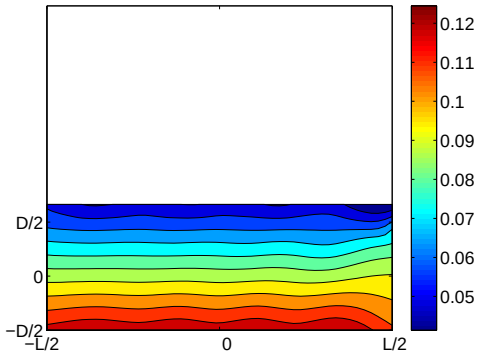

(b) σ_{vm} for $d_2 = 0$

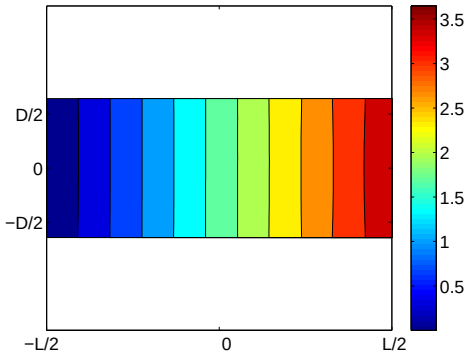

(c) u_m for $d_2 = 4$

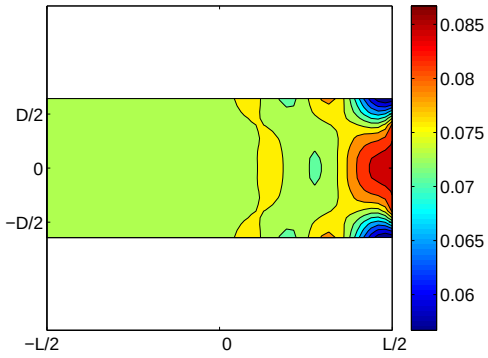

(d) σ_{vm} for $d_2 = 4$

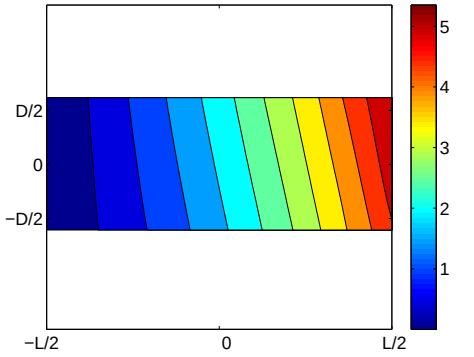

(e) u_m for $d_2 = 4.1$

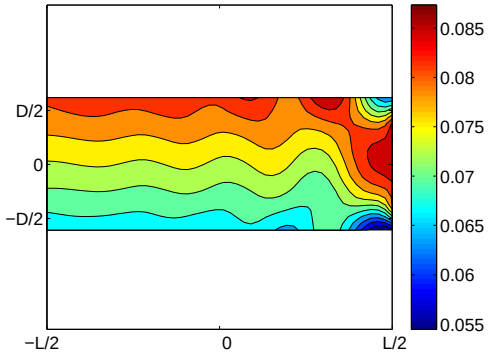

(f) σ_{vm} for $d_2 = 4.1$

Figure B.3: Displacement and stress results for three samples of the problem described in Sec. 3.2.2, in which all integration cells inside the nodal influence domain are taken into account. The problem is described in Fig. 3.14 and solved with the EFG method according to the parameters in Tab. 3.3.

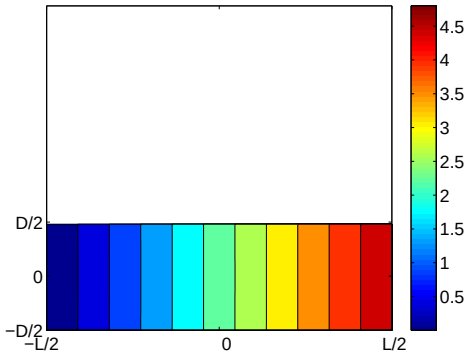

(a) u_m for $d_2 = 0$

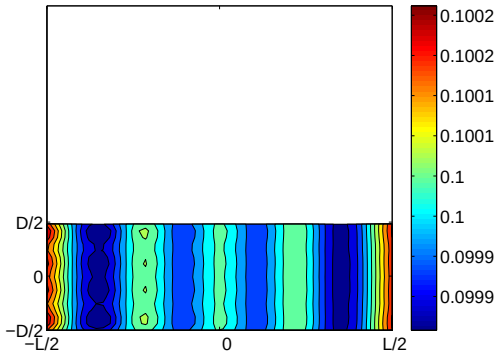

(b) σ_{vm} for $d_2 = 0$

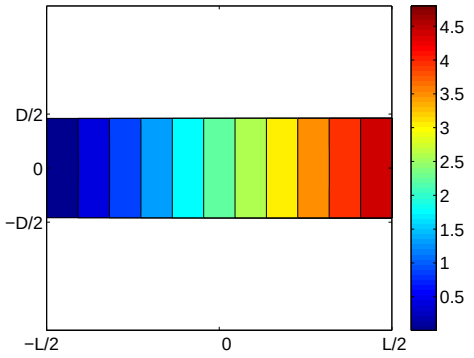

(c) u_m for $d_2 = 4$

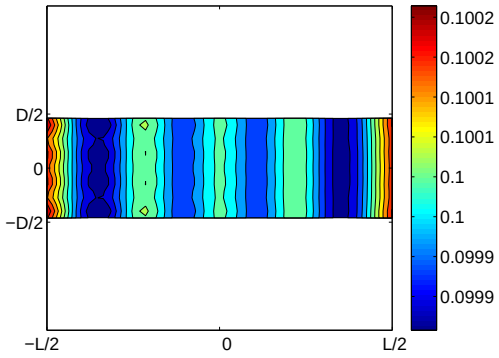

(d) σ_{vm} for $d_2 = 4$

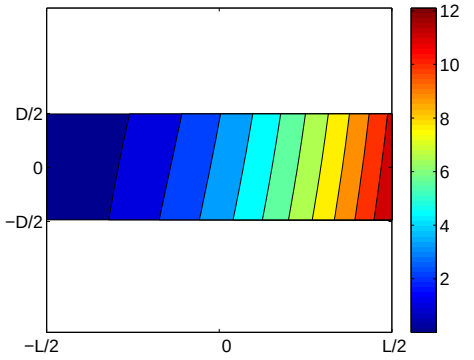

(e) u_m for $d_2 = 4.1$

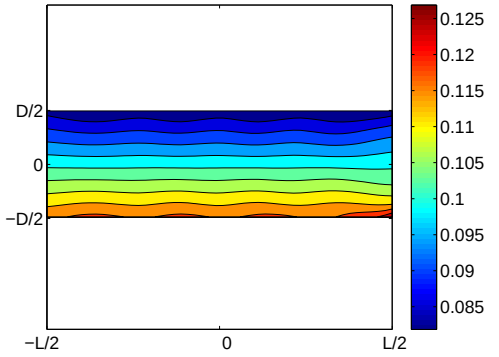

(f) σ_{vm} for $d_2 = 4.1$

Figure B.4: Displacement and stress results for three samples of the problem described in Sec. 3.2.2, in which only the integration cells inside the problem domain are taken into account. The problem is described in Fig. 3.14 and solved with the EFG method according to the parameters in Tab. 3.3.

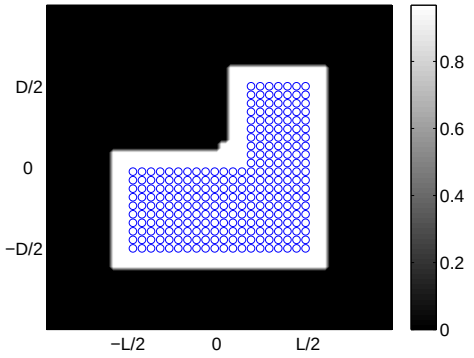

(a) ρ for original material distribution

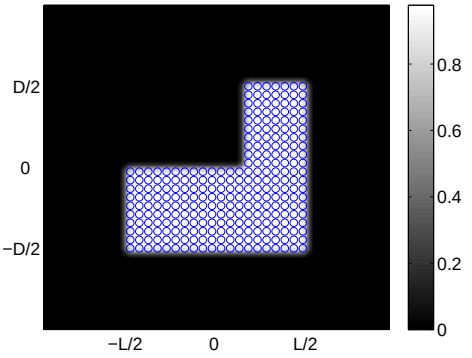

(b) ρ for nodal compaction material distribution

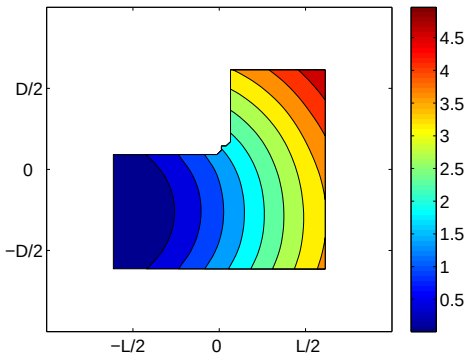

(c) u_m for original material distribution

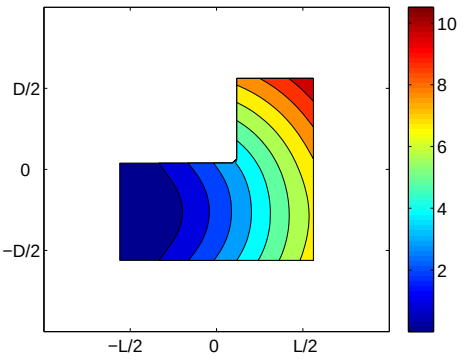

(d) u_m for nodal compaction material distribution

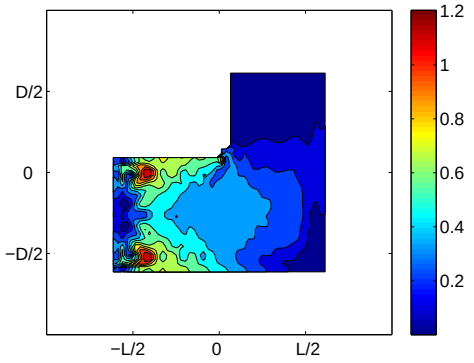

(e) σ_{vm} for original material distribution

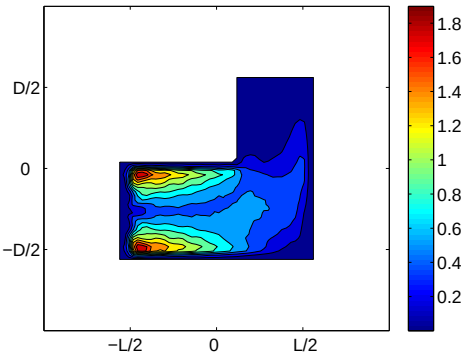

(f) σ_{vm} for nodal compaction material distribution

Figure B.5: Displacement and stress results for one samples of the problem described in Sec. 3.2.2, in which part of the nodes is moved up by a value of $d_2 = 0$. The problem is described in Fig. 4.9 and solved with the EFG method according to the parameters in Tab. 4.2.

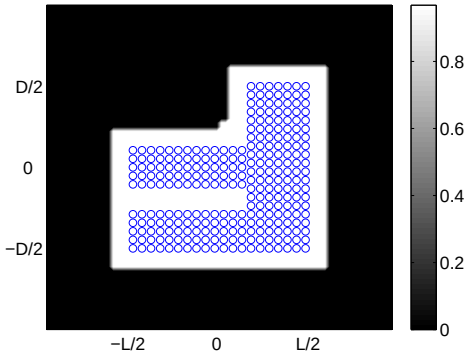

(a) ρ for original material distribution

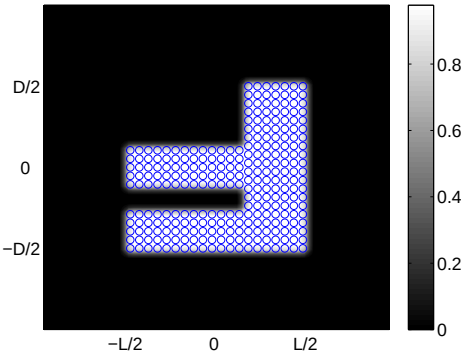

(b) ρ for nodal compaction material distribution

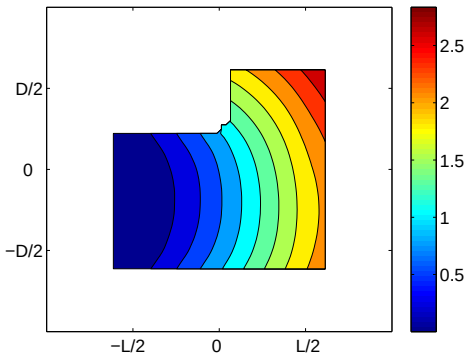

(c) u_m for original material distribution

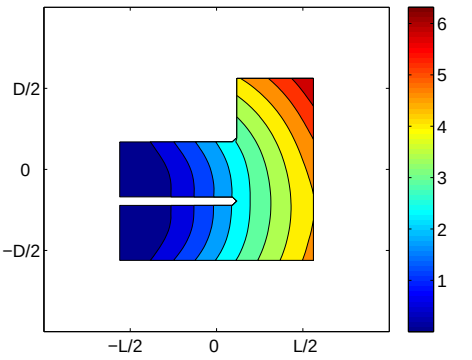

(d) u_m for nodal compaction material distribution

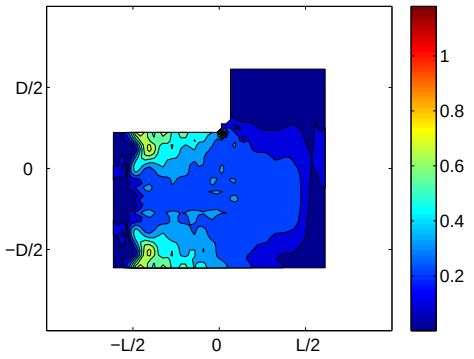

(e) σ_{vm} for original material distribution

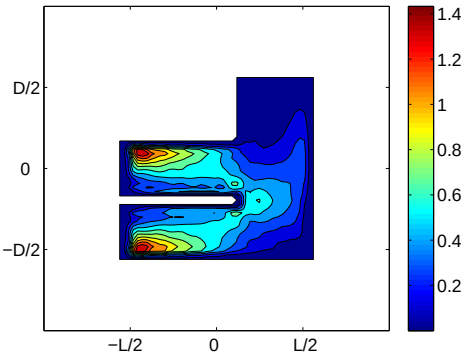

(f) σ_{vm} for nodal compaction material distribution

Figure B.6: Displacement and stress results for one samples of the problem described in Sec. 3.2.2, in which part of the nodes is moved up by a value of $d_2 = 5/19$. The problem is described in Fig. 4.9 and solved with the EFG method according to the parameters in Tab. 4.2.

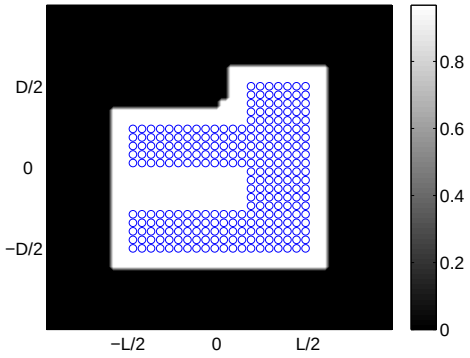

(a) ρ for original material distribution

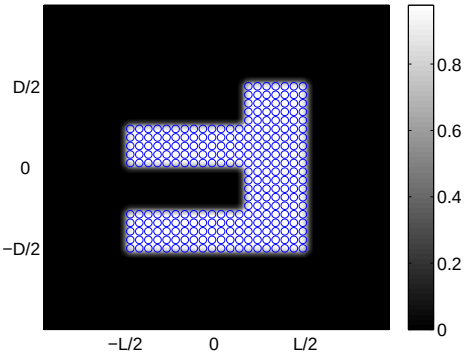

(b) ρ for nodal compaction material distribution

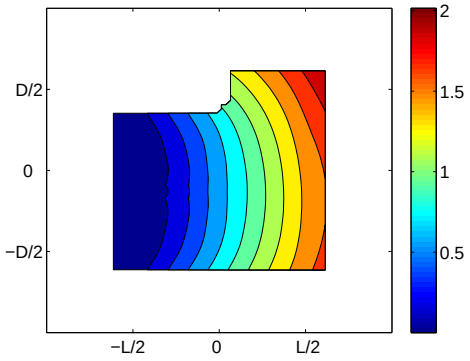

(c) u_m for original material distribution

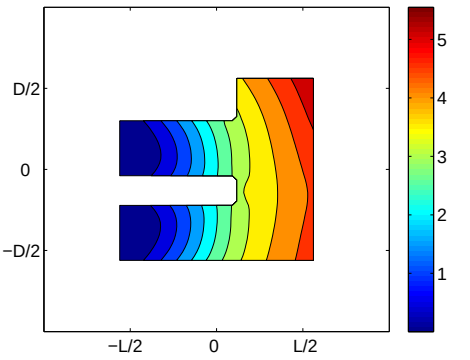

(d) u_m for nodal compaction material distribution

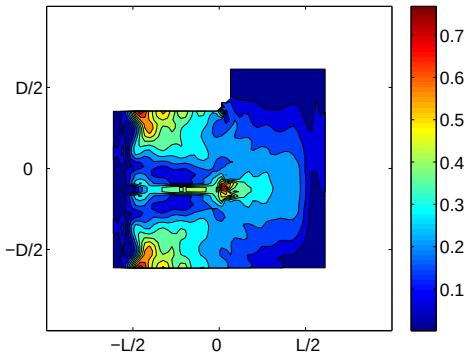

(e) σ_{vm} for original material distribution

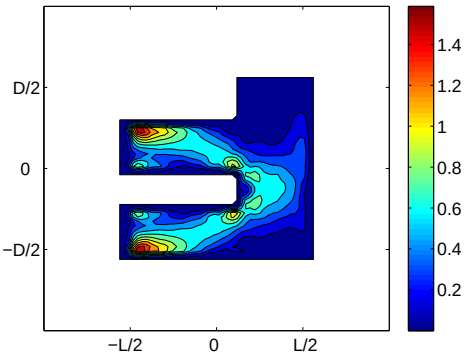

(f) σ_{vm} for nodal compaction material distribution

Figure B.7: Displacement and stress results for one samples of the problem described in Sec. 3.2.2, in which part of the nodes is moved up by a value of $d_2 = 10/19$. The problem is described in Fig. 4.9 and solved with the EFG method according to the parameters in Tab. 4.2.

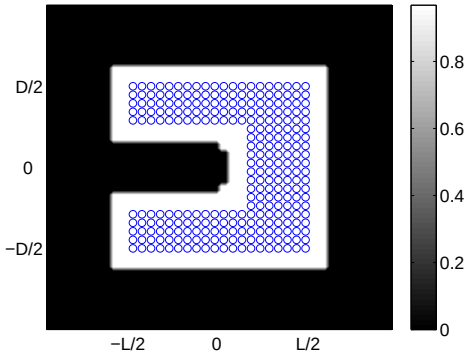

(a) ρ for original material distribution

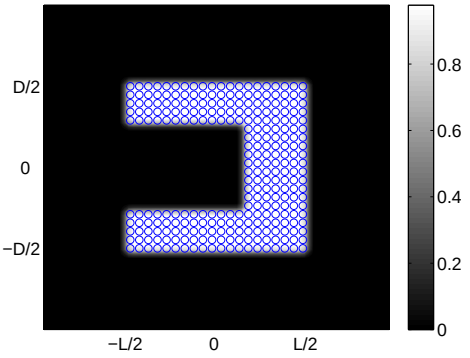

(b) ρ for nodal compaction material distribution

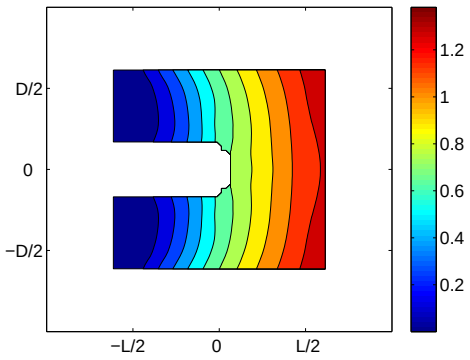

(c) u_m for original material distribution

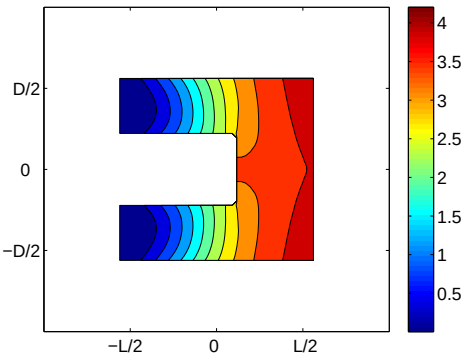

(d) u_m for nodal compaction material distribution

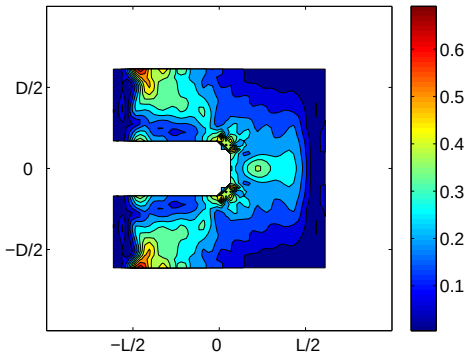

(e) σ_{vm} for original material distribution

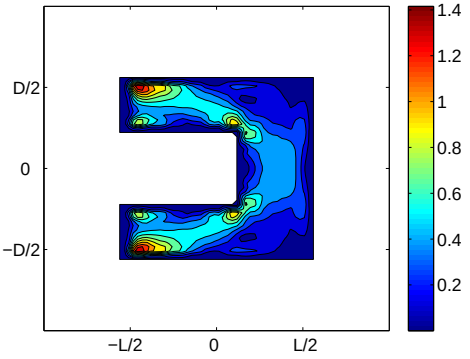

(f) σ_{vm} for nodal compaction material distribution

Figure B.8: Displacement and stress results for one samples of the problem described in Sec. 3.2.2, in which part of the nodes is moved up by a value of $d_2 = 20/19$. The problem is described in Fig. 4.9 and solved with the EFG method according to the parameters in Tab. 4.2.

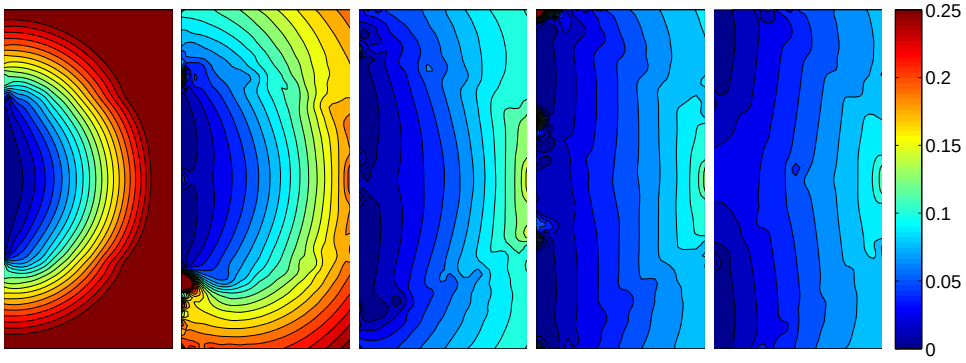

(a) u_m

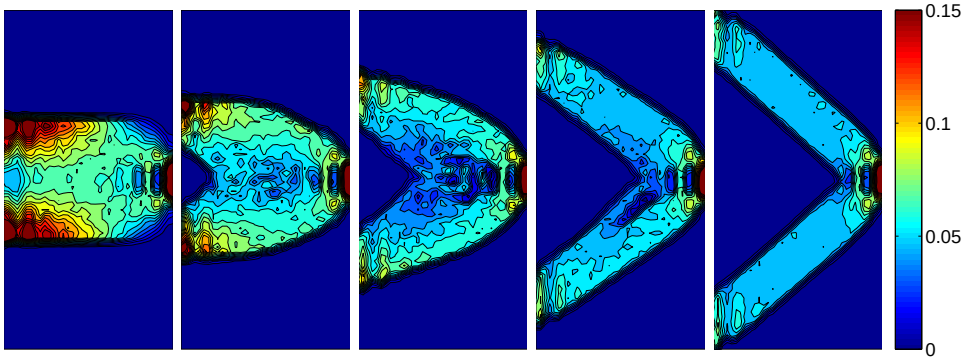

(b) σ_{vm}

Figure B.9: Displacement and stress during optimization process of a cantilever beam with the design space and boundary conditions as depicted in Fig. 5.2 (Sec. 5.2). The size of the design space is equal to $D = 2$ and $L = 1$ and the results are shown at time t^k with $k = 1, 25, 50, 100, 200$. A higher resolution for the discretization nodal distribution and the background mesh is considered, given by the parameters from Tab. 5.1 and Tab. 5.2.

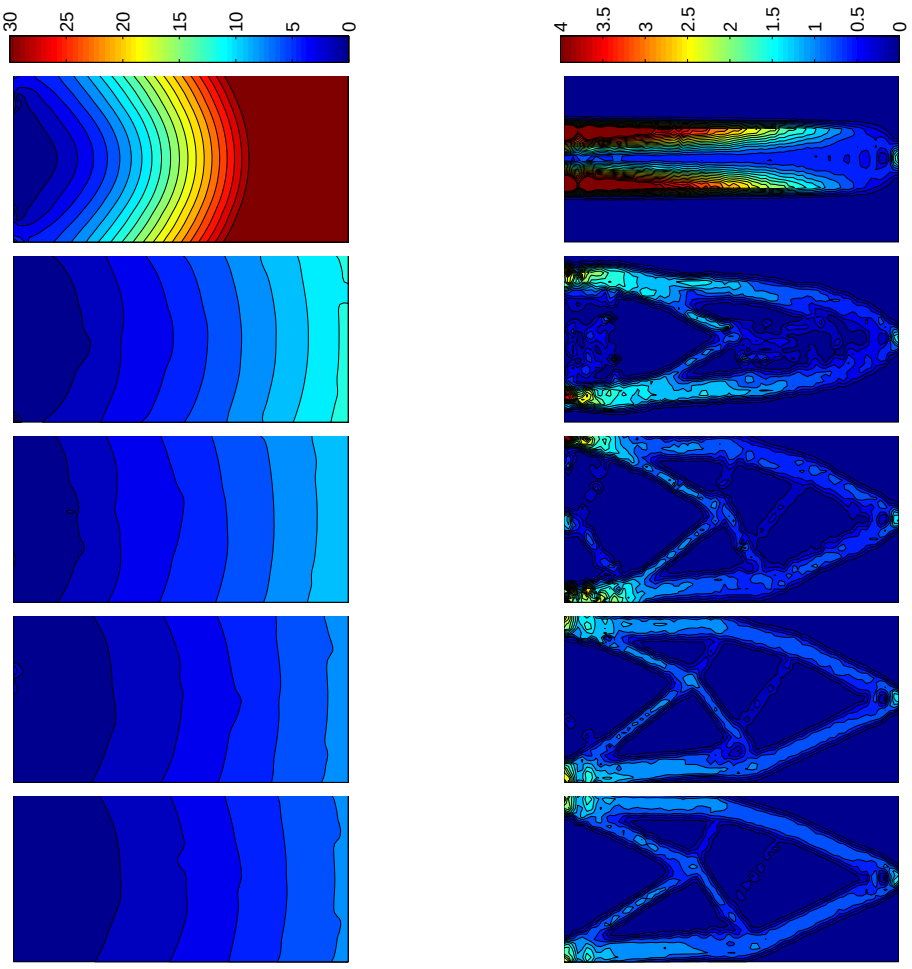

(a) u_m (b) σ_{vm}

Figure B.10: Displacement and stress during optimization process of a cantilever beam with the design space and boundary conditions as depicted in Fig. 5.2 (Sec. 5.2). The size of the design space is equal to $D = 1$ and $L = 2$ and the results are shown at time t^k with $k = 1, 25, 50, 100, 200$. A higher resolution for the discretization nodal distribution and the background mesh is considered, given by the parameters from Tab. 5.1 and Tab. 5.2.